

Separation of hafnium from zirconium using membrane based solvent extraction

D Malan

 orcid.org/0000-0002-5482-000X

Dissertation accepted in fulfillment of the requirements for the
degree Master of Engineering with Chemical Engineering at
the North-West University

Supervisor: Prof H.W.J.P. Neomagus
Co-Supervisor: Prof H.M. Krieg
Co-Supervisor: Mr D.J. van der Westhuizen

Graduation: May 2022
Student number: 22746250

Declaration

I, Daniël Malan, hereby declare that the dissertation titled “**Separation of hafnium from zirconium using membrane based solvent extraction**”, is submitted in the fulfilment of the requirements of the degree of Master of Engineering with Chemical Engineering, and is my own work, except where acknowledged in the text. The document has been language edited as required, and has not been submitted to any other tertiary institution in whole or in part.

I understand that the copies handed in for examination are the property of the North-West University.

Signed at Alberton, Gauteng on 23 November 2021.



Mr. D. Malan (student)

22746250

University number

Research contributions from this study

Article

Malan D, Van Der Westhuizen DJ, Neomagus HWJP, Krieg HM. The effect of molar ratio and flow velocity on the surface area required for pertraction of a Zr / Hf mixture. In: IOP Conference Series: Materials Science and Engineering. 2019. doi:10.1088/1757-899X/655/1/012041

Oral presentation

Malan D, Van Der Westhuizen DJ, Neomagus HWJP, Krieg HM. Predicting concentration profiles along a pertraction column. Conference of the South African Advanced Materials Initiative (CoSAAMI). 23-26 October 2018.

Preface

*“I have already made this paper too long, for which I must
crave pardon, not having now time to make it shorter.”*

- Benjamin Franklin, 1750 -

I want to extend my gratitude to the following people:

- My supervisors, Professors Neomagus & Krieg, and Mr. van der Westhuizen. Your guidance and patience have been invaluable to me, without which I would not have been able to complete this degree.
- Mrs. Stoppel for all the kind, yet stern words of motivation as well as the superpower of knowing who to ask about anything.

I want to also thank the following institutions:

- The CRB and the North-West University for the use of their facilities.
- ChemQuest for the supply of our ShellSol 2325 diluent.
- Necsa and the AMI for the bursary that supported this research project.

Abstract

The need for purified Zr and Hf has become imperative with the development of the nuclear industry. Solvent extraction (SX) processes, such as the TBP and MIBK processes have been successfully applied for the industrial separation of Zr and Hf, however, the crud and emulsion formation of SX processes have prompted efforts to find alternative separation methods. Membrane based solvent extraction (MBSX) is one such alternative, where a porous membrane between the aqueous and organic phases creates an immobilised liquid-liquid (L-L) interface, thus avoiding phase dispersion, while still allowing for mass transfer between the phases.

In view of the limited data on this novel technology, the aim of this study was to develop an approach to predict the technical feasibility of an MBSX unit. For this purpose, the Hf selective separation from Hf/Zr solutions using a D2EHPA-H₂SO₄ system was selected. To attain this, the partition coefficients of Zr and Hf, as well as the effect of the fluid velocity on either side of the membrane was determined experimentally, followed by the development of a process model to technically evaluate an industrial-scale unit.

Liquid-liquid equilibria (LLE) and MBSX experimental data were collected. The LLE data showed that a high separation factor was obtained for the D2EHPA-H₂SO₄ system, while also the corresponding partition coefficients of Zr and Hf were determined. A separation factor of 7.5 was achieved when contacting an aqueous phase of 16 g.L⁻¹ Zr, 0.36 g.L⁻¹ Hf, and 98 g.L⁻¹ H₂SO₄ with an organic phase consisting of 230 g.L⁻¹ D2EHPA, and 41 g.L⁻¹ 1-octanol in Shellsol 2325. The partition coefficients of Zr and Hf were 20.7 and 157 respectively. According to the MBSX experiments, the non-selective diffusion through the shell-side boundary layer dominated the mass transfer resulting in a separation ratio below 2.0 with overall mass transfer coefficients in the order of 9.4×10^{-8} and 1.3×10^{-7} m.s⁻¹ for Zr and Hf respectively. The lumen did not offer significant resistance to mass transfer and was negligible for Re numbers higher than 0.61.

A process model and design methodology were proposed, and in combination with Sherwood relations that were fitted to the experimental data, and industrial-scale design was proposed. These calculations confirmed that the shell-side dominated the overall rates of mass transfer, and through this, that the low separation ratio made the industrial-scale application of MBSX ill-advised as the membrane surface area that was predicted to be in the order of a trillion m², and the organic flow rates in the order of 100 m³.s⁻¹.

It was finally concluded that this technology can only be considered for further exploration if the shell-side mass transfer coefficient increased at least with a factor 1000 to 1×10^{-4} m.s⁻¹.

Keywords: Zirconium, Hafnium, D2EHPA, Membrane based solvent extraction, Mass transfer, MBSX model.

Table of contents

Declaration	I
Research contributions from this study	II
Preface	III
Abstract	IV
Table of contents	V
List of Tables	VIII
List of Figures	IX
List of Symbols	XI
List of Abbreviations	XII
1 Introduction	1
1.1 Background and motivation.....	1
1.2 Problem statement.....	3
1.3 Aim and objectives.....	3
1.4 Scope and limitations.....	4
1.4.1 Experimental and modelling outcomes	4
1.4.2 Order of operations.....	4
1.4.3 Constraints	6
1.5 Dissertation layout	7
2 Literature	9
2.1 Overview of Zr and Hf production.....	9
2.2 The separation of Zr and Hf	10
2.2.1 Pyrometallurgy	10
2.2.2 Solvent extraction (SX).....	10
2.3 Novel SX approaches	15
2.3.1 Disadvantages of SX.....	20
2.4 Membrane-based solvent extraction (MBSX).....	21
2.4.1 Introduction.....	21
2.4.2 Hollow fibre membrane modules	23
2.4.3 Advantages and drawbacks of MBSX.....	25
2.4.4 Applications of MBSX	27
2.5 MBSX of Zr and Hf.....	29
2.6 Modelling MBSX mass transfer.....	30
2.6.1 Mass balance	31
2.6.2 Mass flux.....	32
2.6.3 Overall mass transfer coefficient.....	34
2.6.4 Membrane mass transfer coefficient.....	35
2.6.5 Lumen-side mass transfer coefficient	36
2.6.6 Shell-side mass transfer coefficient	37
2.7 Process parameters.....	39

2.8	Conclusion	40
3	Materials and methods.....	41
3.1	Chemical reagents	41
3.2	Equipment	42
3.2.1	Hollow fibre membrane module	42
3.2.2	Solution analysis	43
3.3	Experimental procedures	44
3.3.1	Solution preparation	44
3.3.2	Salt purity analysis.....	44
3.3.3	Liquid-liquid equilibria (LLE) batch procedure	44
3.3.4	MBSX	45
3.4	Uncertainty analysis.....	48
4	Results and modelling	49
4.1	Introduction.....	49
4.2	Liquid-liquid extraction	49
4.3	MBSX	52
4.3.1	Influence of the shell-side velocity	55
4.3.2	Influence of the lumen-side velocity.....	59
4.4	Mass transfer modelling.....	61
4.4.1	Overall mass transfer coefficient.....	62
4.4.2	Individual mass transfer coefficients	64
5	Design of an industrial MBSX unit	70
5.1	Introduction.....	70
5.2	Design specifications	70
5.3	Membrane module specifications.....	70
5.4	Model development.....	71
5.5	Model application.....	73
5.5.1	Initial values.....	73
5.5.2	Application of the algorithm	74
5.5.3	MBSX unit configuration	76
5.6	Modelling results.....	77
6	Conclusions and recommendations	80
6.1	Conclusions	80
6.1.1	LLE.....	80
6.1.2	MBSX.....	80
6.1.3	Mass transfer modelling.....	81
6.1.4	Industrial estimation.....	81
6.2	Recommendations.....	82
7	References.....	85
	Appendix A.....	XI
	Appendix B.....	XVIII

List of Tables

Table 2-1: Examples of the Zr and Hf SX systems.	16
Table 2-2: A summary of the SX process proposed by Wang & Lee (2016).	20
Table 2-3: Variations in the overall mass transfer coefficient of MBSX in published literature. .	34
Table 2-4: Shell-side Sherwood relations from literature.	38
Table 3-1: List of chemical reagents used.	41
Table 3-2: The Liqui-Cel™ 1.7x8.75 Minimodule specifications.	43
Table 4-1: The parameter values used to determine the individual mass transfer coefficients..	66
Table 5-1: Liqui-Cel™ EXF 8x20 hollow fibre membrane module specifications.	71
Table 5-2: Summary of the industrial-scale cases.	78
Table A-1: The raw data used to determine the purity of the Zr(Hf)(SO ₄) ₂ (H ₂ O) ₄ salt.	XIV
Table A-2: The data used to determine the LLE experimental uncertainty.	XV
Table A-3: The MBSX data used to determine the Zr experimental uncertainty.	XV
Table A-4: The MBSX data used to determine the Hf experimental uncertainty.	XVI
Table B-1: LLE raw data for low D2EHPA concentration range.	XIX
Table B-2: LLE raw data for high D2EHPA concentration range.	XX
Table B-3: Populated LLE data table for low D2EHPA concentration range.	XXI
Table B-4: Populated LLE data table for high D2EHPA concentration range.	XXII
Table B-5: The measured Zr concentration (in g.L ⁻¹) data for the shell-side and lumen-side velocity variation series of experiments.	XXV
Table B-6: The measured Hf concentration (in g.L ⁻¹) data for the shell-side and lumen-side velocity variation series of experiments.	XXVII
Table B-7: The normalised Zr concentration (in g.L ⁻¹) data for the shell-side and lumen-side velocity variation series of experiments.	XXIX
Table B-8: The normalised Hf concentration (in g.L ⁻¹) data for the shell-side and lumen-side velocity variation series of experiments.	XXX
Table B-9: The Zr shell-side concentration, mass flux, and overall MTC data for the shell and lumen velocity variation series of experiments.	XXXIII
Table B-10: The Hf shell-side concentration, mass flux, and overall MTC data for the shell and lumen velocity variation series of experiments.	XXXIV
Table B-11: Parameters for estimating the individual mass transfer coefficients.	XXXVI
Table B-12: The Zr mass transfer data table for the MBSX series of experiments.	XXXVII
Table B-13: The Hf mass transfer data table for the MBSX series of experiments.	XXXVII
Table B-14: Objective function error for Zr model.	XXXIX
Table B-15: Objective function error for Hf model.	XXXIX

List of Figures

Figure 1-1: Project flow sheet.	5
Figure 2-1: A typical three step SX process.	12
Figure 2-2: Membrane based solvent extraction through a hollow fibre membrane	22
Figure 2-3: Liqui-Cel Extra-Flow module diagram featuring cross-flow design.....	23
Figure 2-4: The differential control volume created over aqueous phase (shell-side).	32
Figure 2-5: The resistance-in-series mass transfer model.....	33
Figure 3-1: Cut-away image of the construction of a typical parallel-flow hollow-fibre membrane module.....	43
Figure 3-2: MBSX experimental schematic.	46
Figure 4-1: The effect of D2EHPA concentration on the extraction of Zr and Hf.	50
Figure 4-2: The effect of D2EHPA concentration on the separation between Zr and Hf.	51
Figure 4-3: The effect of D2EHPA concentration on the partition coefficients of Zr and Hf.	52
Figure 4-4: A colour-enhanced photo illustrating shell-side channelling and lumen-side maldistribution.....	53
Figure 4-5: The shell-side outlet Zr concentration as a function of time and shell-side velocity.	56
Figure 4-6: The shell-side outlet Hf concentration as a function of time and shell-side velocity.	56
Figure 4-7: The effect of the shell-side velocity on the extraction of Zr and Hf.	57
Figure 4-8: The effect of the shell-side velocity on the mass flux of Zr and Hf.	58
Figure 4-9: The shell-side outlet Zr concentration as a function of time and lumen-side velocity.	60
Figure 4-10: The shell-side outlet Hf concentration as a function of time and lumen-side velocity.	60
Figure 4-11: The effect of the lumen velocity on the mass flux of Zr and Hf.	61
Figure 4-12: The effect of the shell and lumen velocity on the overall MTC of Zr.....	63
Figure 4-13: The effect of the shell and lumen velocity on the overall MTC of Hf.	64
Figure 4-14: The relative contributions of the shell, membrane, and lumen to the total resistance to mass transfer of Zr and Hf.....	65
Figure 4-15: Comparison of shell-side Sherwood relations from literature to the experimental Zr data.....	66
Figure 4-16: Comparison of shell-side Sherwood relations from literature to the experimental Hf data.....	67
Figure 4-17: Experimental vs. calculated Zr mass flux values for fitting of the Sherwood relation.	69
Figure 4-18: Experimental vs. calculated Hf mass flux values for fitting of the Sherwood relation.	69
Figure 5-1: The control volume created over a portion of the membrane contactor.	72

Figure 5-2: Design equation algorithm.	75
Figure A-1: A section of the ShellSol 2325 data sheet.	XI
Figure A-2: A partial section of the data sheet for the Minimodules™ used in the present study.	XII
Figure A-3: A dimensional drawing of the Minimodules™ used in the present study.	XIII
Figure B-1: The effect of the D2EHPA to metal molar ratio on the partition coefficients of Zr and Hf.	XXIII
Figure B-2: The effect of the D2EHPA to metal molar ratio on the separation between Hf and Zr.	XXIII
Figure B-3: The shell-side Zr outlet concentration as a function of time and shell-side velocity.	XXV
Figure B-4: The shell-side Zr outlet concentration as a function of time and lumen-side velocity.	XXVI
Figure B-5: The shell-side Hf outlet concentration as a function of time and shell-side velocity.	XXVI
Figure B-6: The shell-side Hf outlet concentration as a function of time and lumen-side velocity.	XXVII
Figure B-7: The normalised shell-side Zr outlet concentration as a function of time and shell-side velocity.	XXIX
Figure B-8: The normalised shell-side Zr outlet concentration as a function of time and lumen-side velocity.	XXX
Figure B-9: The normalised shell-side Hf outlet concentration as a function of time and shell-side velocity.	XXXI
Figure B-10: The normalised shell-side Hf outlet concentration as a function of time and lumen-side velocity.	XXXI
Figure B-11: The effect of the shell and lumen flow velocity on the mass flux of Zr.	XXXIII
Figure B-12: The effect of the shell and lumen flow velocity on the mass flux of Zr.	XXXIV
Figure B-13: The contribution of the individual resistances to the total resistance to mass transfer for $U_{Shell} = 1.7 \times 10^{-2} \text{ m.s}^{-1}$	XXXVIII
Figure B-14: The experimental vs. calculated Zr mass flux values for fitting of the Sherwood relation.	XL
Figure B-15: The experimental vs. calculated Hf mass flux values for fitting of the Sherwood relation.	XL

List of Symbols

Nomenclature			Subscripts	
A	Surface Area	m^2	Aq	Aqueous
A_c	Cross sectional area	m^2	Eq	Equilibrium
C	Concentration	$kg.m^{-3}$ or $g.L^{-1}$	H	Hydraulic
d	Diameter	m	i	Component
D_{AB}	Diffusion Coefficient	$m^2.s^{-1}$	ID	Internal diameter
HA	Protonated carrier molecule	-	in	Into control volume
j	Mass flux	$kg.m^{-2}s^{-1}$	L	Lumen
k	Mass Transfer Coefficient	$m.s^{-1}$	LM	Logarithmic mean
K_{eq}	Equilibrium constant	-	Mem	Membrane
K_{OV}	Overall MTC	$m.s^{-1}$	OD	Outer diameter
k	Individual MTC		Org	Organic
L	Length	m	out	Out of control volume
g, m, n	Stoichiometric constant	-	OV	Overall
MW_B	Molecular weight	$g.mol^{-1}$	S	Shell
N_{Fibres}	Number of fibres	-	x, y	Direction, x- or y-axis
$N_{Parallel}$	Number of columns in parallel	-	Superscripts	
N_{Series}	Number of modules in series	-	Bulk	Bulk phase
P	Partition Coefficient	-	Eq	Equilibrium
Q	Volumetric flow rate	$m^3.s^{-1}$	exp	Experimental
R	Mass transfer resistance	$s.m^{-1}$	final	Integral end point
SF	Separation factor	-	In	In flow
SR	Separation ratio	-	Int	Interface
T	Temperature	K	Out	Out flow
U	Superficial velocity	$m.s^{-1}$	Dimensionless groups	
V	Volume	m^3	Gz	Graetz = $UD_H^2/D_{AB}L$
v_A	Molecular volume	$m^3.mol^{-1}$	Re	Reynolds = $\rho UD_H/\mu$
Greek letters			Sc	Schmidt = $\mu/\rho DAB$
α, β	Model fitting parameters	-	Sh	Sherwood = $k_i D_H/D_{AB}$
δ	Thickness	m		
Δ	Delta	-		
ϵ	Porosity	-		
r	Fibre packing factor	-		
r	Dynamic viscosity	Pa.s		
ρ	Density	$kg.m^3$		
τ	Tortuosity	-		
Φ	Wilke-Chang association factor	-		
φ	Volume fraction	-		
ω	Molar fraction	-		

List of Abbreviations

BLM	Bulk liquid membrane
CESUZ	Compagnie Européenne du Zirconium
CFD	Computational fluid dynamics
E:M	Extractant to metal ratio (mol:mol)
HF	Hollow fibre
HFSLM	Hollow fibre supported liquid membrane
IQR	Interquartile range
L-L	Liquid-liquid
LLE	Liquid-liquid equilibria
LM	Liquid membrane
MBSS	Membrane based solvent stripping
MBSX	Membrane based solvent extraction
MIBK	Methyl isobutyl ketone
MTC	Mass transfer coefficient
O:A	Organic to aqueous volumetric phase ratio
ppm	Parts per million
PX	Pertraction
R-i-S	Resistance-in-series
rpm	Revolutions per minute
RTD	Residence time distribution
SLM	Supported liquid membrane
SX	Solvent extraction
TBP	Tributyl phosphate

1 Introduction

1.1 Background and motivation

The discovery of zirconium (Zr) is attributed to Martin Heinrich Klaproth, who first separated zirconia (ZrO_2) from zircon ($ZrSiO_4$) in 1789 [1]. However, it was not until 1824 that the first sample of metallic Zr was produced by Jöns Berzelius, by heating potassium hexafluorozirconate (K_2ZrF_6) in the presence of potassium [1,2]. Unbeknownst to both Klaproth and Berzelius, this sample of metal contained an undiscovered impurity which would be revealed by George Charles de Hevesy and Dirk Coster nearly a century later, in 1923, that would become known as Hafnium (Hf), with the first pure sample to only be produced in 1925 [1]. The separation of Zr and Hf was noted to be difficult, and the significant period of time between the discovery of the two elements was attributed to this challenge, which is the result of the extraordinary chemical similarity of Zr and Hf [1,3–5].

Naturally-occurring Zr contains between 2 and 3 wt% Hf, and for many of its uses (such as refractories, gemstones, enamels, abrasive grits, and dye pigments) the chemical similarity between the two elements negates the need for separation [2,5–9]. Both Zr and Hf are ductile and high melting point metals with a high corrosion resistance even at elevated temperatures, making them ideal candidates for the aggressive conditions inside nuclear reactors [5,10]. The most notable difference between these elements lies in their interaction with thermal neutrons. Zr has a thermal neutron capture cross-section of 0.18 barn, making it almost transparent to thermal neutrons, whereas the thermal neutron capture cross-section of Hf is around 640 times larger than that of Zr at 115 barn, making it an excellent neutron absorber [2,3,11]. The transparency of Zr and opacity of Hf, along with the other mentioned properties, make these metals well suited to their opposing roles of fuel cladding and control rods, respectively [12,13]. It is easily understood that the amount of neutron-absorbing Hf in the Zr used for cladding will have a notable impact on the process efficiency, and hence, the cost of the power produced [14]. Therefore, in order for any Zr alloy to be suitable for use in nuclear reactors it is vital that the Hf content of does not exceed 100 parts Hf per 1 million parts Zr ppm [5,6,11,15]. Accordingly, any further references to nuclear-grade Zr will imply a Hf content of 100 ppm or less.

With the development and expansion of the nuclear industry the need for purified Zr and Hf became imperative, as did the need for an industrial-scale separation process. Solvent extraction (SX) was identified as an economically viable approach, and the Hf-selective methyl isobutyl ketone (MIBK) and the Zr-selective tributyl phosphate (TBP) processes were both developed around the late 1940s to mid-1950s [6]. Both of these processes have been and continue to be used industrially to produce industrial-grade Zr for the nuclear industry [14,16].

In terms of the separation processes suitable for such a purification of Zr and Hf, the advantages of SX processes include: continuous operation, simple equipment, relatively few moving parts, and low temperature conditions, while, the major drawbacks relate to the dispersion of phases to create enough surface area for effective mass transfer [8,17]. For industrial SX, mixer settlers are commonly used process units, which disperse the phases by mechanical agitation. After mixing, the combined phases flow into a settling section, where the phases are allowed to separate based on their density differences. However, drawbacks of direct-contact equipment such as mixer settler units include: i) the time required to separate the phases, which results in large settling sections and therefore chemical inventory, ii) a density difference required between the solutions for separation, iii) the limited range of phase ratios that can be used without concern of flooding or unloading, iv) the difficulty of accurately predicting the interfacial area between the phases, and v) the scaling-up of SX processes, which is usually non-linear and can be difficult [8,17–19].

Due to the widespread application and relatively simple operation of SX, a number of efforts to address some of the drawbacks related to direct-contact equipment have been investigated. One improvement which has become popular entails the addition of a porous membrane to create an immobilised liquid-liquid (L-L) interface between the phases, thereby avoiding the phase dispersion, while still allowing for mass transfer between the phases [17].

The inclusion of a barrier material to immobilise an interface is often classified as a type of liquid membrane (LM), which, depending on the exact configuration, generally falls into either supported liquid membranes (SLM) or bulk liquid membranes (BLM) subtypes [20]. According to Schlosser & Marták (2009), an LM is created when two miscible fluids are separated by a liquid which is immiscible in the other two fluids while still allowing mass transfer [21]. The specific technique utilised in the present study, which is also known as membrane based solvent extraction (MBSX), falls under the bulk liquid membrane division.

The immobilisation of the aqueous-organic interface in a microporous membrane offers a number of advantages over traditional SX, including: i) a fixed interfacial area, ii) no density difference required between the phases used, iii) independent control of the hydrodynamic conditions of each phase, iv) few moving parts, and v) the ease of scalability [17]. In addition, the separation of phases using membranes completely negates the equipment and time requirements of the mixer settlers commonly used in traditional SX plants, resulting in reduced chemical inventories and smaller overall plant footprint. The reduced plant size and lack of moving parts can also reduce downtime required for maintenance, making this technology even more attractive for industrial application [17].

The inclusion of a membrane separator during the SX of Zr and Hf has received attention from researchers as far back as 1983, when Gasparini *et al.* investigated the extraction of plutonium

and Zr through SLM's [22]. Between 1989 and 1992, Chaudry & Malik (as reported by Yang *et al.* (2002)) investigated the transport of Zr and Hf from a nitrate medium through flat sheet SLM's impregnated with TBP [14]. Yang *et al.* (2002) also detailed the separation of Zr and Hf through hollow fibre SLM's from a chloride medium using Aliquat 336 (tri-n-monomethyl ammonium chloride) as carrier [14]. Despite the extensive availability of literature focussing on MBSX, an approach to assess the technical feasibility of industrial-scale processes is not readily available. This is especially true for Zr and Hf, as the literature which has been published, such as by Yang *et al.* (2002), is not detailed enough to predict the suitability of MBSX for the industrial-scale separation of Zr and Hf [14].

1.2 Problem statement

The high manufacturing cost of membranes and membrane contactors have limited the interest of both researchers and industry in the development of MBSX technology. The resulting lack of research data prohibits both i) the modelling of these processes and ii) the estimation of the potential for industrial-scale implementation of such technology. This project was therefore aimed at developing an approach to assess the technical feasibility of MBSX to industrial scale use.

1.3 Aim and objectives

The aim of the study was to develop an approach which could be used to predict the technical feasibility of the industrial-scale application of MBSX. This required combining experimental data with a predictive process model.

Most of the experimental data was generated to sufficiently predict the behaviour of the MBSX system pertaining to this study. Therefore, data was collected that could be used to estimate mass transfer behaviour rather than determining a set of optimal operation conditions. This is further discussed in Section 1.4.3.

The objectives of the study were essentially twofold, firstly, data gathering, which consisted of experimental work and secondly the modelling, consisting of the development and application of a process model based on the experimental data to estimate an industrial MBSX unit.

The data gathering objectives of the study were defined as:

- Determine the ideal D2EHPA concentration for the MBSX experiments as well as the corresponding partition coefficients of Zr and Hf by means of liquid-liquid equilibria.
- Determine the magnitude of the mass flux of Zr and Hf as well as the effects of the shell-side and lumen-side flow velocity on the mass flux of a laboratory scale MBSX membrane contactor.
- Determine the experimental mass transfer coefficients of Zr and Hf corresponding to the experimental conditions.

The modelling objectives were defined as:

- Propose a process model to predict the concentration profiles of Zr and Hf along an MBSX column.
- Using the experimental data, predict the concentration profiles and separation efficiency of a single MBSX column.
- Estimate the required membrane surface area, and the series and parallel configuration of an industrial-scale MBSX unit.
- Evaluate the modelling outcomes, and draw conclusions from the proposed approach and the feasibility of MBSX for the industrial-scale separation of Hf from Zr.

1.4 Scope and limitations

1.4.1 Experimental and modelling outcomes

The final outcome of the study was the development of a method with which small-scale experimental data could be used to estimate the feasibility of an MBSX system for industrial-scale application. This study served as the first step during which a simple approach was developed that could be improved in subsequent studies to compile a more comprehensive assessment method, for example by including additional variables.

For this study, Hf represented the minor component (with a mass ratio between Hf and Zr of approximately 50:1), and the potential financial and plant-size implications related to the minor-component selective extraction using readily available chemicals was the primary motivator for the choice of the chemical system used in this study. Based on this, the Hf-selective D2EHPA- H_2SO_4 system was used.

The modelling required that the partition coefficients (to be obtained from the LLE data), as well as the influence of both the shell and lumen velocities on the overall mass transfer coefficients (K_{OV} , to be obtained from the MBSX experiments) of Zr and Hf be known in order to estimate the total surface area, and combination of series and parallel membrane modules that would be required for an industrial-scale MBSX unit.

1.4.2 Order of operations

This project was executed according to the process illustrated in Figure 1-1.

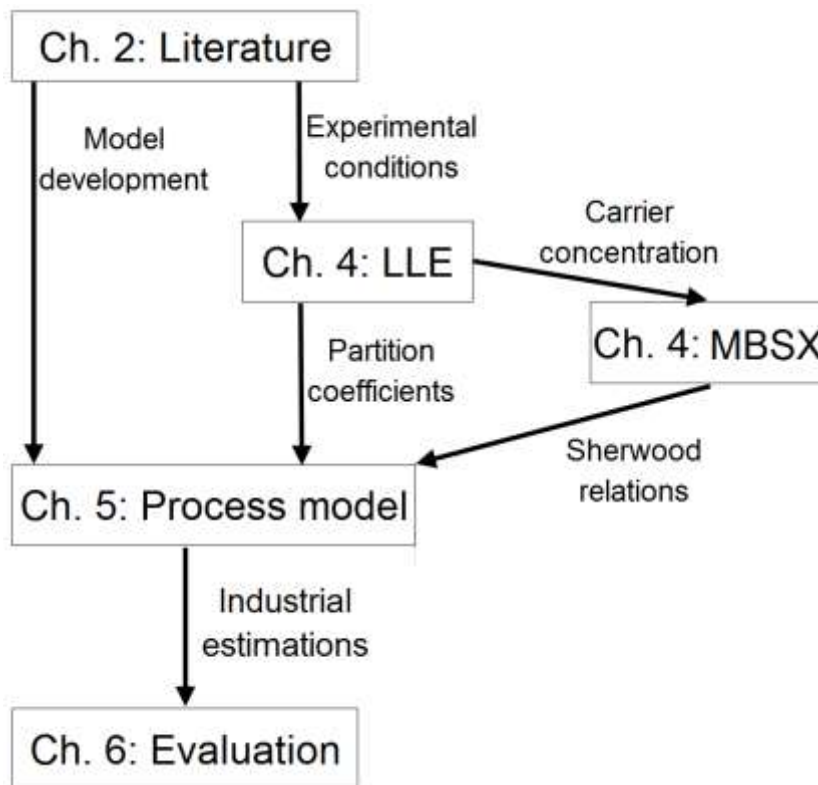


Figure 1-1: Project flow sheet. LLE – liquid-liquid equilibria. MBSX – membrane based solvent extraction.

Information from existing literature will be used to determine the makeup of the aqueous phase, focussing on the work by Wang & Lee (2016) who investigated a similar chemical system as was used in this study, with the only change being that the metal concentration in this study was increased to 16 g.L^{-1} Zr, compared to the 10 g.L^{-1} Zr used by Wang & Lee (2016) [23]. The motivation for using an increased metal feed concentration was to improve the alignment with the expected concentrations of industrial scale operations.

The experimental work of this study consisted of two data groups, namely the LLE and the MBSX sets. Firstly, the LLE data was collected with the purpose of providing the best carrier concentration for the subsequent MBSX experiments, as well as the partition coefficients of Zr and Hf at the relevant carrier concentration. Secondly, the MBSX experiments were used to investigate the effect of the fluid velocity on the overall rate of mass transfer that can be achieved in a laboratory-scale MBSX column.

Based on available literature, and using the experimental data obtained, a process model was developed to predict the total surface area required to produce 100 kg.hr^{-1} nuclear-grade Zr. In 2016, South Africa was responsible for the production of approximately 370 000 metric tons of ZrSiO_4 [24]. The proposed production rate of 100 kg.hr^{-1} Zr equates to converting approximately 1% of the Zr metal in the mined ZrSiO_4 to nuclear-grade purity.

1.4.3 Constraints

The two main factors that constrained the experimental design were i) the aim of generating data for the development of a basic model and assessment methodology, and ii) the financial limitations of the project.

As a significant amount of literature data on the SX separation of Hf from Zr has already been published (see Chapter 2) and advanced knowledge of an optimal set of operating conditions were not primary objectives for the development of the model and assessment methodology, the optimisation of the chemistry of the D2EHPA-H₂SO₄ system was not further considered. Furthermore, the aqueous and organic speciation and reaction mechanisms of Zr and Hf are known to be complex and fell beyond the scope of this study [25]. While many studies have used low feed concentrations (at or below 1.0 g.L⁻¹ Zr), this would not be suitable for industrial applications [13,26–28]. In accordance, the Zr feed concentration was increased by approximately one order of magnitude to 16 g.L⁻¹ Zr (0.36 g.L⁻¹ Hf), as discussed in Section 1.4.2. The only chemistry-related investigation of this study was to determine a suitable carrier concentration for the MBSX experiments at the increased feed concentration. The selection of the carrier did not form part of the study. D2EHPA was chosen based on its relatively low cost, wide availability at large scale, and generally long operational lifespan, all of which makes it an attractive option for the industrial scale application of MBSX [29].

The pH of the aqueous solution, specifically, was not measured for two reasons. Firstly, the chosen acid concentration of 98 g.L⁻¹ (1.0 M) H₂SO₄ would produce a pH of around 0, which falls outside the range of accurate measurements. Secondly, since the extraction of Zr and Hf was relatively low, the pH changes would be smaller than the measurement uncertainty of the available meters. It should be noted that the actual feasibility of the D2EHPA-H₂SO₄ system was not regarded as paramount for the success of this study as long as the data that was generated were sufficient for the development of the assessment method.

While the available analytical techniques were suitable for determining the metal content in the aqueous phase, these techniques could not be used for the analysis of the organic phase. This implies that the mass transfer could only be accurately determined with the fresh organic phases. The lack of data of the organic phase also limited the extent to which the MBSX mass balance could be validated. To avoid the influences of the above-mentioned changes, a once-through methodology was adopted for the MBSX experiments.

The majority of industrial SX processes consist of three steps, namely, extraction, scrubbing, and stripping. This study focused only on the first step, i.e. the extraction of Zr and Hf from a mixed solute aqueous stream.

The range of flow rates tested through the MBSX column was determined by various equipment limitations. At high flow rates, the relatively low permeation rates resulted in the measured concentration difference between the membrane column inlet and outlet approaching the uncertainty limit of the ICP-OES, while the lowest flow rates were based on ensuring a stable flow for the duration of the experiments

Empirical Sherwood relations were used to describe the mass transfer coefficients, and it is assumed that the mass transfer behaviour of a larger module would be similar to the experimental modules if the Reynolds number was kept constant.

1.5 Dissertation layout

This document is divided into six chapters.

The introductory chapter (Chapter 1) provides an overview of the context related to Zr/Hf separation, a proposed improvement over the current technology, and the literature gap that exists. The aim, objectives, and limitations of the study are also discussed.

Chapter 2 covers five main topics. First, a short overview on the current worldwide production of Zr and Hf. Second, the separation of these metals through means of SX, including current industrial processes and some laboratory-scale research. Third, the use of liquid membranes is discussed. Fourth, the literature specifically related to the MBSX of Zr and Hf is discussed, before lastly, explaining the modelling of a typical MBSX unit.

Chapter 3 provides the materials used and procedures followed. Chemical and equipment specifications are provided, followed by discussions of the procedures of the Zr(Hf)SO₄ purity analysis, LLE experiments, MBSX experiments, and uncertainty analysis.

In Chapter 4, the results obtained from the LLE and MBSX experiments, and the mass transfer behaviour and modelling, are discussed. The LLE data gathered is presented initially, along with the determined partition coefficients for Zr and Hf. Next, the MBSX data, consisting of lumen and shell velocity variations, are discussed. The final part of the chapter details the development of the mass transfer model that was used in this study, the resistance-in-series approach that was used to describe the mass transfer, and the Sherwood relations used to estimate the mass transfer coefficients.

Subsequently, in Chapter 5, the target specifications, the process model development, the design algorithm and estimation approach are discussed. The chapter is closed off with discussions of the industrial cases, including the total surface area, and the configuration of series and parallel membrane modules that would be required to produce 100 kg.hr⁻¹ nuclear grade Zr.

Finally, Chapter 6 closes off the dissertation with conclusions and comments on Chapters 4 and 5. A number of recommendations are presented regarding the possible improvements to the design approach, the industrial implementation of MBSX, and further research options.

2 Literature

The following literature chapter deals with two topics pertaining to the present study. The first part focuses mainly on SX, emphasising the literature related to Zr and Hf separation. The second part of this chapter describes MBSX and the mass transfer related to such systems.

In the first section, the production process of Zr metal and general SX is discussed, followed by a more detailed discussion of the TBP and MIBK processes, both of which are used industrially for the production of nuclear-grade Zr. A brief discussion of the extensive literature of Zr and Hf SX is presented with a focus on the organophosphorus-sulphate based system.

In the second section, the principles and configurations of membrane-based SX processes is discussed, followed by the modelling of an MBSX system consisting of aqueous and organic phases separated by a membrane.

2.1 Overview of Zr and Hf production

This section provides a brief description of the process of transforming Zr ore into nuclear-grade metal. The separation of Zr and Hf is discussed in detail in Section 2.2 and 2.3. The most common sources of Zr and Hf are zircon (Zr(Hf)SiO_4) and baddeleyite (Zr(Hf)O_2), of which zircon is far more abundant [27]. The world-wide production of Zr(Hf)SiO_4 in 2016 was approximately 1.38 million metric tons, with South Africa being the second largest producer with approximately 27% of the total production [24]. Banda & Lee (2014) reported that only approximately 5% of Zr is processed into metallic form, most of which is destined for the nuclear industry [6].

The production of Zr and Hf metal from ore typically follows five stages, namely, i) the decomposition of the ore, ii) the separation of the Zr and Hf, iii) calcination, iv) chlorination, and v) the reduction to a metal [27]:

The decomposition of the ore is typically done either by carbo-chlorination or alkali fusion. During carbo-chlorination, chlorine gas and solid carbon is reacted with Zr(Hf)SiO_4 at 1200 °C inside a fluidised bed reactor in which ZrCl_4 and HfCl_4 products are formed. During the alkali fusion process, the Zr(Hf)SiO_4 is heated to 900 – 1200 °C in the presence of either sodium carbonate (Na_2CO_3) or sodium hydroxide (NaOH). Fusion with Na_2CO_3 requires additional acid leaching to remove the Zr and Hf from the $\text{Na}_2\text{Zr(Hf)SiO}_5$ product, while the fusion with NaOH produces $\text{Na}_2\text{Zr(Hf)O}_3$ which can be easily removed using water. The decomposition of the ore serves to remove silicon but does not result in any separation of the Zr and Hf [27].

Following the decomposition, the second, and most important, step in the process is the separation of Zr from Hf, which is also the major focus of the literature discussed in Section 2.2. While a number of techniques are available, including selective crystallisation, ion-exchange, molten salt distillation, and SX, currently the CESUZ, TBP, and MIBK processes are used for

nearly all industrial separations of Zr and Hf, with the TBP and MIBK processes being utilised in the majority of cases. [26–28]. The mentioned processes are discussed further in the Section 2.2.1 (CEZUS), 2.2.2.2 (TBP), and 2.2.2.3 (MIBK).

After separation, the purified Zr and Hf products are typically converted to pure $ZrCl_4$ and $HfCl_4$, which are, penultimately reduced to metal using molten magnesium (Kroll process) which produces a metallic sponge that can be further processed into a solid metal [27].

2.2 The separation of Zr and Hf

A number of separation processes have been developed and utilised industrially with the CEZUS, TBP, and MIBK processes being the most common [6]. The CEZUS process is a pyrometallurgical process based on the difference in volatility of $ZrCl_4$ and $HfCl_4$. The most frequently used TBP and MIBK processes are both hydrometallurgical SX-based processes using organic carriers to selectively extract either Zr or Hf [8].

2.2.1 Pyrometallurgy

The pyrometallurgical CEZUS process utilises the fractional distillation of $Zr(Hf)Cl_4$ to produce nuclear-grade $ZrCl_4$ salt. It was developed by the French company, CEZUS (Compagnie Européenne du Zirconium) in the 1970s with the aim of reducing the number of steps required to produce nuclear-grade Zr [6].

The distillation is performed at 350 °C and atmospheric pressure, where $Zr(Hf)Cl_4$ is dissolved in either $AlCl_3$ -KCl or $FeCl_3$ -KCl solvents, with $AlCl_3$ -KCl being the most commonly used due to the high solubility for $Zr(Hf)Cl_4$ [8]. Since the volatility of $HfCl_4$ is approximately 1.7 times higher than that of $ZrCl_4$ between 152 and 352 °C, the Hf can be selectively removed by distillation, leaving the nuclear-grade $ZrCl_4$ in the solvent [8].

The major advantage of this process is that the $ZrCl_4$ product can be utilised in the Kroll reduction process without any further processing, eliminating the calcination and chlorination steps typically required by SX processes [8]. The drawbacks of this process include: i) the associated high costs, with the construction requiring specialised alloys and maintenance due to the corrosive nature of the chemicals involved in the process, ii) the need to prevent moisture contamination, and iii) the sophisticated technology required to handle a molten salt solvent [6,8].

2.2.2 Solvent extraction (SX)

2.2.2.1 Introduction

SX (also known as liquid-liquid extraction) has been established as a powerful hydrometallurgical tool in the field of separation and has been applied to a vast range of chemical separations, ranging from laboratory-scale preparations to industrial waste treatment and the separation and

purification of metals [6,30]. The separation of components is achieved by the difference in solubility of a component between two immiscible phases [21]. In order to facilitate a high rate of mass transfer, one phase is commonly dispersed into the other to ensure the development of the maximum possible interfacial area between the two phases [21,31]. The maximisation of the interfacial area is one of the main challenges related to the design and operation of dispersion-based SX [17]. The most common methods used to achieve dispersion include packed towers, spray or mixed columns, and mixer settlers [17,32,33]. For packed towers the selection of packing is vital, whereas in the case of mixer settlers, which have moving internals, the droplet size must be minimised, while the number of droplets must be maximised [17,18].

In the case of metal separation, the two phases consist of a solute rich aqueous phase, and an organic phase containing a carrier capable of forming organometallic complexes with the metal solute within the organic phase [30]. The selectivity of the process can be manipulated through the selection of appropriate chemical species (such as the aqueous phase anions, organic phase carriers and modifiers), and operating conditions. The extracted component(s) can be stripped back into an aqueous phase under different chemical conditions or discarded, depending on the product of interest [34].

A typical industrial-scale SX metal separation process is illustrated in Figure 2-1. The initial feed stream (usually an aqueous solution), which is often produced in an ore leaching step, typically contains impurities which need to be removed. The feed enters the extraction unit where it is contacted with a stripped organic phase. The carrier in the organic phase extracts the product and/or impurities by forming organometallic complexes with the metal ions, while the aqueous stream leaves the extraction unit as the raffinate stream. The undesired metals that co-extract must subsequently be scrubbed from the loaded organic phase. This is achieved by contacting the organic phase with a scrub liquor chosen to remove these impurities. The removed impurities can be treated further if necessary. In the final stage, the scrubbed organic phase, containing only the desired metal(s), is contacted with a stripping liquor that has been chosen to remove all the residual metals present in the organic phase.

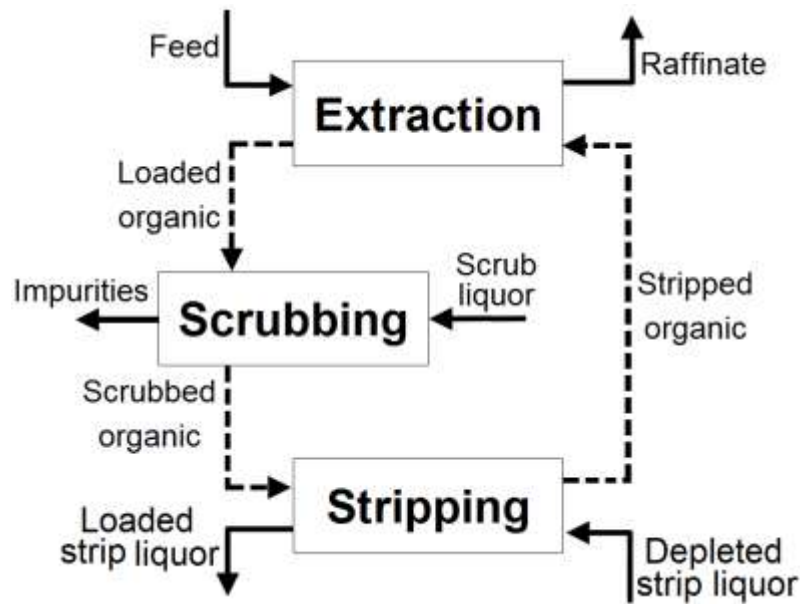


Figure 2-1: A typical three step SX process. The solid lines represent the aqueous phases while the dashed lines represent the organic phase. Redrawn from [17].

This final step serves the dual purpose of regenerating the carrier to be re-used in the extraction stage, while also returning the purified metal(s) to an aqueous phase from which it can be recovered [34]. It is common for the loaded strip liquors to be fed to electrowinning plants in order to recover the metals.

The ease of continuous operation, energy efficiency, and low labour costs have contributed to the success of SX for industrial operations [6,20].

The performance of an SX process is typically defined by the separation factor (SF), Eq. 2-1, and partition coefficients (P), Eq. 2-2, between the components, for example a and b.

$$SF = \frac{P_a}{P_b} \quad 2-1$$

$$P = \frac{C_{org}}{C_{aq}} \quad 2-2$$

The partition coefficient is an indicator of a species' solubility in a certain organic phase. During the design of an SX process, it is desirable to maximise the separation factor in order to minimise the number of equilibrium stages required to achieve the desired purity. In the case where there are no chemical reactions between species in the aqueous and organic phases and the solute(s) exist in a single molecular form (also termed non-reactive systems), the partition coefficient is simply a function of the aqueous phase concentrations and organic-to-aqueous (O:A) phase ratio [35]. However, for reactive systems where chemical reactions between the aqueous and organic phase species are involved (such as the case of metal extractions which require organic phase carriers with which the metal ions can form organometallic complexes), the partition coefficient is

further influenced by the concentrations of the metal and the carrier, the aqueous anionic species, and the specific carrier used. Therefore, the chemical reagents and their concentrations need to be considered carefully during the design of an SX process, as these are important parameters affecting the efficiency of the process.

While the separation of Zr and Hf is known to be notoriously difficult as a result of their nearly identical ionic radii, these two metals do exhibit differences in their interactions with inorganic anions which allows them to be separated using SX [36]. According to Wang & Lee (2016), the high coordination numbers of both Zr and Hf result in their strong tendency to hydrolyse and consequently exist as metal-ion complexes [23]. The tendency of Zr and Hf to complex with anions has been reported to increase in the following order: $\text{Cl}^- < \text{NO}_3^- < \text{SO}_4^{2-} < \text{C}_2\text{O}_4^{2-} < \text{F}^- < \text{OH}^-$, and despite the similar behaviour of the same complexes, differences in the equilibrium and kinetics constants are responsible for the formation of the numerous complexes which can be leveraged to achieve the separation between Zr and Hf [11,23]. There is significant literature providing more information on the properties of Zr and its various associated compounds [1,25,37].

While significant effort has been made to investigate the separation of Zr and Hf using SX (as discussed further in Section 2.3), thus far, the only two SX systems that have been implemented for the industrial scale separation of Zr and Hf are the TBP- and MIBK processes.

2.2.2.2 The TBP Process

The TBP process in which Zr could be selectively extracted by TBP was first proposed by the French Nuclear Agency CEA circa 1954. Researchers at Iowa State University later modified the process to use aqueous solutions consisting of only varying HNO_3 concentrations. The single acid system allowed for the acid solutions to be recycled [6].

In the TBP- HNO_3 process, $\text{Zr}(\text{Hf})\text{O}_2$ is dissolved in an aqueous phase consisting of 3.0 M HNO_3 and 3.5 M NaNO_3 which is contacted counter-currently with 60 vol% TBP diluted with kerosene [6,27,38]. The Zr is selectively extracted from the aqueous solution, with the majority of impurities including Al, Cd, Fe, Mg, Si, and Ti remaining in the aqueous phase [8,27]. The partition coefficients for Zr and Hf that have been reported ranged between 1.5 and 0.15 for the above stated conditions resulting in a separation factor of approximately 10 [6,27,38].

Cox *et al.* (1958) proposed a 14-stage counter-current SX process capable of producing a nuclear-grade Zr rich organic phase. The 14 stages were divided into 10 extraction stages and 4 scrubbing stages. The scrubbing solution was introduced in stage 1, the fresh aqueous feed stream in stage 5 and the fresh organic feed stream in stage 14. The aqueous feed solution consisted of 127 g.L⁻¹ of $\text{Zr}(\text{Hf})\text{O}_2$ diluted to 53 g.L⁻¹ of $\text{Zr}(\text{Hf})\text{O}_2$ in stage 5, containing 2.4 % Hf, in 5.1M HNO_3 . The organic phase consisted of 60 vol% TBP in n-heptane, while the scrubbing

solution contained 5.4 M HNO₃. The authors reported separation factors that varied between 3 and 30 for a single stage. The aqueous raffinate at the outlet of stage 14 was reported to contain approximately 3.54 g.L⁻¹ of Zr(Hf)O₂ with 7.2 % Hf. The organic phase leaving at stage 1 contained 22.2 g.L⁻¹ ZrO₂ with less than 0.01% Hf. This organic phase was then stripped with water to recover the Zr and regenerate the TBP. [5]

The TBP-HNO₃ process has a few advantages such as the high selectivity toward the extraction of Zr [6,8]. However, specific drawbacks decrease the attractiveness of the process. These include: i) severe corrosion of process equipment due to the aggressive nature of the acidic aqueous solutions [8], ii) the formation of stable emulsions at high metal concentrations, limiting the Zr concentration to around 30 g.L⁻¹ (around 40 g.L⁻¹ ZrO₂) [6,8], iii) the process is incapable of producing a high purity Hf product [6], iv) the large consumption of chemicals as the major component is selectively extracted [6,27,38], and v) compared to the MIBK process the TBP process is nearly twice as expensive, due to the large chemical inventories and the increased size of the equipment [6].

2.2.2.3 The MIBK process

The MIBK process is a process in which Hf is selectively extracted from a thiocyanate complex aqueous solution into an organic phase consisting of a thiocyanic acid-MIBK mixture [29].

The MIBK process requires more steps than the TBP process as the Zr(Hf)(OH)₂Cl feedstock must be converted into Zr(Hf)-[S=C≡N-] complexes using ammonium thiocyanate [8,29]. The thiocyanate solution is then contacted counter-currently with a solution of MIBK and thiocyanic acid where the Hf is selectively extracted [8]. Between 12 and 15 stages are required to produce a raffinate stream containing less than 0.0025% (25 ppm) Hf while the organic stream typically contains less than 1% Zr impurity [8]. The process has been reported to achieve a separation factor of around 7 [6].

This process has a number of advantages which has resulted in approximately two thirds of nuclear-grade Zr being produced using the MIBK process [6]. The major advantage relates to the selective extraction of Hf, which, as the minor component, is desirable due to improved process economics, as the chemical inventory and equipment sizes of downstream units are both significantly reduced in comparison to the TBP process [13,39,40]. The high organic phase loading capacity, high energy efficiency, and high purity product streams are further boons to the process' economics [6,8,13]. However, the drawbacks are also significant and should be carefully considered. The major drawbacks include: i) a high chemical consumption related to the high solubility of MIBK in water [6,26,38,40], ii) a low flash point of MIBK resulting in flammability concerns [6,26,39,40], iii) a high vapour pressure of MIBK resulting in evaporative losses of the organic phase [26,38], iv) environmental concerns related to the toxic by-products including

ammonium, cyanide, and organic by-products which can be discharged with waste streams [6,27,38–40], and v) the significant solubility ($\pm 2\%$) of MIBK in the aqueous phase [6,8,26,38,40].

2.3 Novel SX approaches

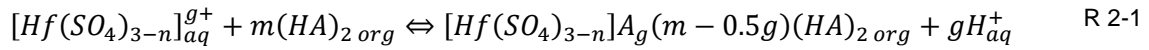
The concerns related to the TBP and MIBK processes, as well as the development of new carriers, have prompted researchers to investigate numerous different combinations to improve the separation of Zr and Hf. Banda & Lee (2015) published an in-depth paper of the various methods of separating Zr and Hf [6]. Amaral & Morais (2016) investigated the separation of Zr and Hf using a wide range of carriers in both hydrochloric and nitric acid media [15]. Wang & Lee (2016) published a review article which summarised a vast amount of literature on the SX of Zr and Hf, providing an in-depth discussion of the aqueous chemistry of Zr and Hf, and the interactions of various carriers (acidic, solvating, and amine) with different anion (chloride, nitrate, and sulphate) systems [27]. Readers are advised to review the above-mentioned articles for more detail on the SX chemistry of Zr and Hf. A number of the SX chemical systems that have been investigated are listed in Table 2-1. The table contains the aqueous medium, organic carrier, and various concentrations correlating to the highest equilibrium separation factors reported in the specific article. It is notable that the majority of the investigated systems were Zr-selective, while most of the Hf-selective systems were related to the organophosphorus (such as D2EHPA (bis-(2-ethylhexyl)phosphoric acid) or Cyanex 272 (Bis (2,4,4-trimethylpentyl) phosphinic acid)) and H_2SO_4 systems.

The development of a minor component (Hf) selective system is naturally attractive due to the potential cost savings associated with smaller plants and less environmental pollution. While the Cyanex 272- H_2SO_4 would seem to be an ideal choice due to the high separation factor (24), the cost of Cyanex 272 and the highly corrosive nature of the aqueous phase due to the high acid concentration (588 g.L^{-1}) must be carefully considered. While the separation factor (8.8) of the D2EHPA- H_2SO_4 system seems lacklustre in comparison, D2EHPA is an affordable and widely available alternative to Cyanex 272, while allowing lower acid concentrations to be used. In line with the aim of this study, the following section provides an overview of the research focussing on the selective extraction of Hf specifically using a D2EHPA- H_2SO_4 system.

Table 2-1: Examples of the Zr and Hf SX systems and the separation factor at equilibrium conditions presented in literature.

Acid	[Acid] (g.L ⁻¹)	[Metal] (g.L ⁻¹)	Carrier, [C] (g.L ⁻¹)	Carrier type	Selectivity	Separation factor	Ref.
HCl	11	Zr = 15 Hf = 0.6	D2EHPA, 483	Phosphoric acid	Zr	1.6	[16]
	146	Zr = 0.18 Hf = 0.18	Cyanex 272, 2.9	Phosphinic acid	Zr	8.7	[11]
	11	Zr = 0.09 Hf = 0.18	Cyanex 302, 0.6	Thiophosphinic acid	Zr	7.8	[42]
	73	Zr = 0.09 Hf = 0.18	LIX 84 IC, 26.3	Oxime	Hf	3.6	[43]
	365	Zr = 15 Hf = 0.6	TBP, 399.5	Phosphate	Zr	21.4	[15]
HNO ₃	126	Zr = 15 Hf = 0.6	Cyanex 272, 435	Phosphinic acid	Zr	26.4	[16]
	126	Zr = 0.1 Hf = 0.1	Cyanex 923, 87	Alkylphosphine	Zr	28	[45]
	252	Zr = 15 Hf = 0.6	D2EHPA, 483	Phosphoric acid	Zr	1.3	[15]
	441	Zr = 15 Hf = 0.6	TBP, 399.5	Phosphate	Zr	51.3	[16]
H ₂ SO ₄	49	Zr = 0.2 Hf = 0.2	Alamine 308, 5.3	Amines	Zr	12.4	[40]
	392	Zr = 10 Hf = 0.2	D2EHPA, 16.7	Phosphoric acid	Hf	7.6	[17]
	98	Zr = 10 Hf = 0.2	D2EHPA, 22.5	Phosphoric acid	Hf	8.8	[24]
	588	Zr = 10 Hf = 0.2	Cyanex 272, 20.3	Phosphinic acid	Hf	24	[16]

Wang & Lee (2016) sought to determine the reaction mechanisms with which D2EHPA and PC 88A (2-ethylhexyl phosphonic acid mono-2-ethylhexyl ester) in kerosene extract Hf from a sulphate medium [46]. The authors found that at low acid concentrations, a cation exchange reaction is responsible for extraction and set out to solve the stoichiometric constants for the reaction given by R 2-1:



Where $(HA)_2$ represents the dimeric form of D2EHPA. From Eq. 2-3, the reaction equilibrium constant can be described as:

$$K_{eq} = \frac{[Hf(SO_4)_{3-n}]A_g(m - 0.5g)(HA)_{2\ org}][H^+]^g}{[Hf(SO_4)_{3-n}]_{aq}^{g+}[(HA)_{2\ org}]^m} \quad 2-3$$

The partition coefficient of a solute is defined as the ratio of the concentration of the solute in the organic to the aqueous phase. Based on R 2-1 the partition coefficient of Hf is:

$$P_{Hf} = \frac{[Hf(SO_4)_{3-n}]A_g(m - 0.5g)(HA)_{2\ org}}{[Hf(SO_4)_{3-n}]_{aq}^{g+}} \quad 2-4$$

From this the partition coefficient can be written as a function of the equilibrium conditions.

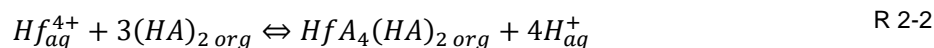
$$\text{Log } P_{Hf} = \text{Log } K_{ex}^{Hf} + m[(HA)_2] - g\text{Log}[H^+] \quad 2-5$$

Wang & Lee solved Eq. 2-5 by varying the metal, acid and carrier concentrations, constructing Log (P) vs. Log (Variable) plots, and determining the slope of the line.

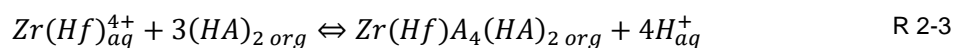
For their experiments, the authors used $HfOCl_2 \cdot 8H_2O$ as a Hf source, and prepared fresh solutions, as they assumed that the small radius and high charge makes Hf prone to hydrolysis and polymerisation, which could affect the extraction over time. The variables they investigated were: i) the Hf aqueous concentration, which ranged from 0.1 to 2 g.L⁻¹ (5.6×10^{-4} – 1.1×10^{-3} M), ii) the H₂SO₄ concentration, which ranged between 1 and 7 M, and iii) the carrier (D2EHPA or PC 88A) concentrations, which ranged between 0.02 – 0.03 M.

By varying the Hf concentration, the authors determined that under their experimental conditions, the organometallic complex of Hf is a mononuclear species. They further reported that the extraction of Hf decreased when varying the H₂SO₄ concentration between 1 and 6 M, while showing an increase at 7 M. The partition coefficient of Hf decreased from around 250 at 1 M H₂SO₄ to 6.3 at 6 M H₂SO₄. Using Log (P) vs. Log (variable) plots, the authors determined that 4 moles of protons are involved in the extraction of 1 mole of Hf, and by varying the D2EHPA concentration, the authors were able to obtain a slope of 3 for the carrier stoichiometry. The

overall extraction reaction for Hf by D2EHPA in H₂SO₄, as reported by Wang & Lee (2016), can be given as:



The authors assumed that, due to the significant chemical similarity between Zr and Hf, that the extraction of Zr by D2EHPA from a sulphate medium would be similar, therefore the extraction reaction of Zr and Hf from a mixed aqueous solution could be written as [46]:



Banda *et al.* (2013) also investigated the selective extraction of Hf from a sulphate medium using D2EHPA. They investigated the effect of the acid concentration from 0.5 to 4 M by extracting 0.2 g.L⁻¹ Zr (from ZrOCl₂·8H₂O) and 0.2 g.L⁻¹ of Hf (from HfOCl₂·8H₂O) using 0.03 M D2EHPA. The stoichiometric carrier to metal (extractant-to-metal, E:M) ratio of the experiments was approximately 9:1. The authors reported that above 1M H₂SO₄ the extraction of both metals decreased. In a second set of experiments at 1 M H₂SO₄, the carrier concentration was varied, which showed that the extraction of both Zr and Hf was nearly complete above an E:M ratio of 9:1. The best separation factor reported at 1 M H₂SO₄ and 0.03 M D2EHPA (E:M of 3:1) was 10.6 [13].

Lee & Min (2015) investigated the separation of Hf from Zr from a sulphate medium with D2EHPA at different Zr:Hf concentration ratios and acid concentrations. The authors used pure ZrOCl₂ and HfOCl₂ salts as metal sources. They fixed the Hf concentration at 0.2 g.L⁻¹ (1.1 x10⁻³ M) and varied the Zr concentration from 0.2 (2.2 x10⁻³ M) to 20 g.L⁻¹ (0.22 M). The H₂SO₄ concentration was varied from 2 – 6 M and the D2EHPA concentration was varied between 0.01 and 0.07 M. The authors reported that the extraction of both metals decreased with increasing acid and metal concentrations, regardless of the Zr:Hf ratio, but even at 100:1 the selectivity toward Hf remained. At a Zr:Hf ratio of 50:1, the best separation factor of approximately 12 was achieved with 2 M H₂SO₄ and 0.05 M D2EHPA (the E:M ratio was approximately 0.45:1) [16].

Wang & Lee (2016) investigated the effect of mixing TBP with D2EHPA or Cyanex 302 on the extraction of Zr and Hf from a sulphate medium. The authors used pure Zr(SO₄)₂·4H₂O and Hf(SO₄)₂·4H₂O as metal sources, with an initial 0.2 g.L⁻¹ concentration of both metals in the aqueous phase while the H₂SO₄ concentration was fixed at 0.5 M. The D2EHPA concentration was 0.01 M (E:M of 3:1), while the TBP concentration was varied from 0.01 to 0.2 M (E:M of 3–60:1). The addition of TBP to Cyanex 302 decreased the extraction of both metals with increasing TBP concentration while having minimal impact on the selectivity toward Hf. The addition of TBP to D2EHPA gave similar results to the Cyanex 302 for TBP concentrations above 0.01 M, while the best separation factor of 6.6 was achieved with no TBP added to the D2EHPA, i.e. the addition of TBP to either Cyanex 302 or D2EHPA had no benefit [39].

Wang & Lee (2016) proposed a complete SX process utilising the D2EHPA-H₂SO₄ system [23]. The authors used pure Zr(SO₄)₂·4H₂O and Hf(SO₄)₂·4H₂O as metal sources. When investigating the effect of the H₂SO₄ (0.1 to 1.0 M) and D2EHPA (0.001 to 0.15 M, E:M of 0.009 to 1.35:1) concentrations, they found that increasing the H₂SO₄ concentration from 0.1 to 0.5 M improved the extraction of both metals before decreasing above 0.5 M H₂SO₄. The extraction of both metals increased with increasing D2EHPA concentration over the entire range tested. The best separation factor (8.8) was achieved with 1.0 M H₂SO₄ and 0.07 M D2EHPA (E:M 0.63:1) [23]. The authors reported agreement with the reaction stoichiometry given by R 2-2. The loaded organic was scrubbed with H₂SO₄ solutions (3.0 to 5.5 M) with the highest separation factor (10.1) achieved at 4 M H₂SO₄. All the Hf remaining in the organic phase could be stripped after a single contact using 1.0 M oxalic acid.

Based on the results acquired the authors attained loading isotherms for a system consisting of 10 g.L⁻¹ Zr (0.11 M), 0.2 g.L⁻¹ Hf (1.1 x10⁻³ M), 0.5 M H₂SO₄, and 0.05 M D2EHPA in kerosene. Using the McCabe-Thiele method, they estimated that 5 cross-current extraction stages would be required to remove most of the Hf, if an O:A ratio of 2 was used. The scrubbing isotherm was obtained with a loaded organic phase containing 0.9 g.L⁻¹ Zr (0.001 M), and 5.7 x10⁻² g.L⁻¹ Hf (3.2 x10⁻⁴ M). Again, using the McCabe-Thiele method, the authors estimated that 4 scrubbing stages would be required to remove all the Zr from the loaded organic phase.

The process conditions and mass balance proposed by Wang & Lee (2016) is shown in Table 2-2. It should be noted that the process proposed is incapable of producing a nuclear-grade Zr stream as the Hf content should be less than 100 ppm. The recovery of near-nuclear-grade Zr was only approximately 25%, while the recovery of pure Hf was approximately 34%.

An important change made in this study was to increase the initial metal concentration in the aqueous phase to 16 g.L⁻¹ (0.18 M) Zr and 0.36 g.L⁻¹ (0.02 M) Hf. The increased concentration better reflects possible industrial concentrations while the Zr:Hf ratio was the same as typically expected in naturally occurring zircon.

Table 2-2: A summary of the SX process proposed by Wang & Lee (2016) [23].

Parameter	Unit	Extraction	Scrubbing	Stripping
Number of stages	-	4	5	1
Inlet [Zr]	g.L ⁻¹	10	3.6	0
Inlet [Hf]	g.L ⁻¹	0.2	0.1	6.8 x10 ⁻²
Aq outlet [Zr]	g.L ⁻¹	2.5	1.8	0
Aq outlet [Hf]	g.L ⁻¹	8.0 x10 ⁻⁴	1.6 x10 ⁻²	6.8 x10 ⁻²
Hf content of outlet stream	ppm	320	8 810	pure Hf
[H ₂ SO ₄]	M	0.5	4	-
[D2EHPA]	M	0.05	-	-
O:A ratio	-	2	2	1
Oxalic acid	M	-	-	1

2.3.1 Disadvantages of SX

Despite the advantages of the technical ease and energy efficient operation, dispersion-based SX processes, do exhibit a number of drawbacks which detract from their current attractiveness for industrial applications.

- The phase dispersion can be difficult to achieve and result in the formation of stable emulsions, which inhibit phase separation and reduce product recovery [17–19,21,33].
- The poor phase separation could lead to entrainment of the organic phase in the aqueous stream, which could in turn affect downstream processes [21].
- The viable phase ratios are limited, as very high or low phase ratios in columns and mixer settlers have a tendency to flood or unload, respectively, resulting in reduced process efficiencies [17,19,33].
- Fluids of similar densities cannot be used effectively, as they tend to be difficult to separate [18,33].
- SX processes do not scale linearly and are not straightforward processes to scale up [17,19].
- The maintenance of moving equipment can be significant [18].
- Certain chemical species, such as the organic solvents used in the MIBK process, are an environmental concern and could lead to significant pollution and dangerous working environments [6].
- It is difficult to estimate the interfacial area of dispersive contactors, especially mixer-settlers, as the droplet size distributions are determined by the operating conditions and fluid properties [17].

- The modelling of the mass transfer in an SX process is difficult due to the uncertainty related to estimating the interfacial area.

The drawbacks related to the dispersion of phases have been significant enough to prompt researchers to investigate ways in which the dispersion can be avoided without sacrificing the mass transfer rates [4,18,35,47–50]. One such avenue of investigation has been the addition of physical supports for one of the phases, which prevents a dispersion while allowing mass transfer to occur [20,33].

2.4 Membrane-based solvent extraction (MBSX)

2.4.1 Introduction

Both MBSX (Figure 2-2) and membrane-based solvent stripping (MBSS) rely on a microporous membrane to immobilise one of the phases in the pores of the membrane through capillary action, and create a L-L interface at the mouth of the pores. Since the membrane prevents the dispersion of one phase into another, these processes are also referred to as non-dispersive solvent extraction [21,31,32,51]. MBSX, through hollow fibre membranes, is a relatively new approach to the more traditional dispersive SX, overcoming many of the disadvantages, while offering not only more interfacial area for mass transfer, but also constant interfacial area regardless of hydrodynamic conditions [17,32,35]. Figure 2-2 illustrates a hydrophobic hollow fibre (HF) membrane impregnated with an organic phase flowing through the inside of the fibre (lumen), an aqueous phase outside the fibre (shell) and the L-L interface situated on the outside surface of the membrane fibre. HF membranes are typically constructed as porous cylindrical membranes which, depending on the hydrophilic or hydrophobic nature, are wetted by one phase which fills the membrane pores via capillary action and through surface tension and a small trans membrane pressure differential (higher on the non-wetting side) providing a stable interface at the mouth of the pore between the wetting and non-wetting phases. This stable interface, in combination with the difference in polarity between the two phases, prevents the bulk of the phases from mixing, while not affecting the extraction or stripping reactions.

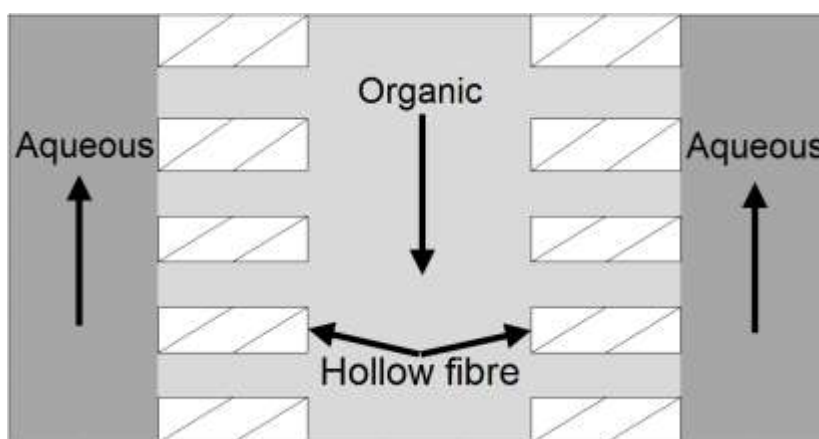


Figure 2-2: Membrane based solvent extraction through a hollow fibre membrane. Redrawn from [52].

It must be noted that some liquid membrane processes, such as MBSX, are often not regarded as true membrane processes, as the membranes merely act as a physical support for one of the phases while having no active role in the process or affecting the separation of the components [17,20,21,31,32,53]. This is because the membranes that are often used for MBSX were originally developed for the purposes of micro- and ultrafiltration, and aside from being hydrophobic or hydrophilic, they do not have any chemical reactions with the typical chemical species used in SX [20,21]. In fact, the chemistry of the extractions in MBSX is the same as with conventional SX, but the separation is achieved through a combination of reaction kinetics and diffusion rather than equilibrium conditions, implying that the separation is determined by the rate of mass transfer [14,21,33]. A number of mass transfer methods related to immobilised L-L interfaces are discussed in greater detail by Schlosser & Marták (2009) [21] and Schlosser *et al.* (2005) [52].

Since MBSX with HF was used in the present study, the following discussion of the working of MBSX is based on the configuration employed for the experimental work. According to Schlosser & Marták (2009), this configuration can be classified as a bulk liquid membrane (BLM) [21]. Convective transport carries the solute in the shell phase through the contactor, while diffusive transport, driven by a concentration gradient between the bulk shell and membrane interface, drives the mass transfer through the shell side boundary layer toward the aqueous-organic interface at the mouth of a membrane pore [33]. At the interface, the solute reacts with a carrier to form an organometallic complex, which then diffuses through the microporous wall towards the lumen-side mouth of the pore [14]. From the mouth of the pore, the complex diffuses through the lumen boundary layer, where convective transport removes it from the contactor [33].

According to Schlosser & Marták (2009), multiple mechanisms could be responsible for the transfer of solutes through the L-L interface [21]. The mechanism can be based on the rate of chemical or biochemical reactions on the L-L interface, different solubilities of components in the organic phase, or the solubilisation of species into the organic phase. The solubilisation of

species occurs by complexing the desired component with a carrier to form a compound that is soluble in the organic phase [21]. It is important to note that, unlike many membrane processes, a pressure differential does not drive the mass transfer, and a transmembrane pressure differential is only required to ensure that the wetting phase remains immobilised inside the pores [17]. The leaking and entrainment of the wetting phase into the non-wetting phase is often called breakthrough, which can usually be prevented by having the non-wetting phase at a slightly higher pressure than the wetting phase [17].

2.4.2 Hollow fibre membrane modules

HF membrane modules are the most widely used and the only ones readily available for industrial MBSX and MBSS applications, with modules ranging in membrane surface area sizes from 1.4 m² (module OD of 6.3 cm) to 130 m² (module OD of 25 cm) [17,21,35]. The most important advantages of HF modules are the relatively simple construction and the geometry which facilitates high L-L interfacial areas in a relatively small form factor [18]. The most commonly used industrial-scale HF contactors are circular, cross-flow modules, such as the Liqui-Cel EXF modules, illustrated in Figure 2-3. HF modules are typically operated either in a parallel-flow or a cross-flow configuration, depending on the relative flow direction of the fluids [18,19].

The first HF modules were constructed as unbaffled shells with the flexible fibres running longitudinally through the shell, with the shell and lumen phases flowing parallel to each other [18,19]. However, these modules suffered from significant shell-side channelling and non-uniform fibre distribution, resulting in decreased mass transfer rates [18]. The baffled cross-flow design (Figure 2-3) provided a significant improvement over previous configurations, as these modules were designed to maximise the flow of the shell-side phase across the fibres by means of a woven membrane mat and a central baffle.

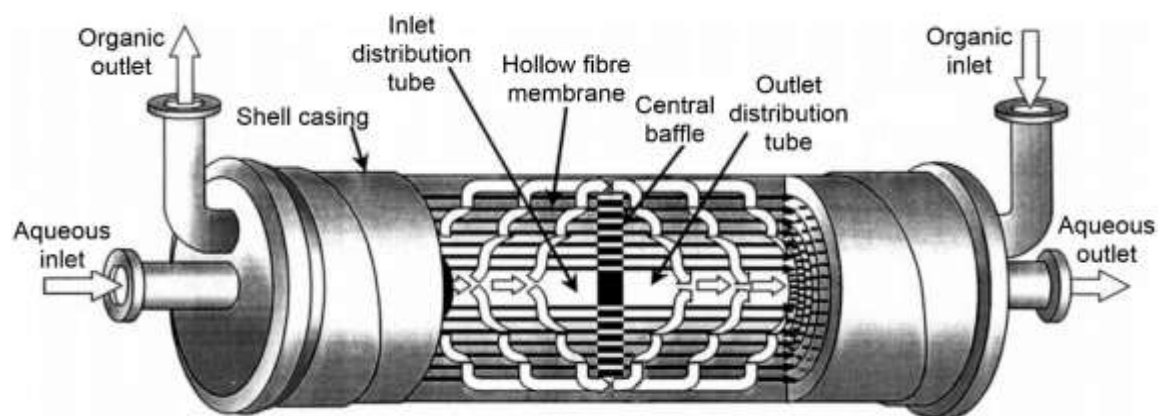


Figure 2-3: Liqui-Cel Extra-Flow module diagram featuring cross-flow design. Adapted from [17].

The non-uniform spacing between the fibres were largely overcome using a woven membrane mat which allows more uniform fibre spacing and hence improved mass transfer, while the distribution tube addressed the problem of shell-side channelling by promoting a shell-side flow

pattern across the membrane fibres, rather than alongside them [17]. The shell-side fluid path, illustrated by means of the white arrows in Figure 2-3, has been described by Baudot *et al.* (2001) [18]: The shell-side liquid is fed through a central inlet distribution tube which is blocked off at the centre of the module. The blockage forces the fluid to exit the tube through holes along the wall, which then flows radially outward across the membrane fibres. Upon reaching the outer wall of the module, the fluid is redirected along the wall toward the second half of the module where it must flow radially inward, again across the fibres, before entering the outlet portion of the central distribution tube [18]. Results reported by Jansen *et al.* (1994) (as reported by Dindore & Versteeg (2005)), on the reactive absorption of SO₂, showed that the cross-flow design could achieve a mass transfer coefficient around one order of magnitude larger than the parallel flow design. [19].

The performance of membrane modules is determined by the overall mass transfer coefficients that can be achieved during operation. Inside the module many possible fluid flow paths exist between the inlet and outlet of the module, and the overall mass transfer coefficient of a given module can be considered as the sum of the local mass transfer coefficients of each of these possible flow paths. These local mass transfer coefficients are strongly influenced by two factors. Firstly, the unique characteristics of any one flow path will differ from that of others due to the unique effects of channelling and fibre distribution, resulting in some paths having less resistance to flow (therefore a larger volumetric flow rate to membrane surface area ratio), as well as being shorter or longer than others. While channelling and path distance does not affect the local mass transfer coefficient directly, the effect of a reduction in the effective surface area (mainly due to channelling) is often mathematically lumped into the overall mass transfer coefficient of a module [19].

Secondly, they are influenced by the velocity and turbulence on the local mass transfer coefficient of any specific flow path [17,19]. Higher velocities and increased turbulence are generally associated with an increased local mass transfer coefficient and, maximising the local turbulence of a flow path improves phase mixing, therefore minimizing the concentration boundary layer thickness around the membrane fibres. These two performance aspects are both addressed by the cross-flow pattern used in later designs, which tends to be less impacted by channelling, and promotes the break-up and remixing of different flow paths, improving the local turbulence, and therefore, the local mass transfer coefficient [17,19]. These improvements make the cross-flow design the preferred choice for MBSS and MBSX processes, even though modelling the process behaviour is more complex, as the solute concentration differs in both radial and axial directions [19].

The construction, operation, and modelling of HF membrane modules are comparable to shell and tube heat exchangers [19]. Dindore & Versteeg (2005) [19] and Fadaei *et al.* (2011) [33] state that the mass transfer along an HF module can likely be described in a similar manner to

the heat transfer along a shell and tube heat exchanger, as the change in the driving force (concentration or temperature) along the length of the exchangers is similar. Although Dindore & Versteeg (2005) also noted that, under circumstances where the mass transfer is affected by a chemical reaction, the application of the heat transfer analogy would have to be adapted to include the effect of reaction kinetics [19].

2.4.3 Advantages and drawbacks of MBSX

MBSX was developed to address many of the drawbacks associated with SX, while also offering a number of significant advantages, such as:

- The nondispersive nature of the process eliminates the formation of emulsions and subsequent loss of the organic phase due to entrainment [14,17,21,31,35,50,53].
- Fluids with identical densities can be used with the contactors in either vertical or horizontal orientation, as the phases are always separate, while flooding and unloading will not occur [14,17,31,53].
- The possible phase ratios that can be achieved are nearly limitless, as each phase can be operated as an individual loop [14,17,21,31,35,53].
- The hydrodynamic conditions on either side of the membrane can be independently controlled [17,31,53].
- Many membrane processes can be scaled up linearly simply by adding more modules either in series or parallel configurations, while the lack of moving parts within contactors make adjusting the number of modules relatively simple [17]. This modular design capability ensures that the production capacity of a plant can be varied significantly simply by adjusting the number of membrane modules used [17].
- Combining MBSX and MBSS into a single process (also known as pertraction (PX)) allows for the intermediate removal of reaction products that may be limited by small equilibrium conversions, thereby increasing the overall conversion of the process [17]. PX through supported liquid membranes (SLM), is one such example where simultaneous extraction and stripping can reduce equilibrium limitations, while the organic phase inventory of an SLM is also significantly less than traditional direct-contact approaches or even most BLM equipment [14,17].

It can be argued that the greatest advantage of MBSX over conventional dispersion SX is the high and fixed L-L interfacial area through which mass transfer occurs [14,18,31,35,50,53]. Kiani *et al.* (1984) reported the specific surface area (surface area to volume ratio) of conventional SX equipment such as rotating columns to be around $200 \text{ m}^2.\text{m}^{-3}$, while the Liqui-Cell EXF modules used by Baudot *et al.* (2001) in their study exhibited a specific surface area of approximately $3000 \text{ m}^2.\text{m}^{-3}$ based on the fibre OD [18]. According to Gabelman & Hwang (1999), the specific surface areas of free dispersion columns, packed/trayed towers, mechanically agitated towers, and

membrane contactors were estimated by Reed *et al.* (1995) as 1 - 10, 10 - 100, 50 - 150, and 500 - 2000 m².m⁻³ respectively [17]. The high surface area potentially results in significantly higher rates of mass transfer compared to traditional dispersive contactors, although according to Gabelman & Hwang (1999) the increased rate of mass transfer is likely due to the increased interfacial area, which remains constant under a range of operating conditions, rather than due to greater mass transfer coefficients [17,19]. Regardless of the exact cause, increased rates of mass transfer could lead to smaller process plants capable of handling the same production specifications of larger dispersion-based SX plants. Such smaller plants correlate to lower capital and operating costs, decreased chemical inventories, and potentially decreased energy consumption [54]. The known and unchanging surface area of the membranes is also beneficial when predicting the performance of an MBSX process under different conditions, as the modelling is significantly simplified [17].

For all the advantages offered by MBSX, the process is not without its drawbacks. Some are inherent to the process, while others are related to the design of the modules.

- A drawback inherent to MBSX include the additional mass transfer resistance encountered due to the membranes through which the solute has to diffuse. The transfer of the solute between phases occurs only by diffusion, and additional resistances can severely impact the viability of the process [21,53].
- The fouling of HF membranes typically does not occur by means of the accumulation of particulates on the surface of the membrane as the contactors do not work by means of convective transport. However, the relatively small openings of the lumen side inlet of the membrane fibres are considerably more likely to be plugged by particulates making prefiltration of the lumen-side phase advisable [22]. Additionally, the aggressive species of the aqueous and organic phases that are common in SX processes could result in the destructive fouling of the membrane leading to the loss of the membrane's hydrophobicity or hydrophilicity as well as eventually the complete failure of the membrane [22].

Drawbacks related to the module design are determined by the construction of the membrane modules and differ based on the module.

- Many HF modules, especially the earlier, parallel flow designs, are and were plagued by a non-uniform distribution of the membrane fibres inside the shell, which resulted in channelling of the shell-side fluid around fibre bundles, reducing the efficiency and the overall rate of mass transfer [17]. This is especially true for low volumetric flow rates, which are susceptible to shell-side channelling and a loss of performance [18,53].
- Elongation of the membrane fibres has been reported by Schlosser & Marták (2009) as a possible cause for the non-uniform distribution of fibres [21]. Elongation also affects the total surface area available for mass transfer and could skew modelling efforts.

- As both shell and lumen phases are pumped and often flow counter-currently to each other, it is vital that the pressure difference is well managed to prevent not only breakthrough but also damage to the membranes and the module shells. The number of modules in series may be limited by the allowable pressure drop on one side of the membrane [17]. High viscosity organic phases pose a particular problem, especially if pumped through fibres with a small internal diameter.
- The construction materials of the modules need to be compatible with the various chemical solutions; of particular importance is that the potting material of the membranes should be compatible with the organic phase, in order to prevent chemical reactions between the seal separating the shell and the lumen [17,53]. The preferred method of operating systems sensitive to leakage is to circulate the lower pressure fluid on the inside of the fibre lumen [17].
- The availability of industrial membrane modules is limited to a few suppliers with limited options available [21]. This has limited the interest in industrial applications, and as a result of low demand, the cost of modules remain prohibitively high [52]. Alternatively, modules designed for filtration need to be repurposed, which could complicate the process due to a number of incompatibilities, as the modules were likely not designed to handle the fluids commonly used in SX. Ideally, the membrane properties and construction materials should be tailored according to the individual system and built for purpose [21].

2.4.4 Applications of MBSX

The majority of applications using MBSX are in the form of pertraction, as the benefit of a single membrane contactor for MBSE and MBSS is often maximised compared to using two separate contactors. Therefore, the majority of literature focusses on PX and not only MBSX.

Valenzuela *et al.* (1998) investigated the application of SLM PX to the recovery of copper (Cu) from the reject water of an SX plant. The shell solution contained 1.0 g.L⁻¹ Cu, which is considered too low for standard SX processes. The authors reported that the Cu content of the shell could be reduced from 1.0 to around 0.2 g.L⁻¹ using an 8 - 10 vol% LIX-860 in Kermac 500-T as the membrane and a 2.0 to 4.3 M H₂SO₄ stripping solution [55].

Gawroński & Wrzesińska (2000) [31], and Kertész & Schlosser (2005) [32] found that MBSX and PX have significant potentials for application over a diverse range of fields, including the separation of organic compounds, waste water treatment, *in situ* removal and concentration of pharmaceutical and fermentation products, and recovery of metals. For a review on hollow fibre membrane contactors and potential applications, many of which being non-MBSX, readers are referred to Gabelman & Hwang (1999) [17]. For the sake of simplicity, this section will use the term 'pertraction', to refer to any configuration of solvent extraction, solvent scrubbing, and or, solvent stripping where membranes are used as a physical support for one of the phases.

Baudot *et al.* (2001) investigated the extraction of aroma (flavour) compounds from an aqueous solution into sunflower oil using MBSX. For this, MBSX is well suited, as both light and heavy compounds can be removed without endangering heat-sensitive compounds. SX has been shown as an effective method for separation, but the phase dispersion can be inconvenient. MBSX avoids phase dispersion, and the lack of a phase change can result in drastically reduced operating costs. The concentration of aroma compounds in the aqueous phase was low (2 - 50 ppm), but the authors still reported promising extraction results alongside high mass transport rates [18].

Trivunac *et al.* (2004) investigated the removal of phenol from wastewater and found that PX is effective for cleaning the wastewater, avoiding many of the disadvantages related to emulsion formation with dispersion SX. Phenol, as well as its derivatives in industrial waste water, can range from a few ppm to 3%. The authors were able to remove up to 75% of the phenol from a 0.1 mol.L⁻¹ aqueous solution over the course of one hour. They illustrated that a low aqueous velocity (1.1 cm.s⁻¹) was required to ensure high extraction efficiency [56].

Hasanoglu (2013) evaluated emulsion PX using simulated wastewater streams with an 800 ppm phenol contamination using Liqui-Cell™ 1.7x5.5 HF Minimodules. The author tested various organic plus stripping solution combinations, including air, pure NaOH, pure 1-decanol, and mixtures of NaOH and 1-decanol. Using an air-filled membrane, they were able to reduce the phenol content in the aqueous phase from 800 to 150 ppm after 150 minutes. Using pure NaOH as the solvent phase, the author was able to reduce the phenol content in the aqueous phase to 150 ppm after 160 minutes, while a pure 1-decanol organic solvent was able to achieve the same phenol concentration after 25 minutes. In addition to the significantly increased rate of mass transfer using a 1-decanol solvent, they reported that the transmembrane water transport was reduced to less than 6% of the aqueous phase volume, compared to 35% for the air-filled membrane. Hasanoglu reported emulsion PX as an advantageous technology, as it is both effective and able to combine extraction and stripping into a single process unit, thereby reducing the equipment costs and solvent consumption [57].

Červeňanský *et al.* (2017) investigated the potential of PX for the *in situ* removal of 2-phenylethanol from a fermentation broth. Their study used an octane-impregnated polypropylene HF to create a SLM. During a 72-hour membrane stability experiment, the authors reported no degradation of the membrane, no fouling by the biomass present, and highly stable extraction kinetics. The authors also reported that the SLM was able to extract the 2-phenylethanol while leaving the L-phenylalanine reagent in the aqueous phase [58].

The hydrometallurgical applications of PX are likely one of the most promising areas as the non-dispersive contact reduces the risk of entrainment of the organic phase and electrolyte contamination, which is known to negatively impact metal deposition during electrowinning [50].

Applications of this include the hydrometallurgical separation of heavy metals such as Zn, Cu, Co, Ni, and Cd from feed liquors as well as waste water streams [33].

Carrera *et al.* (2009) investigated the application of emulsion PX to treat the wastewater effluent from a hot-dip galvanising process. They reported that higher extraction and stripping could be achieved using increased zinc (Zn) concentrations in the aqueous phase and greater emulsion volumes; whereas the carrier to strippant ratio had a negligible effect on the extraction of Zn, while for stripping a low carrier to strippant ratio was optimal [59].

Chaturabul *et al.* (2015) investigated the separation of mercury from petroleum-produced water using hollow fibre supported liquid membrane (HFSLM) PX. Their optimal conditions consisted of an aqueous phase pre-treated with 0.2 M HCl, a 4 vol% Aliquat 336 membrane phase and 0.1 M thiourea stripping solution. From an initial aqueous phase concentration of 2 ppm Hg, the authors were able to reduce the Hg content of the discharge water to approximately 5 ppb [54].

Mans *et al.* (2018) investigated the use of PX to separate cobalt (Co) from spent catalyst solutions. They were able to selectively extract Co from a mixed cobalt-nickel (Co-Ni) aqueous phase solution even at a 1:10 concentration ratio of Co:Ni. They generated a conceptual design for a PX plant capable of extracting $0.85 \text{ kg}\cdot\text{h}^{-1}$ Co from an aqueous solution to reduce the concentration of Co from 4.7 to $0.01 \text{ g}\cdot\text{L}^{-1}$. Based on a constant K_{OV} of $7.43 \times 10^{-8} \text{ m}\cdot\text{s}^{-1}$, they predicted a total surface area of 2125 m^2 would be required necessitating 6 14x40 Liqui-Cel modules combined in series [48].

Schlosser *et al.* (2005) compiled an overview of the applications of MBSX and PX for the recovery and separation of organic acids [52]. Their paper provides many references to available literature, and interested readers are advised to refer to their paper for more applications of MBSX and PX.

2.5 MBSX of Zr and Hf

The application of MBSX to the separation of Zr and Hf has received limited attention in literature. Some of the first literature that was published by Chaudry & Malik in 1989 researched the transport of Zr and Hf through a flat sheet SLM with TBP in a xylene organic phase. They reported a maximum flux for Zr and Hf of 1.29×10^{-6} and $2.0 \times 10^{-6} \text{ mol}\cdot\text{m}^{-2}\cdot\text{s}^{-1}$, respectively. Optimal conditions for attaining a separation ratio of approximately 8 were the following: a TBP concentration above 2.93 M, an HNO_3 concentration of between 5 and 6 M, and a temperature of $10 \text{ }^\circ\text{C}$ [14].

Yang *et al.* (2002) investigated the PX separation of Zr from Hf using HFSLMs with tri-n-octylamine (TNOA) and trioctylmethyl ammonium chloride (Aliquat 336) as carriers [14]. They used polypropylene hollow fibres with an ID of $600 \text{ }\mu\text{m}$, wall thickness of $200 \text{ }\mu\text{m}$, and a porosity of 69%. The variables they investigated included the HCl concentration of the feed and strip solutions, the feed flow rate, and the fibre length. The PX experiments were conducted by

circulating the feed inside the membrane lumen and the stripping solution in the shell for 20 hours. The organic phase contained either 0.5 M TNOA or 0.2 M Aliquat 336 with 1.0 M 2-ethyl-1-hexanol as modifier and kerosene as diluent. The stripping phase consisted of 2 M HCl. They reported that, after 1 hour, the extraction of Zr and Hf reached around 85% and 15% respectively, reaching a plateau due to the decreased concentrations in the feed. Increasing the HCl concentration in the feed solution resulted in higher mass flux values for both Zr and Hf, but a reduced separation factor. A higher HCl concentration in the strip phase decreased the flux and separation factor of both metals. The feed rate was varied between 0.8 and 8.8 mL.min⁻¹ (the superficial velocities varied between approximately 0.007 and 0.073 cm.s⁻¹ in the shell and 0.14 to 1.48 cm.s⁻¹ in the lumen, respectively). The mass transfer coefficient increased from 4.1 x10⁻⁴ m.s⁻¹ at 0.8 mL.min⁻¹ to a 6.0 x10⁻⁴ m.s⁻¹ at 8.8 mL.min⁻¹. Over the same variation in the flow rate, the mass transfer coefficient of Hf increased from 0.4 x10⁻⁴ to 0.8 x10⁻⁴ m.s⁻¹. The separation ratio, favouring Zr, increased from approximately 5.1 at 0.8 mL.min⁻¹ to 7.5 at 4.4 mL.min⁻¹. The authors further reported that the membrane resistance was likely to control the rate of mass transfer at flow rates above 4 mL.min⁻¹. An increase of the fibre length from 100 to 300 mm did not show a significant impact on the separation ratio.[14].

Despite an extensive search for literature, at the time of writing, the author was unable to find other studies that specifically investigated the application of MBSX or PX for a Hf-selective separation process.

2.6 Modelling MBSX mass transfer

A detailed analysis of the mass transfer occurring inside a membrane contactor is required for the purposes of process design [31]. The mass transfer of a solute in an MBSX contactor can be seen as a combination of convection, diffusion, and reaction kinetics [54]. Modelling of the mass transfer in an MBSX system is typically done in one of two ways.

The first method involves solving conservation equations for continuity, energy, and momentum, which need to be solved simultaneously using computational fluid dynamics (CFD) [33]. This approach is complex, requiring a thorough understanding of the use of CFD. Fadaei *et al.* (2011) investigated the extraction of metal ions through a membrane contactor [33]. Their simulations used CFD to solve equations for the mass and momentum transfer of Cu²⁺ from an aqueous solution into a D2EHPA-kerosene organic phase under laminar conditions. This approach has the potential of providing highly accurate predictions of the behaviour inside membrane contactors, at the cost of more complex models, longer computational time, and the prerequisite CFD skills.

The second method, known as the resistance-in-series (R-i-S) approach, is based on the film model, and assumes that the rate of mass transfer from the aqueous phase to the organic phase consists of three diffusion steps: firstly, the aqueous boundary layer, secondly, the membrane

pores, and lastly, the organic boundary layer, as expressed in Eq. 2-10 [18,20,31,32,53,60,61]. This model is very similar to what would be encountered in heat transfer where the energy is transferred through multiple layers of material [62]. This approach is generally simpler and requires less data than the CFD-based approach, and is therefore more widely used for this type of application [20,33]. The drawback of such an approach is that, the simplicity sacrifices some of the accuracy (as compared to CF-based models), and without accurate estimations of each parameter, it is difficult to optimise a process effectively, as the transfer rate is often determined by one or more limiting steps [63]. The mass transfer model using the R-i-S method consists of two master equations; the first is a mass balance based on a continuity equation for the solute moving through a control volume in the membrane contactor, while the second equation describes the mass flux through the membrane.

2.6.1 Mass balance

By applying the law of conservation of mass over the control volume depicted in Figure 2-4 the mass balance over the aqueous phase can be described by Eq. 2-6, when using the assumptions listed below:

- Steady state with no solute accumulation in the membrane [17,19,33,53,54].
- The system is isothermal [19,33,54] with constant fluid properties.
- The mass transfer coefficient of any solute remains constant [19].
- Both fluids are completely immiscible with no convective transport through the membrane [17,53].

$$\dot{Q}_S C_S|_y - \dot{Q}_S C_S|_{y+\Delta y} = j_x A_{Mem} \quad 2-6$$

Converting Eq. 2-6 to a differential form, the concentration profile can be written as:

$$\frac{dC_S}{dA_{Mem}} = \frac{j_x}{\dot{Q}_S} \quad 2-7$$

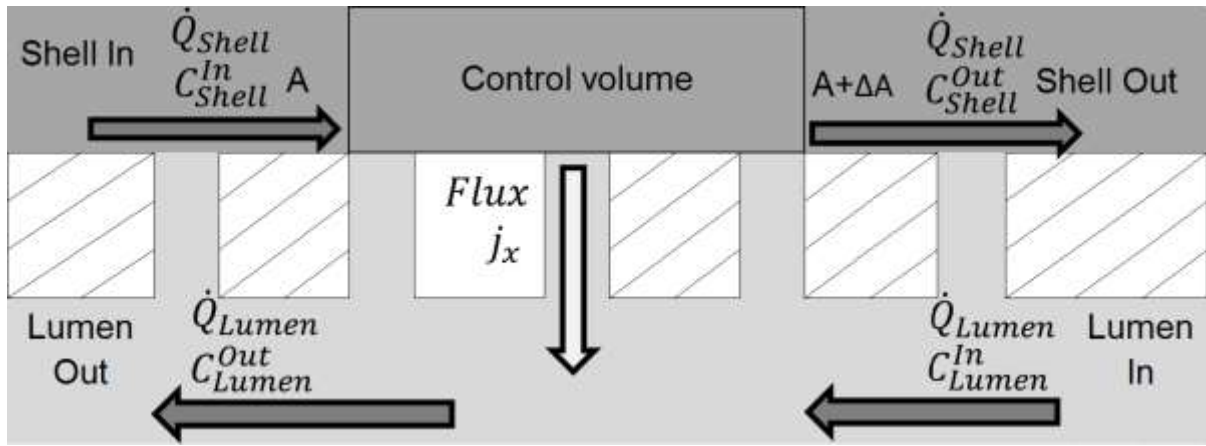


Figure 2-4: The differential control volume created over aqueous phase (shell-side) for the mass balance.

Eq. 2-7 can be integrated over the surface of a membrane contactor to estimate the total surface area of said membrane column that would be required to achieve a certain design specification. However, before Eq. 2-7 has any use, the mass flux, j_x , needs to be estimated.

2.6.2 Mass flux

The mass flux, illustrated in Figure 2-5, can typically be estimated using Fick's law of diffusion:

$$j_{Shell} = j_{Membrane} = j_{Lumen} = j_x \quad 2-8$$

$$k_S(C_S^{Bulk} - C_S^{Int}) = k_{Mem}(C_S^{Int} - C_L^{Int}) = k_L(C_L^{Int} - C_L^{Bulk}) = K_{OV} \left(C_S - \frac{C_L}{P} \right) \quad 2-9$$

With k_{OV} , the overall mass transfer coefficient, being:

$$R_{Total} = R_{Shell} + R_{Membrane} + R_{Lumen} = \frac{1}{K_{OV}} \quad 2-10$$

Using the mass flux equation, we assume:

- The mass flux of each stage step is identical [53].
- The mass transfer is well described by the boundary layer model [17,53].
- The concentration distribution is uniform in the shell and lumen [54].
- The membrane is fully filled with the organic phase [33].
- The curvature of the interface does not significantly affect the mass transfer, partition coefficient or surface area of the membrane[17,53].
- The extraction reaction occurs only on the L-L interface in the pores of the membrane [53,54].
- The reaction kinetics are fast, irreversible, at equilibrium on the interface, and do not limit the rate of mass transfer [17,19,33,35,50,53,54].
- The solute can only enter the organic phase as the converted complex. [54].

- The concentration at the membrane-organic phase interface is continuous [33].
- Both phases exhibit laminar flow conditions and are ideally mixed [17,33,53].
- The membrane properties are constant along the entire length of the column [17,53].
- No boundary layer interference occurs between the membrane fibres [64].
- The partition coefficients and mass transfer coefficients are constant along the length of the membrane [17,19,53].

The available literature remains somewhat divided on a common manner in which K_{OV} should be written as a function of the individual mass transfer coefficients. Some authors utilise the surface area (m^2) based on the inner (ID), outer (OD) or log mean (LM) diameter [18,20,35] of the fibres, while others simply use the relevant diameter rather than the surface area [17,50,53,64]. Some authors include the membrane porosity [20,35], while others use the total surface area based on either the inner or outer fibre diameter [18]. Three common variations of equations used to calculate K_{OV} are listed in Table 2-3. The expressions have been rewritten to use the same notation, and to be applicable to a system consisting of a hydrophobic membrane with the aqueous phase flowing through the shell and the organic phase through the lumen. The problem created by the lack of consensus is that it causes confusion and makes it difficult to compare published work. Therefore, care should be taken whenever comparing published data and mass transfer coefficient correlations to experimental work. In the present study Eq. 2-11 as given by Gabelman & Hwang (1999) was used [17].

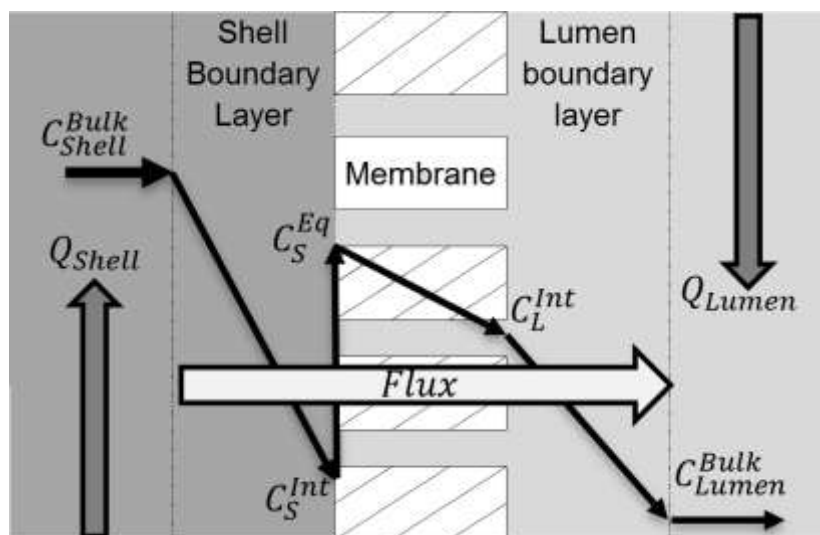


Figure 2-5: The resistance-in-series mass transfer model. Redrawn from [35].

It is worth noting that the extraction reaction of metals is often regarded to be fast compared to the diffusion and is assumed to achieve equilibrium at the aqueous–organic interface, thus having no significant impact on the overall resistance [33,49,65]. Therefore, most authors do not include a term describing the resistance added by the reaction kinetics to Eq. 2-10.

However, Schlosser *et al.* (2001) reported that in the case of the PX of butyric acid, the stripping reaction kinetics represent approximately 38% of the total resistance to mass transfer, indicating that care should be taken when neglecting the effect of reaction kinetics [20]. Under conditions of a large partition coefficient and high stoichiometric excess of reagents, especially that of the carrier, it is possible to minimise the resistance of the reaction kinetics. However, in the event of two or more species being extracted simultaneously, the modelling becomes more complex, and resistance related to the reaction kinetics would likely play a significant role, especially if the solutes compete for the carrier in the organic phase [32].

In order to solve for K_{OV} in any of the equations listed in Table 2-3, the individual coefficients should be estimated.

Table 2-3: Variations in the overall mass transfer coefficient of MBSX in published literature.

Equation	Ref.
$\frac{1}{K_{OV}} = \frac{1}{k_{Shell}} + \frac{d_{OD}}{Pk_{Mem}d_{LM}} + \frac{d_{OD}}{Pk_{Lumen}d_{ID}}$	2-11 [17]
$\frac{1}{K_{OV}} = \frac{A_{OV}}{P_{Shell}k_{Shell}A_{OD}} + \frac{A_{OV}}{P_{Mem}k_{Mem}A_{LM}} + \frac{A_{OV}}{P_{Lumen}k_{Lumen}A_{ID}}$	2-12 [18]
$\frac{1}{K_{OV}} = \frac{\varepsilon}{k_{shell}} + \frac{A_{OD}}{P_{Shell}A_{LM}k_{Mem}} + \frac{A_{OD} \varepsilon}{P_{Shell}A_{ID}k_{Lumen}}$	2-13 [20]

2.6.3 Overall mass transfer coefficient

The overall mass transfer coefficient, Eq. 2-14, can be derived from a mass balance on the aqueous side, such as is given by Eq. 2-6, and K_{OV} solved using experimental data [18,50].

$$K_{OV} = \frac{Q_S \Delta C_S}{A_{Mem} \Delta C_{LM}} \quad 2-14$$

With the logarithmic mean concentration difference between the shell and lumen:

$$\Delta C_{LM} = \frac{C_{in} - C_{out}}{\ln\left(\frac{C_{in}}{C_{out}}\right)} \quad 2-15$$

For systems where the resistances of Eq. 2-10 are in the same order of magnitude, the analysis is more complex, and having correlations to describe the mass transfer coefficients is imperative in the design of an MBSX process [17].

2.6.4 Membrane mass transfer coefficient

The membrane mass transfer coefficient can be described using Eq. 2-16 [14,18,31,50,66].

$$k_{Mem} = \frac{D_{AB}\varepsilon}{\tau\delta} \quad 2-16$$

With D_{AB} being the metal-carrier complex diffusion coefficient, which is commonly estimated using the Wilke-Chang equation given in Eq. 2-17 [18,20,32,35,58,64,67].

$$D_{AB} = 1.173 \times 10^{-13} * \frac{(\phi MW_B)^{0.5} T}{\mu^* v_A^{0.6}} \quad 2-17$$

According to Gabelman & Hwang (1999), Eq. 2-16 is valid for membranes with a porosity in the range of 20 to 90% and a tortuosity between 2 and 3 [17]. Kertész *et al.* (2005) reported that the tortuosity of polypropylene membranes with approximately 30% porosity was between 2 and 3.5 [35].

Gawronski & Wrzesinska (2000) investigated the extraction of ethanol from water into n-octanol. They reported that hydrophilic membranes had mass transfer coefficients around 2 to 4 times higher than those of hydrophobic membranes, which they attributed to the faster rate of ethanol diffusion in water when compared to ethanol in n-octanol. They also investigated the fibre packing factor, and reported that both high and low packing factors resulted in decreased mass transfer coefficients, due to interactions between fibres and non-uniform flow conditions created by the irregular distribution of fibres at high packing densities, whereas low packing densities resulted in channelling [31].

Diffusion coefficients of 2.76×10^{-10} and $2.11 \times 10^{-10} \text{ m}^2 \cdot \text{s}^{-1}$ for phenylalanine-D2EHPA complexes in C_{10} to C_{13} n-alkanes ($\text{Phe}(\text{DEHPA})_4(\text{H}_2\text{O})_2$ and $(\text{Phe})_2(\text{DEHPA})_6(\text{H}_2\text{O})_4$), respectively, were determined by Kertész *et al.* (2005) [35]. Kertész & Schlosser (2005) estimated a diffusion coefficient of the (butyric acid)₃-trioctylamine complex of $3.55 \times 10^{-10} \text{ m}^2 \cdot \text{s}^{-1}$ in n-alkanes [32]. Soldenhoff *et al.* (2005) investigated the extraction of Co using MBSX. They reported diffusion coefficients of 1.24×10^{-10} and $1.35 \times 10^{-10} \text{ m}^2 \cdot \text{s}^{-1}$ for Cobalt-Ionquest 801 in Shellsol D70 and Cobalt-Cyanex 272 in Shellsol 2046 respectively. They estimated the molecular radius of the organometallic complexes from that of the monomeric carrier molecule, using the assumption that the volume of the organometallic complex was four times larger than that of the monomer, as four carrier molecules were required to extract one mole of Co [50].

Based on the diffusion coefficients from published literature, it could be expected that a Zr or Hf-D2EHPA complex would exhibit diffusion coefficients in the order of $1 \times 10^{-10} \text{ m}^2 \cdot \text{s}^{-1}$, or less, as larger complexes may form at increased complex concentrations in the organic phase.

2.6.5 Lumen-side mass transfer coefficient

Estimating the flow inside the membrane lumen is generally the simplest step, as laminar flow inside circular tubes has been studied extensively [60,62]. The mass transfer inside the lumen is largely determined by convective forces and flow patterns, and the mass transfer coefficients for many systems can be predicted using Sherwood relations of the form [17,31]:

$$Sh \propto Re^\alpha Sc^\beta f(\text{geometry}) \quad 2-18$$

The relation provided by Dahuron and Cussler (1988) for laminar flow in tubes ($Re < 2700$ [18]) is used extensively in literature to predict the lumen mass transfer coefficient [19,32,50,53]:

$$Sh_{Lumen} = \frac{k_{Lumen} d_H}{D_{AB}} = 1.5 \left(\frac{d_L^2 U_L}{L D_{AB}} \right)^{0.33} \quad 2-19$$

The L  v  que equation, given by Eq. 2-20, has been used by many authors under a number of different conditions for both liquid and gas phase systems [17–19,50,56,58,61,68].

$$Sh_{Lumen} = \frac{k_{Lumen} d_H}{D_{AB}} = 1.62 \left(\frac{d_L U_L}{L D_{AB}} \right)^{0.33} \quad 2-20$$

Baudot *et al.* (2001) stated that the L  v  que equation is only valid for Graetz ($Gz = \frac{d_H}{L} Re Sc$ for mass transfer) values higher than 4, as low flow rates in combination with variations in the internal diameter of the hollow fibres, could result in non-uniform flow [18]. However, both Bocquet *et al.* (2005) [53] and Wang *et al.* (2017) [63] reported that at low Graetz numbers (below 6) the L  v  que equation could significantly overestimate the Sherwood number of the lumen side, and should ideally be used only when $Gz > 20$. Through analysis of the available literature, Wang *et al.* (2017) stated that at Graetz values around 5 the Sherwood number tended toward a value of 1. They further recommended that, when operating at Graetz values less than 2, Eq. 2-21 should be used instead of Eq. 2-20 [63].

$$Sh_{Lumen} = 0.36 Gz = 0.36 \left(\frac{d_H}{L} \right) (Re Sc) \quad 2-21$$

Since the hydraulic diameter, d_H , of a circular pipe is equal to the inside diameter of the pipe, the lumen side Reynolds number is equal to:

$$Re_{Lumen} = \frac{d_{Lumen} U_{Lumen} \rho}{\mu} \quad 2-22$$

The density and viscosity of both the aqueous and organic phases have to be accounted for when estimating the mass transfer coefficients. Koekemoer *et al.* (2005) investigated the change in the density and viscosity of D2EHPA in kerosene solutions and found that both the density and

viscosity can be adequately described by relatively simple and conventional relations [69]. A good fit of the experimental data was reported for the solution density, which was determined using Eq. 2-23:

$$\rho_{Solution} = \sum_i \varphi_i \rho_i \quad 2-23$$

Where the viscosity of mixtures can be predicted with the Kendall Monroe equation [69]:

$$\eta_{mixture} = \left(\sum_{i=1}^n \omega_i \eta_i^{\frac{1}{3}} \right)^3 \quad 2-24$$

Since Eq. 2-24 requires that the molar fraction of the components in the mixture is known, a unique molecular weight for petroleum fraction products such as Shellsol or kerosene, which do not have a specific molecular weight, should be defined. Under the assumption that an average molecular mass can be estimated, Eq. 2-24 can be rewritten in terms of the volume fraction as described by Eq. 2-25 [70].

$$\omega_i = \frac{\varphi_i \frac{\rho_i}{MW_i}}{\sum_i \varphi_i \frac{\rho_i}{MW_i}} \quad 2-25$$

Further, with the assumption that interactions between the components is similar, Eq. 2-25 can be substituted into Eq. 2-24 and expanded for a three-phase system, as described by Eq. 2-26.

$$\eta_{mixture} = \left(\frac{MW_2 MW_3 \varphi_1 \rho_1 (\eta_1)^{\frac{1}{3}} + MW_1 MW_3 \varphi_2 \rho_2 (\eta_2)^{\frac{1}{3}} + MW_1 MW_2 \varphi_3 \rho_3 (\eta_3)^{\frac{1}{3}}}{M_2 M_3 \varphi_1 \rho_1 + M_1 M_3 \varphi_2 \rho_2 + M_1 M_2 \varphi_3 \rho_3} \right)^3 \quad 2-26$$

2.6.6 Shell-side mass transfer coefficient

Predicting the shell-side mass transfer behaviour of a system has proven to be significantly more difficult than the membrane or lumen, as evidenced by the number of Sherwood correlations reported in literature [17,31]. Due to the often-random packing and varying distances between the membrane fibres, it is difficult to predict the flow and distribution of the fluid inside the shell. Nonetheless, many authors have investigated the shell-side mass transfer in various membrane modules and reported Sherwood correlations for their findings. Table 2-4 lists a number of the correlations that have been reported in literature for conditions similar to the experimental work of this study.

Two important factors include the flow rate and packing factors. It can be seen in the relations listed that the power of the Reynolds number varies between approximately 0.33 and 0.8. Typically, a Reynolds exponent of 0.33 would be expected for laminar flow conditions. The

deviation away from this is probably due to the irregular distribution and flexibility of the fibres in commercial modules, which alongside the variations in the fibre packing density affect the local flow pattern, resulting in more laminar conditions in highly packed sections, and more turbulence in lower packed sections [31]. Furthermore, fibres that are not perfectly straight are also likely to affect the flow pattern and possibly enhance the mixing and local mass transfer coefficient [64]. These factors are likely responsible for the wide range of Reynolds exponents that have been reported.

The model reported by Gawronski and Wrzesinska (2000), Eq.2-29, which was developed for low Re numbers, had an exponent of $(0.8 - 0.16\theta)$, which was always greater than 0.33, suggesting that locally turbulent flow conditions existed on the shell side of their module [31]. The significant variations in published literature has resulted in many authors fitting Sherwood relations to their unique situations [64].

Table 2-4: Shell-side Sherwood relations from literature.

Range	Relation	Eq.	Ref
$0 < Re < 500$	$Sh = 5.85(1 - \theta)\left(\frac{d_H}{L}\right)(Re^{0.6}Sc^{0.33})$	2-27	[17]
Laminar	$Sh = 2 + 1.1\left(\frac{\mu_{Shell}}{\rho_{Shell}D_{AB}}\right)^{0.33}\left(\frac{d_H U_{Shell}}{\mu_{Shell}}\right)^{0.6}$	2-28	[71]
$1 < Re < 10$	$Sh = 0.09(1 - \theta)Re^{(0.8-0.16\theta)}Sc^{0.33}$	2-29	[31]
$Gz < 60$	$Sh = 0.019Gz$	2-30	[17]
$0.16 < Re < 7.3$	$Sh = 8.71\left(\frac{d_H}{L}\right)(Re^{0.74}Sc^{0.33})$	2-31	[31]

The shell-side Reynolds number is slightly more complex compared to that of lumen, partly due to the various definitions used by different authors to determine the shell-side hydraulic diameter. Some authors, such as Schoner *et al.* (1992), used the diameter of the entire fibre bundle, while others used the OD of a single fibre [18,50]. Baudot *et al.* (2001) suggested that the hydraulic diameter of a centre-tubed cross-flow module could be described by Eq. 2-32 [18]:

$$d_H = \frac{d_{Fibre\ bundle}^2 - d_{Distribution\ tube}^2 - N_{Fibres}d_{Fibre\ OD}^2}{N_{Fibres}d_{Fibre\ OD}} \quad 2-32$$

The superficial velocity is conventionally determined as the shell-side volumetric flow rate divided by the empty cross-sectional area of the shell [50]:

$$U_{Shell} = \frac{Q_{Shell}}{A_{C_{Shell}}} \quad 2-33$$

2.7 Process parameters

From the available literature, it can be concluded that the most important parameters when estimating the mass transfer performance of an MBSX process, are: the solute partition coefficients, the carrier concentrations, the aqueous and organic flow rates, the location of the phases, and the fibre packing factor.

Baudot *et al.* (2001) extensively studied the effects of the partition coefficient and aqueous phase velocity on the mass transfer behaviour of aroma compound MBSX [18]. They reported that high and low partition coefficients typically determined the controlling resistance. For species with a high partition coefficient, the resistance of the membrane and organic phase became minimal due to the high solubility of the species in the organic phase. This can be seen in the equations listed in Table 2-3, where a large P value would reduce the membrane and organic phase resistances, making the aqueous resistance dominant. On the other hand, for species with low partition coefficients, the membrane and organic phase resistances were both significant. Their investigation into the effect of flow rates revealed that the mass transfer coefficients of species with a high partition coefficient had a greater response to an increased aqueous flow rate, indicating that the aqueous side resistance was limiting the rate of mass transfer. The overall mass transfer coefficient of species with a partition coefficient of approximately 50 or more were also nearly one order of magnitude larger than species with a partition coefficient below 20 [18].

Gabelman & Hwang (1999) reported that a low aqueous phase and high organic phase flow rate improved the extraction efficiency of an MBSX process, as the long residence time of the aqueous ensured good solute removal, while the high organic phase flow rate maintained the lowest possible organic phase concentration, and therefore, the highest possible driving force. They further stated that several considerations have to be taken into account when deciding which fluid is located where. As the shell-side tends to be subject to bypassing and channelling, it is difficult to attain a high degree of extraction if the aqueous phase is located in the shell [17]. On the other hand, the pressure drop through the shell tends to be lower, which would be advantageous if a high viscosity organic phase was to be used.

Asimakopoulou & Karabelas (2006) argue that because the often-neglected organic phase flow rate does not typically control the rate of mass transfer, the degree of carrier saturation could become a significant concern. As such, they state that carrier saturation is an important parameter, which must be included when assessing the extraction performance [64]. Carrier saturation can be especially problematic for high partition coefficient species that are contacted with organic phases with a low carrier concentration, as equilibrium limitations could severely affect the driving force for mass transfer.

Schlosser *et al.* (2001) investigated the effect of increased carrier concentrations on the extraction of butyric acid with trioctylamine (TOA). A threefold increase in carrier concentration only

increased the flux of butyric acid by 16%. The discrepancy between the expected increase and the experimental data was attributed to a combination of reaction kinetics and the aggregation of extraction complexes at the mouth of a membrane pore, effectively blocking the interface and decreasing the diffusion rate of fresh reagents [20]. A second effect of an increased carrier concentration, is an increase in the viscosity of the organic phase, resulting in lower diffusion coefficients of both the carrier and extraction complexes.

Bocquet et al. (2005) modelled the mass transfer of sulphur aroma compounds from an aqueous solution into hexane at various aqueous phase velocities (0.06 to 0.2 m.s⁻¹). They found that the mass flux increased by 47% while the extraction decreased to approximately 55% of the original value between the minimum and maximum velocities. According to their results, the aqueous phase always provided the predominant resistance (species partitions coefficients ranged between 92 and 565), where increasing the organic phase flow rate from 60 to 3000 mL.min⁻¹ resulted in less than 1% increase in the rate of mass flux [53]. The behaviour was explained by an increase in the quantity of solute moving through the contactor, which facilitated the higher mass transfer coefficient, whereas the increased velocity decreased the residence time of the solute inside the module, resulting in the loss of extraction efficiency. It is however also possible that the increased mass flux at higher velocities could have resulted from a smaller boundary layer, in which case the observed decrease in extraction would have resulted from the increased mass flow rate through the membrane contactor. Even though the mass flux increased at higher velocities, that increase was less than the increase of the total mass flow rate. Therefore, the extraction, represented as a percentage of the total mass flow, appeared to decrease as the fluid velocity increased.

2.8 Conclusion

The separation of Zr and Hf is the most important but also most difficult step in the production of nuclear-grade Zr. SX has been well established as the most common approach to the separation, with the TBP and MIBK processes being used for the majority of Zr and Hf separation. However, recent SX research has found that the D2EHPA-H₂SO₄ system holds potential for industrial application due to the selectivity towards Hf. A significant drawback of traditional SX processes, including the TBP, MIBK, and D2EHPA-H₂SO₄ systems, is the reliance on the dispersion of the aqueous and organic phases, which facilitates mass transfer between the phases.

The inclusion of a membrane to act as a phase separator, while still allowing mass transfer, has been proven as an alternative to the traditional dispersion-based approaches. However, the application of MBSX for the separation of Zr and Hf has not been well investigated, and the currently available literature does not provide sufficient data to allow an industrial-scale estimation of an MBSX process for the separation of Zr and Hf to be made.

3 Materials and methods

3.1 Chemical reagents

The chemicals that were used in this study are listed in Table 3-1, including their function, purity, supplier, and CAS No. The Zr/Hf salt purity was determined experimentally, as described in Section 3.3.2. Appendix A 1 contains the chemical data sheet of Shellsol 2325, provided by Shell Chemicals. All other chemicals were used as supplied by the respective vendors.

Table 3-1: List of chemical reagents used.

Reagent	Function	Purity	Supplier	CAS No.
Zr(Hf)SO ₄ ·4H ₂ O	Metal source	98% ¹	Hangzhou Dayangchem Co. Ltd.	7446-31-3
H ₂ SO ₄	Anion source	98%	Labchem (Pty) Ltd.	7664-93-9
Shellsol 2325	Diluent	-	Chemquest (Pty) Ltd.	64742-81-0
D2EHPA ²	Carrier	98%	Sigma Aldrich	298-07-7
1-Octanol	Phase modifier	95%	Sigma Aldrich	111-87-
Zr and Hf standards	ICP-OES standard	99.99%	De Bruyn Spectroscopic Solutions	Zr 7440-67-7 Hf 7440-58-6

¹ Determined in-house

² Bis-(2-ethylhexyl)phosphoric acid

When designing a separation process, it is often desirable to select a method which facilitates small downstream units. In this case, the Zr:Hf mass ratio was approximately 50:1, therefore a chemical system exhibiting selectivity toward Hf was selected. While a number of Hf-selective organophosphorus-sulphate systems have been reported in literature (see Table 2-1), the D2EHPA-H₂SO₄ chemical system was selected for this study as the LLE separation of Hf from Zr has shown promising separation factors using D2EHPA, which also has a generally long operational lifetime, is widely available, and is relatively inexpensive, making it well suited for industrial scale applications [29].

This study focussed on the development of a method to assess the technical feasibility of MBSX for the separation of Hf and Zr. A number of studies have already focussed on the chemistry and LLE of the reaction system in combination with the optimisation of the thermodynamic separation factor [23,29,34]. These studies, together with data from literature, were used to select the operation window of the MBSX operation. Therefore, this study was not aimed at further optimisation of the yield and selectivity but was related to obtain a first estimation of the operational feasibility of the MBSX process.

3.2 Equipment

3.2.1 Hollow fibre membrane module

This study used two Liqui-Cel™ 1.7x8.75 Minimodules (see Appendix A2 for the datasheet and dimensional drawing) connected in series for the MBSX experiments. The modules were originally designed for low volumetric flow liquid degassing [72]. As this study formed part of a larger project, to further develop the technology readiness of MBSX for the industrial separation of Zr and Hf, the authors were limited to using these modules.

The design, as illustrated in Figure 3-1, resembles that of a shell and tube heat exchanger, which was originally designed to house liquid on the lumen-side of the membrane and a sweep gas or vacuum applied to the shell-side to assist in the removal of unwanted gases from the liquid. A summary of the module and membrane parameters of the 1.7x8.75 Minimodules are provided in Table 3-2.

In an MBSX application, liquid flows on both sides, where the nature of the membrane (hydrophilic or hydrophobic) determines which fluid wets the membrane and thus fills the pores. Since the polypropylene membranes used are hydrophobic, the organic phase filled the pores of the membrane due to the capillary forces. In this study, the organic phase was pumped through the membrane lumen which resulted in the aqueous-organic interface to be in close proximity to the outer surface of the membranes. This interface was maintained by a combination of the surface tension of the organic phase and a higher pressure on the non-wetting side of the membrane [73]. It is this interface, in combination with the low miscibility between polar and non-polar liquids that prevent the phases from mixing and the bulk movement of one phase into the other. In addition, it is important that a transmembrane pressure (higher on non-wetting side) is maintained during operation to prevent contamination of the non-wetting side by the wetting fluid. The specific transmembrane pressure required for a given membrane module depends on membrane properties such as the pore size, as well as the wetting-fluid properties such as the surface tension and viscosity. In this study, a 0.1 bar transmembrane pressure was sufficient to prevent contamination between the phases.

The outside shell of Liqui-Cel™ 1.7x8.75 Minimodules is made from polycarbonate, which is susceptible to possible degradation when contacted with the organic phase, but is resistant to an H₂SO₄ aqueous phase [74]. Therefore, to protect the modules while avoiding the possibility of contamination of the fluids, the organic phase was pumped through the inside of the membrane fibres (lumen) for all the MBSX experiments thereby avoiding contact with the shell material. The polypropylene membrane fibres and the ethylene propylene diene monomer potting material are both resistant to the organic and aqueous phases and no interaction between the material and the fluids was observed during experimentation.

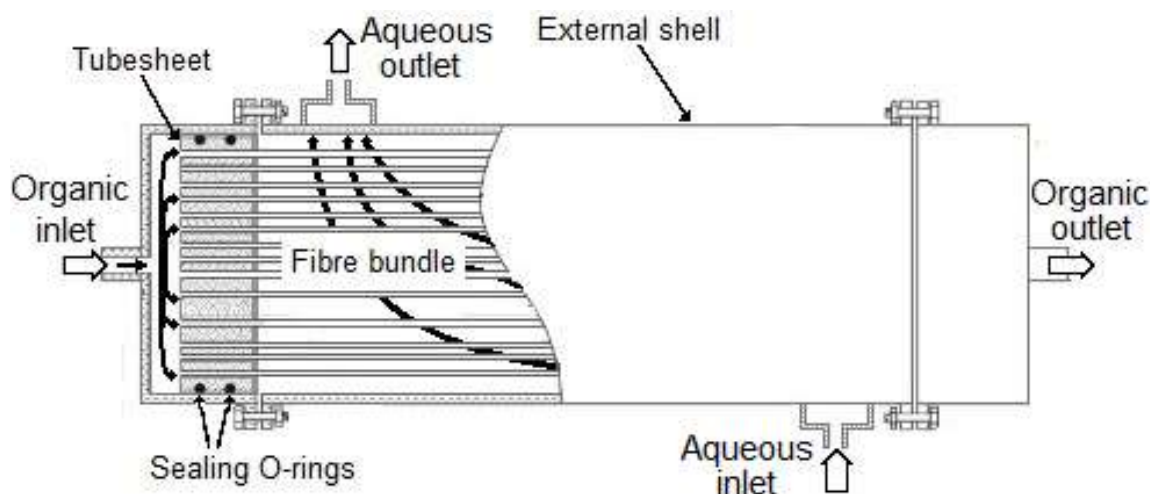


Figure 3-1: Cut-away image of the construction of a typical parallel-flow hollow-fibre membrane module with the organic phase in the lumen flowing counter-currently to the aqueous phase in the shell. Adapted from [75].

Table 3-2: The Liqui-Cel™ 1.7x8.75 Minimodule specifications [72].

Module specifications			Membrane specifications		
Parameter	Value	Unit	Parameter	Value	Unit
Shell OD	42.5	mm	Fibre OD	0.3	mm
Shell ID	36.5	mm	Fibre thickness	40	µm
Overall length	260	mm	Pore size	0.04	µm
Membrane length	198	mm	Porosity	40	%
Shell total volume	270	ml	Surface Area	0.9	m ²
Shell flow volume	189	ml	Approx. fibre count	6500	
Lumen volume	43	ml			

3.2.2 Solution analysis

The metal concentration of all the aqueous samples was analysed by means of inductively coupled plasma optical emission spectrometry (ICP-OES) using the Agilent 5110 ICP-OES.

The calibrations standards that were used consisted of separate 10 000 ppm Zr in H₂O and 1 000 ppm Hf in 5% HCl solutions as supplied by De Bruyn Spectroscopic Solutions. A multiple wavelength calibration approach, where a specific emission wavelength corresponded to a certain concentration range, was used to facilitate the wide range of concentrations expected. The Zr calibration ranges were 0 – 100, 100 – 650, and 650 – 1000 ppm, while the Hf ranges were 0 – 1, 1 – 12.5, and 12.5 - 25 ppm. The calibration error tolerance was set to 10% for all standards, although the calibration errors that were reported by the software fell below 1% for the vast majority of analyses. The experimental samples were diluted with deionised water in a 1:15 ratio prior to analysis.

3.3 Experimental procedures

3.3.1 Solution preparation

All solutions used in this study were freshly prepared in order to minimise the effect of ageing.

3.3.1.1 Aqueous solutions

The aqueous solutions were prepared by adding the required amounts of a mixed Zr(Hf)SO₄ salt and H₂SO₄ to deionised water (Evoqua Labostar). The same concentrations were used for all the experiments conducted in this study and consisted of 16 g.L⁻¹ Zr (0.18 M), 0.36 g.L⁻¹ Hf (0.002 M), and 98 g.L⁻¹ H₂SO₄ (1.0 M).

3.3.1.2 Organic solutions

The organic phase was prepared by mixing the required amounts of D2EPHA and 1-octanol and diluting to the desired volume using Shellsol 2325. For the batch extraction experiments, the E:M molar ratio was varied between 0.11:1 and 5.8:1 by changing the D2EHPA concentration between 6.6 and 330 g.L⁻¹. For the MBSX experiments, the organic phase consisted of 235 g.L⁻¹ (E:M of 4.1:1) D2EHPA and 41 g.L⁻¹ 1-octanol (5 Vol%) in Shellsol 2325. The 1-octanol that was added as a phase modifier to prevent emulsion formation and hasten the phase separation of batch experiments was also added to the MBSX organic phase for consistency [34].

3.3.2 Salt purity analysis

Due to the high concentration of metal salts used in this study (16 g.L⁻¹ Zr), it was not possible to purchase high purity, pre-separated reagents from which the aqueous solutions could be prepared. Instead, industrial-grade Zr(Hf)SO₄ salt from Hangzhou Dayangchem Co. Ltd. (China) was acquired. Since the product assay only stated that the salt contained at least 33% ZrO₂ + HfO₂ and 50% sulphate, it was necessary to determine the exact purity and Hf content before conducting any experiments. The salt purity was determined in-house, using ICP-OES (Agilent 5110), and it was found that 98% of the salt consisted of Zr(SO₄)₂ and Hf(SO₄)₂, with Hf making up 2.23 ± 0.08 wt% of the metal content. Further details regarding the analysis method and data are available in Appendix A3.

3.3.3 Liquid-liquid equilibria (LLE) batch procedure

The method used in this study for the LLE experiments was similar to that described by Wang & Lee (2016) [46]. During the LLE extraction experiments, 20 ml of both aqueous and organic phases were directly contacted in polypropylene bottles, which were agitated in a Labcon 3081U mechanical agitator at 350 rpm, maintaining a temperature of 25 ± 2.0 °C. Taghizadeh *et al.*

(2008) found that 45 minutes would be adequate to reach equilibrium [38]. Accordingly, an experimental time of 60 minutes was used [34].

After 60 minutes, the mixed phases were poured into separation funnels and allowed to stand for approximately 3-5 minutes until the two phases had completely separated. The residual metal content in the aqueous phase was determined using ICP-OES analysis, from which the metal content of the loaded organic was calculated using a mass balance, as described by Eq. 3-1.

$$C_{Org} = (C_{Aq}^{In} - C_{Aq}^{Eq}) \left(\frac{V_{Aq}}{V_{Org}} \right) \quad 3-1$$

3.3.4 MBSX

All the MBSX experiments were conducted using the setup illustrated in Figure 3-2. The membrane contactor column consisted of two Liqui-Cell™ 1.7x8.75 Minimodules connected in series, with a gear pump for the shell-side (aqueous phase) and a peristaltic pump for the lumen (organic phase). All the experiments were conducted under counter-current flow conditions, with the aqueous phase pumped from the bottom of the column upwards to ensure that all the air pockets in the shell were filled with fluid, and the organic phase pumped through the lumen from the top downward. The more restricted flow path of the lumen and higher viscosity of the organic phase allowed the downwards flow of the organic phase to be more uniform than would have been possible if the shell-side had flown downwards. Additionally, because the polycarbonate shell material was susceptible to degradation from contact with the Shellsol 2325 diluent, contact was avoided by always having the organic phase flow through the membrane lumen rather than the shell [74].

As the membrane was wetted by the organic phase, leakages of the organic phase were prevented by applying a transmembrane pressure difference (higher on the aqueous side) over the membrane. Zahakifar et al. (2017) maintained a transmembrane pressure drop of 0.4 bar to prevent phase mixing [76]. In this study, a slight over pressure on the shell-side was realised through means of a 1 m standpipe installed on the shell-side corresponding to a pressure differential of approximately 0.1 bar to prevent breakthrough of the organic phase from the lumen into the shell. Using this stand pipe, no breakthrough was observed during any stage of the MBSX experiments. At the top of the standpipe, the aqueous phase flowed into an open cup connected to a drain line that fed into the shell reservoir (see Figure 3-2).

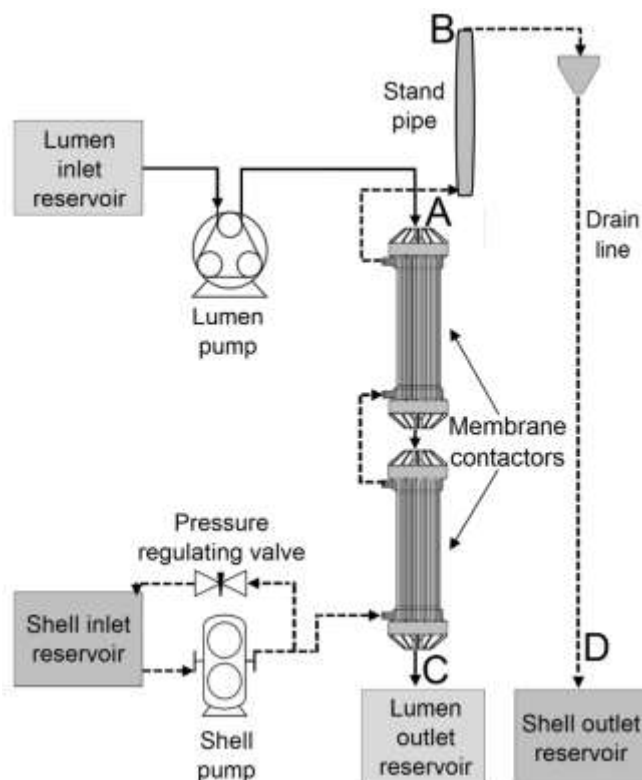


Figure 3-2: MBSX experimental schematic. The dotted lines indicate the shell-side while the solid lines indicate the lumen. Membrane module diagram adapted from [77].

Since no suitable equipment was available for the analysis of the organic phase, a once-through experimental approach was used to avoid the introduction of variables such as i) partial carrier loading, ii) sulphate migration to and build-up in the organic phase, iii) D2EHPA migration to the aqueous phase, or iv) significant changes in the pH of the aqueous phase. While these factors could influence the behaviour of the system, it would not have been possible to quantify them without determining the metal content in the organic phase. Furthermore, the once-through method provided an estimation of steady state operation, which aligned well with the main goal of these experiments, being to generate representative data from which a process model could be built and further evaluated.

The focus of the MBSX experiments was on the mass transfer variables that could not be determined using LLE, namely the flow rates of the shell and lumen, which were thus varied between 0.6 and 15 L.hr⁻¹. The corresponding shell-side fluid velocities ranged from 0.02 to 0.41 cm.s⁻¹ while the lumen velocities ranged from 0.07 to 1.7 cm.s⁻¹. The flow rates that were used were primarily constrained by the capacities of the pumping equipment, the financial constraints of the project, and the accuracy of the analysis equipment. It was difficult to maintain stable flow rates below 0.6 L.hr⁻¹ throughout the experiment, while at flow rates above 15 L.hr⁻¹ the relatively low permeation rates resulted in measured concentration differences between the inlet and outlet which approached the uncertainty of the ICP-OES used to measure the metal concentrations.

3.3.4.1 MBSX operation

The MBSX experimental procedure is discussed stepwise below in accordance with the diagram presented in Figure 3-2.

Pre-experiment preparation:

- The fluid flow rates were calibrated by circulating deionised water and Shellsol 2325 through the shell and lumen of the membrane column, respectively. The flow rate from the lumen pump was controlled by increasing or decreasing the RPM setting on the motor controller. The shell pump flow rate was varied by increasing or decreasing the speed setting of the motor controller while also adjusting the pressure regulating valve (see Figure 3-2) to obtain the correct flow rate through the membrane column. The regulating valve allowed for much finer control over the flow rate through the column than the motor controller. The flow rate of each phase was measured using a measuring cylinder and stopwatch, after which the pump speed was adjusted as required. Once the desired flow rates had been achieved, the pumps were switched off, and the column was emptied before the pumps were connected to the reservoirs housing the experimental solutions.
- The aqueous phase was sampled directly from the reservoir to determine the initial (feed) concentrations of Zr and Hf.

During the experiment:

- To ensure the most efficient possible use of reagents, the lumen-side fluid line was primed by pumping the organic phase to just above the inlet of the membrane column, point "A" in Figure 3-2. Once the organic phase had reached point "A" the peristaltic pump was switched off. As the peristaltic tubing remained clamped down in the pump head, the organic phase remained stationary near the lumen inlet without flowing into the membrane module.
- The shell-side pump was switched on, and the shell-side entirely filled up. Once the aqueous phase in the shell had reached the top of the stand pipe, point "B" in Figure 3-2, the lumen pump was switched back on.
- Once the organic phase began flowing out of the bottom of the membrane column, point "C" in Figure 3-2, a two-minute delay timer was started. At this time the organic phase had completely filled the membrane column. The two-minute delay served as a small window for the system to stabilize as well as for the flow rates to be measured again and corrections to be made if necessary.
- After the two-minute delay had elapsed, the experimental timer of six minutes was started. The first shell-side sample was taken immediately after starting the timer, and subsequent samples every 60 seconds thereafter. Samples of the shell-side were taken at the outflow

of the drain line, point “D” in Figure 3-2. The organic phase was not sampled during the experiments as the available analysis technique was not suitable for organic solutions.

Post-experiment procedure:

- After the experimental time (six minutes) had elapsed, both pumps were switched off, the peristaltic pump head was unclamped, and both the aqueous and organic phases inside the modules allowed to drain under gravity.
- After the free-flow from the modules had stopped, deionised water and clean Shellsol 2325 was pumped through the column to wash any residual reagents from the modules.
- Subsequently, compressed nitrogen was used to clear the membrane lumen of any remaining Shellsol 2325.
- All experimental fluids were disposed of in waste containers as per laboratory regulations.
- Shortly before the ICP-OES analysis, the shell-side samples taken during the experiment were diluted 1:15 with deionised water.

3.4 Uncertainty analysis

In this study, the experimental uncertainties were determined by repeating selected experiments, and the LLE and MBSX experimental uncertainties were calculated separately based on the outlet concentration values. The procedure followed to determine the uncertainties were to, first, to identify and eliminate any data points that were statistical outliers, and second, determine the maximum deviation of each point away from the experimental average of the repeated points, and lastly to round upwards to the nearest 5%. It was also assumed that the uncertainties remained constant throughout the subsequent analysis and modelling.

Outliers were identified using Tukey’s method, with the upper and lower bounds determined by adding or subtracting $1.5 \times \text{IQR}$ (interquartile range) to the third and first quartiles respectively. Data points that fell outside the Tukey fences were eliminated from further consideration.

The uncertainty of the LLE experiments were determined using three repeated data points. The maximum deviations from the overall average of Zr and Hf were 3.5 and 3.0% respectively. The LLE uncertainty was rounded up to 5%.

The experimental uncertainty related to the MBSE experiments were determined using two repeated experiments with 7 data points for each experiment. The maximum deviations from the overall averages were 3.9% for Zr and 5.6% for Hf. The uncertainty of Zr in the MBSE data set was rounded to 5% while that of Hf was rounded to 10%. The subsequent modelling of the mass transfer assumed that the uncertainties of 5 and 10% were maintained.

Tables with the experimental data, and the relevant calculations can be found in Appendix A4.

4 Results and modelling

4.1 Introduction

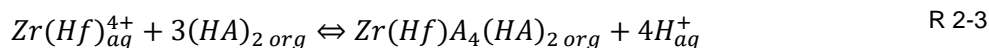
The present study aimed at the development of a method to assess the technical feasibility of MBSX for industrial-scale application. To this end, the selective extraction of Hf from Zr was used as the example system which required making use of experimental data that was generated in a small-scale laboratory unit. It was essential to determine the partition coefficients of both species, and to be able to describe the transfer of species in the form of mass transfer coefficients on both sides of the membrane. While the liquid-liquid extraction experiments (Section 4.2) were used to determine the partition coefficients of Zr and Hf, the MBSX experiments (Section 4.3) were conducted to study the effect of velocity on the mass flux of Zr and Hf for both the shell-side (Section 4.3.1) and the lumen-side (Section 4.3.2). In Section 4.4, the experimental mass transfer data are related to various Sherwood relations, to predict the mass transfer coefficients under various conditions.

In the following sections, when MBSX work is discussed, the terms '*shell*' and '*lumen*' refer to the aqueous phase outside the membrane fibres, and the organic phase inside the membrane fibres, respectively, therefore both the location and the type of fluid are specified.

4.2 Liquid-liquid extraction

The aqueous phase, consisting of 16 g.L⁻¹ Zr (0.18 M), 0.36 g.L⁻¹ Hf (0.002 M), and 98 g.L⁻¹ H₂SO₄ (1.0 M), was contacted with an organic phase of Shellsol 2325 + 1-octanol (5 vol%) and various D2EHPA concentrations between 6.6 and 330 g.L⁻¹. While the work by Wang & Lee (2016) served as the guide for the aqueous phase concentrations used in this study, the low E:M ratio of their study was not used due to the potential of the organic phase quickly becoming saturated in an MBSX column [23]. To avoid such saturation, it was desired to increase the D2EHPA concentration without sacrificing selectivity. Furthermore, the study on the extraction of aroma compounds by Baudot *et al.* (2001) clearly illustrates the importance of the partition coefficient of a species in the mass transfer of an MBSX process, therefore it was vital to determine the partition coefficients of Zr and Hf. According to Baudot *et al.* (2001), K_{OV} (as described in Section 2.6.2, Table 2-3) of a species was found to increase with an increase in the partition coefficient, and that for species with a partition coefficient lower than 20, K_{OV} seemed to reach a plateau at shell-side velocities higher than approximately 1.1 cm.s⁻¹ [18]. Therefore, the LLE experiments were designed to answer three questions: Firstly, can the D2EHPA concentration be increased while maintaining selectivity toward Hf? Secondly, what is the highest separation factor that can be achieved at higher D2EHPA concentrations? Thirdly, what are the partition coefficients of Zr and Hf at these higher concentrations?

During the LLE work, the D2EHPA concentration was varied between 6.6 and 330 g.L⁻¹ (0.02 to 0.95 M, E:M ranged from 0.11:1 to 5.8:1). At the low end of the concentration range, the D2EHPA concentration corresponded to a severely carrier-limited equilibrium, while at the high end, the concentration corresponded to an almost (5.8:1 instead of 6.0:1) stoichiometric ratio, as given by R 2-3, (the most commonly accepted writing of R 2-3 specifies the dimeric form of D2EHPA as (HA)₂, which translates to a stoichiometric ratio of six D2EHPA monomers per molecule of metal).



The unprocessed LLE data, as well as the necessary background to the calculations is provided in Appendix B1. Figure 4-1 illustrates the extraction of Zr and Hf as a function of the D2EHPA concentration. Throughout the experimental range, the extraction of both species increased relatively uniformly. As the available D2EHPA increased, so too did the effective solubility of the metal in the organic phase. It is also evident that, while Hf was preferentially extracted throughout the entire range, the co-extraction of Zr was significant throughout the range as well. The extraction of Zr and Hf increased, from 4.2% and 4.6% at a D2EHPA concentration of 6.6 g.L⁻¹, to 99.6% and 99.9% at a D2EHPA concentration of 330 g.L⁻¹, respectively. The high co-extraction observed, would pose a significant concern for the efficiency of an industrial-scale separation process, by placing possible stress on downstream units, either resulting in unmet purity specifications, or requiring larger and more expensive units to ensure the required purity.

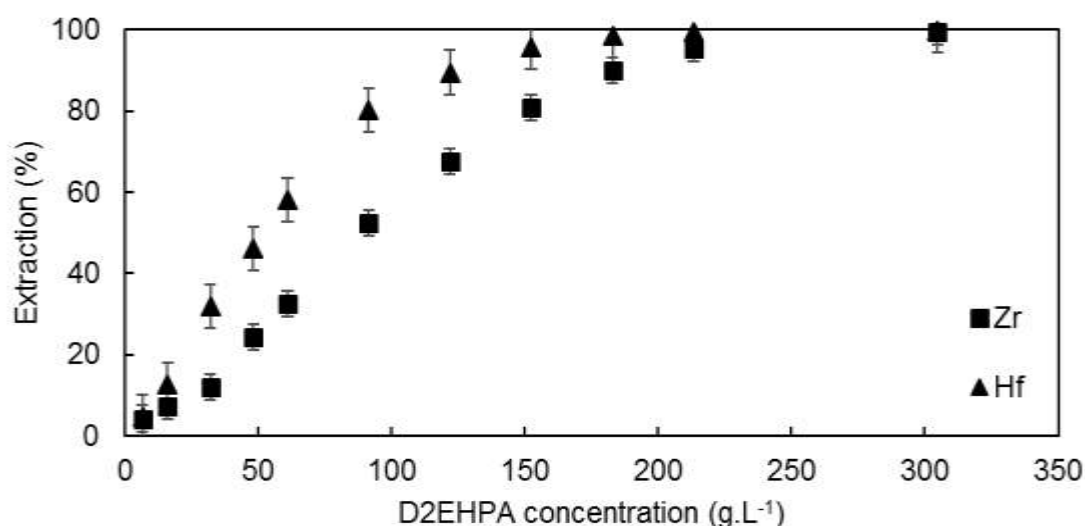


Figure 4-1: The effect of D2EHPA concentration on the extraction of Zr and Hf. [Zr] = 16 g.L⁻¹, [Hf] = 0.36 g.L⁻¹, [H₂SO₄] = 98 g.L⁻¹, [D2EHPA] = 6.6 – 330 g.L⁻¹, [1octanol] = 41 g.L⁻¹ in Shellsol 2325. Agitation = 350 RMP, time = 60 minutes.

The separation factor between Hf and Zr (Eq. 2-1), is illustrated in Figure 4-2 as a function of the E:M ratio, where it can be seen that the separation factor increased with increasing E:M ratios up to a ratio of 4.1:1. The lowest separation factor of 1.2 was obtained at the lowest E:M ratio of 0.11:1, which increased to a maximum of 7.5 at an E:M ratio of 4.1:1. At the highest E:M ratio of

5.8:1, a significant decline in the separation factor (3.9) was observed. The separation factor of 7.5 at an E:M ratio of 4.1:1 (0.73 M or 235 g.L⁻¹ D2EHPA) was in the same order as the maximum separation factors of 8.8 reported by Wang & Lee (2016) [23] and 7.6 reported by Lee *et al.* (2015) [16], although the E:M ratio in the present study was significantly higher. The difference could likely be due to the different experimental conditions, specifically the lower metal concentration used in their studies, as the hydrolysis of Zr and Hf has been shown to not only be concentration-dependent but also strongly influence the extraction equilibrium [23]. The decrease in the separation factor at higher E:M ratios have also been observed by Banda *et al.* (2013) [13], Lee *et al.* (2015) [16], and Wang & Lee (2016) [23], who have attributed this decrease to the relatively high amount of carrier indiscriminately binding to any metal ions remaining in the aqueous phase, thereby negating any efforts at separation.

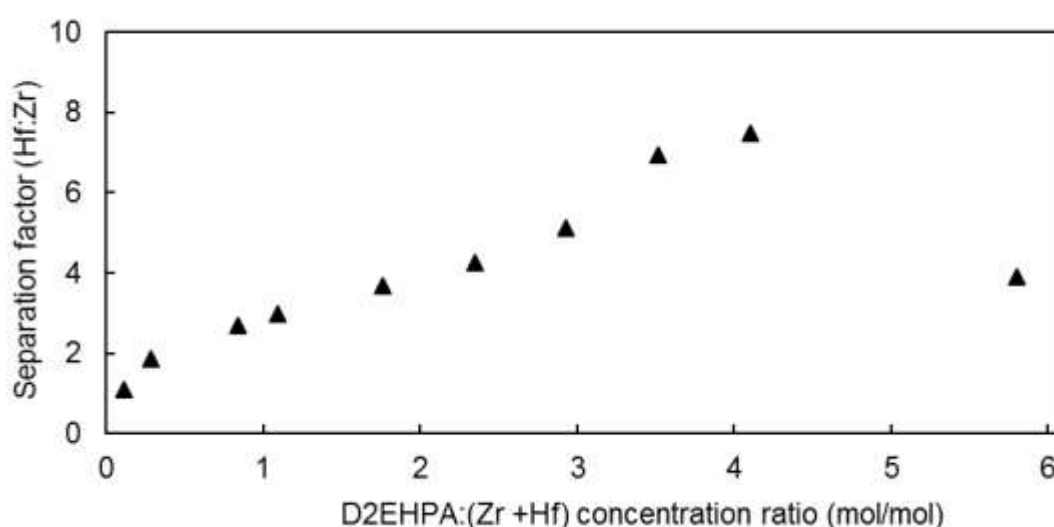


Figure 4-2: The effect of D2EHPA concentration on the separation between Zr and Hf. [Zr] = 16 g.L⁻¹, [Hf]=0.36 g.L⁻¹, [H₂SO₄] = 98 g.L⁻¹, [D2EHPA] = 6.6 – 330 g.L⁻¹, [1-octanol] = 41 g.L⁻¹ in ShellSol 2325. Agitation = 350 RMP, time = 60 minutes.

While the separation factor obtained in this study was similar to other Hf-selective D2EHPA-H₂SO₄ systems that have been listed in Table 2-1, it was significantly lower than the separation factor (24) of the Cyanex 272-H₂SO₄ system that was reported by Lee *et al.* (2015) [16]. While Cyanex 272 would appear superior to D2EHPA in terms of the separation that can be achieved, the high acid concentration required (6.0 M) for the Cyanex 272-H₂SO₄ system would require specialist materials capable of withstanding such aggressive conditions. According to Banda & Lee (2015), the separation factors of the commercial MIBK and TBP processes are approximately 7 and 10, respectively [6]. This shows that the separation factor of 7.5 obtained in this study could be sufficient for an industrial-scale SX process, and hence for the purpose of this study.

The effect of the D2EHPA concentration on the partition coefficients (Eq. 2-2) of Zr and Hf is illustrated in Figure 4-3. The partition coefficients of Zr increased from 0.04 at an E:M of 0.11:1

to 232 at an E:M of 5.8:1, while that of Hf increased from 0.05 to 745 over the same E:M range. The partition coefficients of Zr and Hf at the point of best separation at an E:M of 4.1:1 were 21 and 156, respectively.

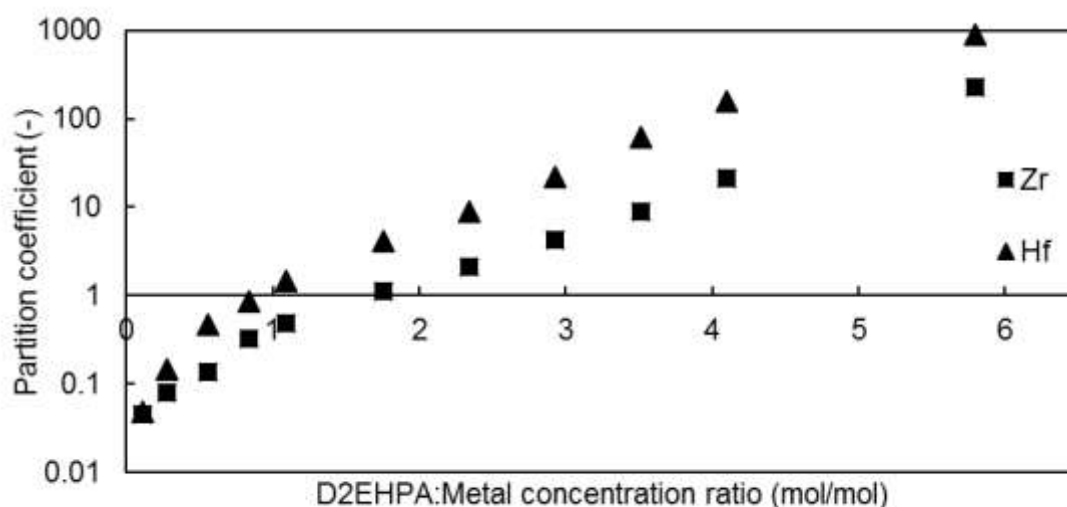


Figure 4-3: The effect of D2EHPA concentration on the partition coefficients of Zr and Hf. [Zr] = 16 g.L⁻¹, [Hf] = 0.36 g.L⁻¹, [H₂SO₄] = 98 g.L⁻¹, [D2EHPA] = 6.6 – 330 g.L⁻¹, [1-octanol] = 41g.L⁻¹ in ShellSol 2325. Agitation = 350 RMP, time = 60 minutes.

Log (P) vs. Log [(D2EHPA)₂] plots were constructed for Zr and Hf, and the slopes for both Zr and Hf were determined to be approximately 4, indicating that at high metal concentrations or high levels of organic phase saturation the stoichiometric number of D2EHPA dimer molecules required in the extracted complex might be higher (4 vs. 3) than is described by R 2-3. This could result in lower than expected extraction values for a process, due to unexpectedly high usage of the carrier, which could, however, be mitigated by using a higher carrier concentration or larger phase ratio. However, while further studies on both the reaction stoichiometry, and the complexation behaviour at various aqueous concentrations and organic phase saturations are recommended, these aspects fell beyond the scope of this study.

The liquid-liquid extraction experiments posed three questions which can now be answered as follows. Firstly, the selectivity toward Hf can be maintained, even improved, with increasing D2EHPA concentrations. Secondly, the maximum separation factor achieved was 7.5 at a D2EHPA concentration of 235 g.L⁻¹ (0.73 M, E:M 4.1:1). Lastly, the partition coefficients of Zr and Hf at this concentration were 21 and 156, respectively. A D2EHPA concentration 0.72 M was subsequently used for all MBSX experiments.

4.3 MBSX

The objectives of the MBSX experiments were to determine K_{OV} of both Zr and Hf at various shell and lumen velocities and how the velocity of each phase influenced the resistance to mass

transfer. The flow rates of both phases were varied between 0.6 and 15 L.h⁻¹, while maintaining the other phase at 6.0 L.h⁻¹. All the experiments were conducted under laminar flow conditions, with Reynolds numbers varying between 0.03 and 1.52 throughout all the MBSX experiments.

General observations of the MBSX experiments

Prior to the first use, the fibres in all the modules were straight with no obvious non-uniformity in the fibre bundles. During the first contact with the organic phase, all the modules exhibited longitudinal swelling, which, restricted to outward movement by the module construction, caused the membrane fibres to buckle and create channels through which the shell-side fluid flowed selectively. This was not entirely unexpected, as Asimakopoulou & Karabelas (2006) also reported the possible swelling of the polypropylene fibres used in their study [64]. While it is reasonable to assume that the swelling negatively affected the spacing, and therefore the flow between the fibres, this was only observed and verified visually. This maldistribution can be seen in Figure 4-4, which shows a colour-enhanced photo of the working membrane contactor. The shell-side (aqueous phase) was coloured green, while the lumen-side (organic phase) was coloured blue.



Figure 4-4: A colour-enhanced photo illustrating shell-side channelling (large green bands) and lumen-side maldistribution (vertical striations in blue fibres). Note that the photo has been rotated 90° counter-clockwise for the purposes of this document, under normal conditions the module was oriented upright with the bottom shell-side inlet seen on the right of the clamp.

In Figure 4 4, the two large green bands near the centre of the module clearly show that a significant part of the shell-side membrane surface area was bypassed with little contact between the aqueous phase located in the shell and the membrane. The colour intensity of the bands is an indication of the thickness of the liquid layer, and therefore, the distance between the membrane fibres and the shell wall, with a darker colour indicating a larger distance. A third, lightly coloured band is also visible at the inlet of the shell-side (far right of Figure 4 4). The distance between the fibres and the shell wall is relatively small near the shell-side inlet (right of the clamp), increasing significantly towards the centre of the module. Both the longitudinal

swelling of the membranes after contact with the organic phase and the restriction to outward movement by the module construction caused the fibres to buckle forming the observed channels.

The blue sections of Figure 4 4 indicate that large portions of the shell were in direct contact with the membrane fibres (the blue coloured organic phase filled the membrane pores, resulting in the clearly visible colouring) and therefore had no clearly visible contact with the aqueous phase on the side visible to the observer. It can further be seen that some striations in the membrane fibres were present, indicating that not all of the membrane fibres were filled by the organic phase. This could be due to malformation of the membranes resulting in a more restricted flow path and therefore the organic phase would preferentially flow through other membrane fibres. While the combined effects of shell-side channelling and lumen-side maldistribution would impact the overall rate of mass transfer, investigating this further fell beyond the scope of this study.

No breakthrough of the bulk organic phase into the aqueous phase was observed during any of the MBSX experiments.

It should be noted that the once-through configuration of the MBSX experiments required large phase volumes, making the experiments costly to perform. The same comment regarding once-through operation was made by Kertész *et al.* (2005) [35].

For each experimental run, the shell-side was filled before commencing with the pumping of the lumen phase. To achieve the best approximation of steady state, a delay timer of two minutes was started after the lumen phase flowed continuously from the bottom of the membrane column, the first sample was only taken from the shell-side outlet after the two-minute delay had expired. The delay between the points where both sides of the module were completely filled and the first samples being taken was the most practical approach to achieving steady state under the limitations of the study. The data illustrated in Figure 4-5, Figure 4-6, Figure 4-9, and Figure 4-10 showed that the experiments operated under conditions that were sufficiently stable for the purpose of the present study.

It was observed that significant variations in the measured shell-side feed concentration data was reported by the ICP-OES despite a careful and consistent process that was followed to prepare the feed solutions and samples for analysis. The reported Zr feed concentrations varied between 14.4 and 18.4 g.L⁻¹, while the Hf concentration ranged between 0.33 and 0.40 g.L⁻¹. Minor variations in the measured feed concentrations were expected as each experiment required the preparation of fresh solutions (nine sets of solutions in total), and all the samples were individually diluted prior to analysis. However, the large variations observed in the feed concentrations were more likely the result of calibration variances and the operational method of the ICP-OES. To compensate for these variations the measured concentration data were normalised to the specified baseline Zr and Hf concentrations of 16.0 and 0.357 g.L⁻¹ respectively. The Hf concentration used was based on the salt purity analysis (see Section 3.3.2) showing that Hf

made up 2.23 ± 0.08 wt% of the metal content in the salt. The concentration data was normalised by dividing the measured outlet concentration by the measured feed concentration for each experiment to determine the outlet: inlet ratio, which was multiplied by 16.0 in the case of Zr, or 0.357 in the case of Hf, as per Equations 4-1 and 4-2, respectively.

$$C_{normalised}^{Zr} = 16.0 \left(\frac{C^{Out}}{C^{In}} \right) g \cdot L^{-1} \quad 4-1$$

$$C_{normalised}^{Hf} = 0.357 \left(\frac{C^{Out}}{C^{In}} \right) g \cdot L^{-1} \quad 4-2$$

All subsequent calculations of the mass transfer behaviour were based on the normalised concentration values. The actually measured concentration data, a discussion on the normalising procedure, as well as the normalised data are presented in Appendix B2.

Near the end of the experimental work, all the modules were destroyed by large cracks which formed in the poly carbonate shells, and sufficiently large cracks ripped the potting material, making repairs impossible. The irreparable damage to the modules made it impossible to repeat experiments. It is suspected that despite the effort to clean the modules after use the polycarbonate shells were chemically degraded by the H_2SO_4 present in the aqueous phase, despite polycarbonate reported to have excellent resistance to the concentration of acid used in this study [74].

The MBSX data, both raw and processed, and discussions of the calculations is provided in Appendix B2.

4.3.1 Influence of the shell-side velocity

The effect of the shell-side velocity on the shell-side outlet concentrations of Zr and Hf is shown in Figure 4-5 and Figure 4-6, respectively. The dotted lines in each figure indicate the average outlet concentration of the specific experiment, while the error bars indicate the standard error of the mean. It is clear that the outlet concentration was strongly affected by the flow velocity with the outlet concentration increasing along with velocity. Both Figure 4-5 and Figure 4-6 clearly show that, despite the short operational time, an acceptable degree of steady state was achieved during the experiments which provided results that were sufficient for the purpose of estimating the influence of the shell-side flow velocity on the mass transfer coefficients of Zr and Hf.

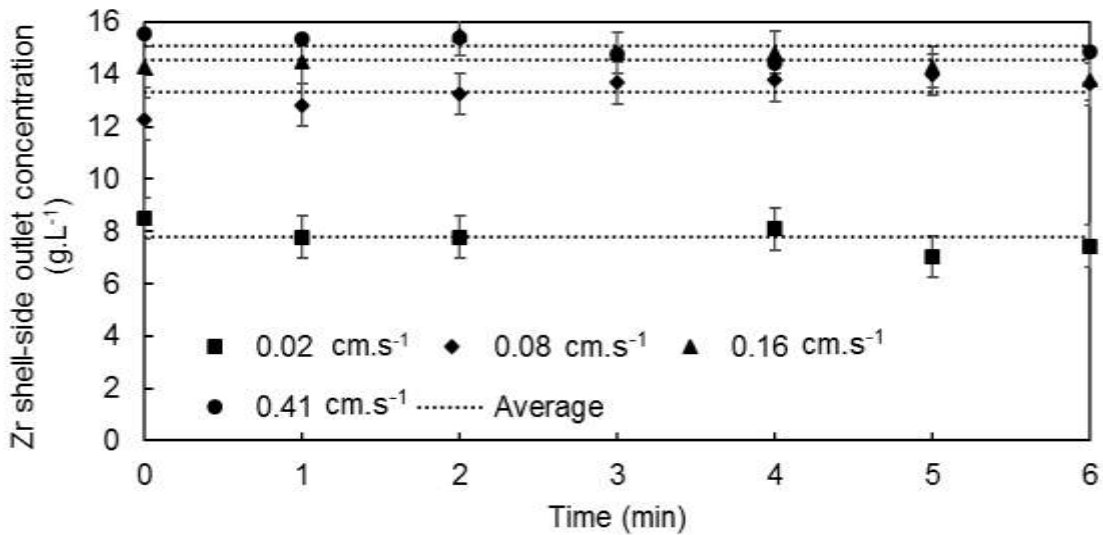


Figure 4-5: The shell-side outlet Zr concentration as a function of time and shell-side velocity. The dotted lines represent the average of each experiment and are included to guide eye of the reader. $[Zr] = 16 \text{ g.L}^{-1}$, $[Hf] = 0.36 \text{ g.L}^{-1}$, $[H_2SO_4] = 98 \text{ g.L}^{-1}$, $[D2EHPA] = 235 \text{ g.L}^{-1}$, $[1\text{-octanol}] = 41 \text{ g.L}^{-1}$ in ShellSol 2325.

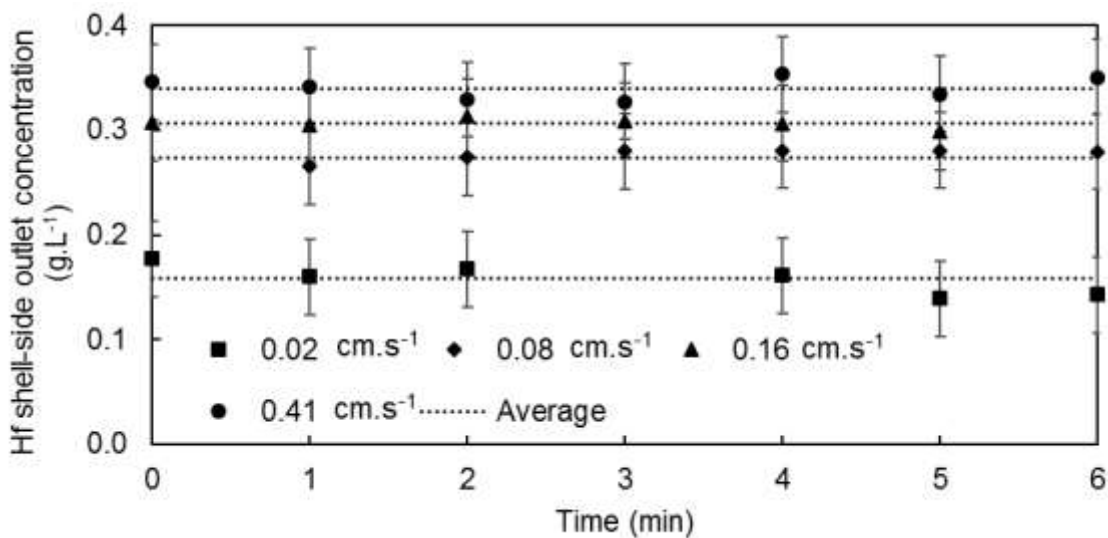


Figure 4-6: The shell-side outlet Hf concentration as a function of time and shell-side velocity. The dotted lines represent the average of each experiment and are included to guide eye of the reader. $[Zr] = 16 \text{ g.L}^{-1}$, $[Hf] = 0.36 \text{ g.L}^{-1}$, $[H_2SO_4] = 98 \text{ g.L}^{-1}$, $[D2EHPA] = 235 \text{ g.L}^{-1}$, $[1\text{-octanol}] = 41 \text{ g.L}^{-1}$ in ShellSol 2325.

The average extraction of Zr and Hf as a function of the shell-side velocity is illustrated in Figure 4-7. The apparent decrease in the extraction observed at higher shell-side velocities has been reported by Bocquet *et al.* (2005) [53], Fadaei *et al.* (2011) [33], and Chaturabul *et al.* (2015) [54]. While Bocquet *et al.* (2005) attributed the reduction in the extraction efficiency to the reduction in the residence time of the shell, it would not adequately describe the apparent decrease in extraction with the increased velocity [53]. Rather, the increase in the shell-side velocity had two relevant effects which would affect the measured extraction. Firstly, the thickness of the shell-side boundary layer would decrease, decreasing the shell-side resistance to mass transfer

resulting in an increased mass flux through the membrane, this is illustrated Figure 4-8. Secondly, the mass flow rate would increase due to the increased volumetric flow rate through the shell-side. However, under conditions where the increase in the mass flow rate was greater than that of the mass flux through the membrane, the measured extraction decreased as the mass flux through the membrane became a smaller component of the total mass flow and the subsequent change in concentration became smaller, thereby resulting in an apparent decrease in the extraction values.

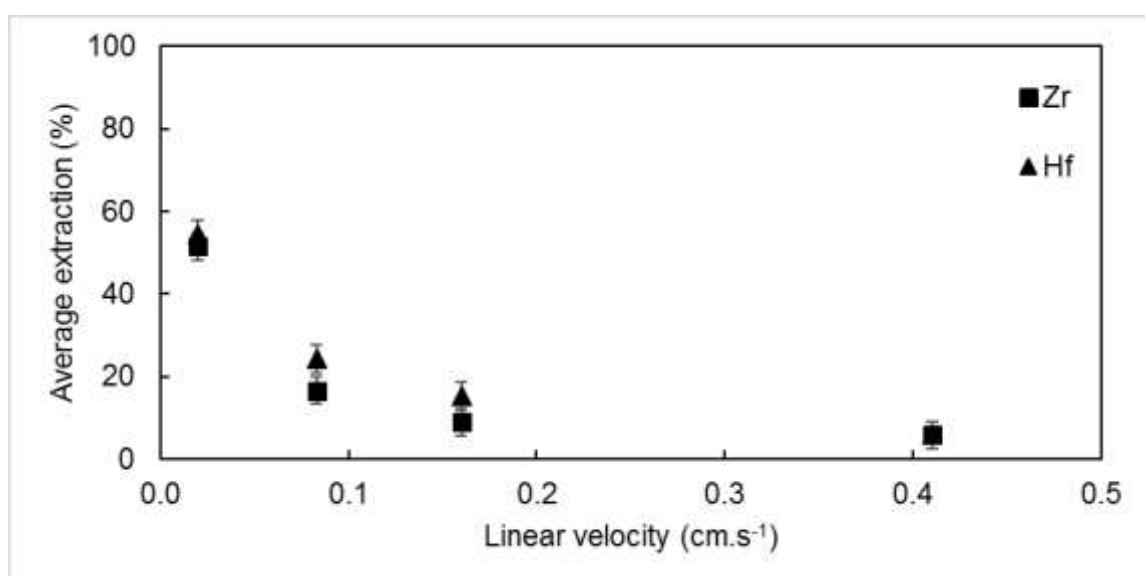


Figure 4-7: The effect of the shell-side velocity on the extraction of Zr and Hf. $[Zr] = 16 \text{ g.L}^{-1}$, $[Hf] = 0.36 \text{ g.L}^{-1}$, $[H_2SO_4] = 98 \text{ g.L}^{-1}$, $[D2EHPA] = 235 \text{ g.L}^{-1}$, $[1\text{-octanol}] = 41 \text{ g.L}^{-1}$ in ShellSol 2325.

It is evident when comparing Figure 4-1 to Figure 4-7 that the co-extraction of Zr was more pronounced during the shell-side variation experiments than during the LLE experiments. *While the extraction favoured Hf*, as expected, it is clear from Figure 4-7 that the closely matched extraction values of Zr and Hf significantly reduced the separation that was achieved in the MBSX setup as compared to that of the LLE.

The separation ratio attained at the lowest velocity (0.02 cm.s^{-1}) was 1.1, which was attributed to a low shell-side mass transfer coefficient, creating an environment similar to the highest E:M ratio of Section 4.2 where the carrier indiscriminately extracted any metal ions which diffused through the shell-side boundary layer to the membrane surface. The highest separation ratio of approximately 1.7 was achieved at a shell-side velocity of 0.16 cm.s^{-1} , which was approximately 4 times lower than the LLE separation factor at equilibrium conditions. As the velocity increased to 0.41 cm.s^{-1} , the separation ratio decreased to approximately 1.

Yang et al. (2002) also found that the LLE separation factor of approximately 20 could not be replicated in their MBSX setup, where a maximum separation ratio of approximately 6.5 was achieved [14]. They attributed this discrepancy to the membrane, creating a low-selectivity

resistance to mass transfer dominating the overall rate of mass transfer. In the present study, the discrepancy between the LLE separation factors, which has been discussed in Section 4.2, and the MBSX separation ratio, indicated that a non-selective resistance was likely to dominate the overall rate of mass transfer. Further, as the metal ions are approximately the same size, it was expected that the diffusion coefficients of Zr and Hf through the shell-side boundary layer would be similar, resulting in similar mass transfer coefficients of Zr and Hf. Based on this, it can be assumed that the non-selective diffusion of the metal ions through the shell-side boundary layer most likely limited the overall rate of mass transfer thereby negating any efforts to attain separation between Zr and Hf.

The effect of the shell-side velocity on the mass flux of Zr and Hf is illustrated in Figure 4-8. The trend with which the mass flux of both Zr and Hf increased were closely matched throughout the range of tested shell-side velocities. The increased mass flux was attributed to a greater degree of local turbulence of the shell-side fluid around the membrane fibres at the higher velocities. This turbulence reduced the shell-side boundary layer thickness, which improved the mass transfer coefficients on the shell-side. The mass flux of Zr was approximately 28 to 41 times higher than that of Hf, which was attributed to the approximately 50 times higher concentration of Zr in the shell, resulting in a higher driving force for mass transfer.

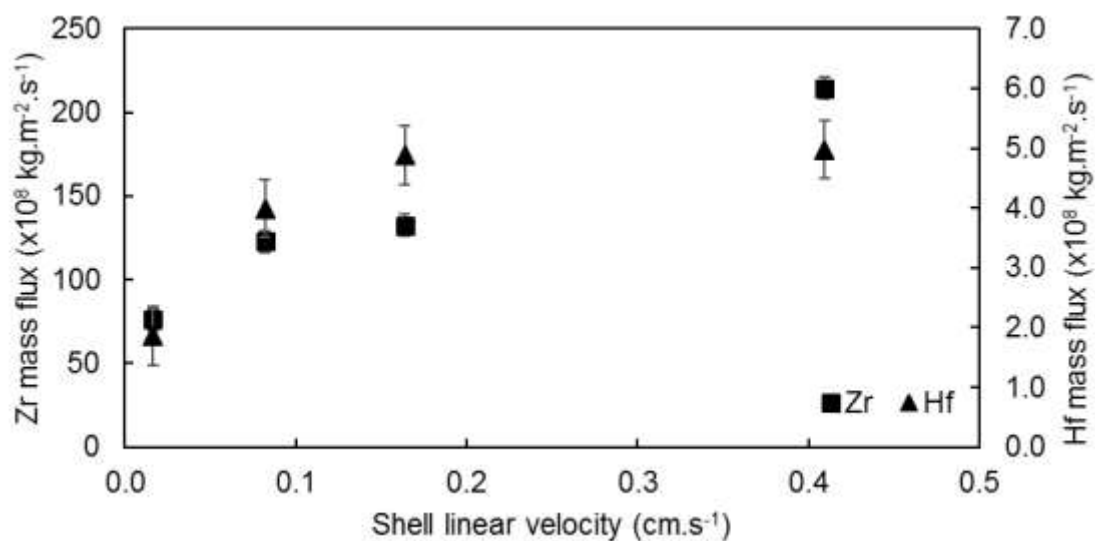


Figure 4-8: The effect of the shell-side velocity on the mass flux of Zr and Hf. [Zr] = 16 g.L⁻¹, [Hf] = 0.36 g.L⁻¹, [H₂SO₄] = 98 g.L⁻¹, [D2EHPA] = 235 g.L⁻¹, [1-octanol] = 41 g.L⁻¹ in ShellSol 2325.

According to Gabelman & Hwang (1999), species exhibiting high partition coefficients such as Hf (157), in combination with hydrophobic membranes (would be expected to be strongly influenced by the velocity of the aqueous phase [17]. According to Baudot *et al.* (2001), a species exhibiting a partition coefficient above 20, such as Hf, would likely have the dominant resistance to mass transfer in the aqueous phase, and therefore the aqueous phase mass transfer coefficient would benefit greatly from an increased aqueous phase velocity [18]. On the other hand, for species

exhibiting partition coefficients near or below 20, such as Zr (20.7), it would be expected that the resistance to mass transfer would be more balanced between the shell and lumen resistances, and therefore, not benefit as much as Hf from an increased shell-side velocity. However, as the data reported in Figure 4-5 and Figure 4-6 showed very similar trends for both metals, it was clear that under the present conditions the effect of a high partition coefficient of a species, as noted by Baudot *et al.* (2001), alone could not be used to predict the separation efficiency of an MBSX system. As supported by the low separation ratio of the experiments, it was suspected that under the conditions of the present study a non-selective resistance limited the rate of mass transfer to the extent that the separation that was expected based on the LLE partition coefficients of Hf and Zr was not achieved.

4.3.2 Influence of the lumen-side velocity

The effect of the lumen velocity on the shell-side outlet concentrations of Zr and Hf is illustrated in Figure 4-9 and Figure 4-10, respectively. The dotted lines in the figures represent the average shell-side outlet concentration of all the experiments, while the error bars represent the standard error of the mean. It can be seen in both figures that increasing the lumen velocity from 0.07 to 1.7 cm.s⁻¹, (an increase by a factor of 24) had relatively little impact on the outlet concentration of either Zr or Hf compared to the effect of the shell-side velocity. The extraction of Zr increased from 4.7 to 12.0% and the extraction of Hf increased from 6.0 to 16.8% between the slowest and fastest lumen velocities tested. It was most likely that the lumen velocity was high enough to ensure that the D2EHPA in the membrane could be refreshed faster than the Zr and Hf could diffuse toward the shell-lumen interface, therefore, the D2EHPA was essentially the reagent in excess and did not contribute significantly to the resistance to mass transfer.

The mass flux of Zr and Hf is illustrated in Figure 4-11. Note that the 0.34 cm.s⁻¹ data point was excluded from further calculations, as the mass flux values of Zr (32×10^{-7} kg.m⁻².s⁻¹) and Hf (0.8×10^{-7} kg.m⁻².s⁻¹) were markedly higher than that of all the other data collected in the series of experiments, possibly indicating that an error had occurred during the experiment. Unfortunately, as the polycarbonate shells of the modules had cracked during the course of the experimental work and could not be repaired or replaced, it was not feasible to repeat the experiment to determine the mass flux at this condition. An investigation into the chemical compatibility between the materials and chemical reagents found that the compatibility between polycarbonate and Shellsol 2325 would be problematic, however, from the observations of the modules, the shell was structurally chemically degraded by the aqueous phase.

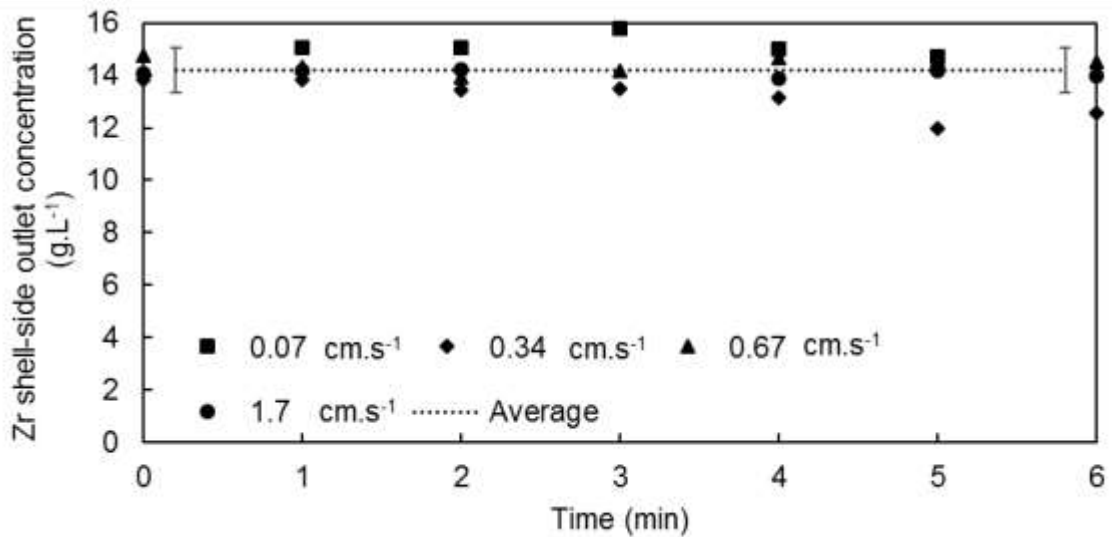


Figure 4-9: The shell-side outlet Zr concentration as a function of time and lumen-side velocity. The dotted lines represent the average of all the experiments and are included to guide eye of the reader. [Zr] = 16 g.L⁻¹, [Hf] = 0.36 g.L⁻¹, [H₂SO₄] = 98 g.L⁻¹, [D2EHPA] = 235 g.L⁻¹, [1-octanol] = 41 g.L⁻¹ in ShellSol 2325.

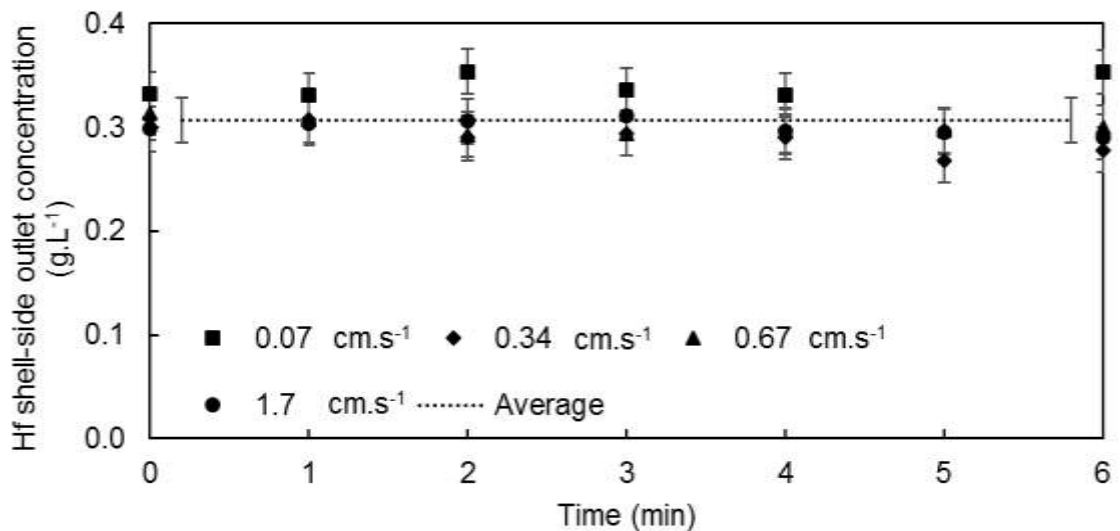


Figure 4-10: The shell-side outlet Hf concentration as a function of time and lumen-side velocity. The dotted lines represent the average of all the experiments and are included to guide eye of the reader. [Zr] = 16 g.L⁻¹, [Hf] = 0.36 g.L⁻¹, [H₂SO₄] = 98 g.L⁻¹, [D2EHPA] = 235 g.L⁻¹, [1-octanol] = 41 g.L⁻¹ in ShellSol 2325.

The mass flux values of Zr and Hf as a function of the lumen velocity are illustrated in Figure 4-11. From 0.07 to 0.67 cm.s⁻¹, the mass flux of Zr and Hf increased by factors of 2.1 and 2.8 respectively, but only small increases (factors of 1.2 for Zr, and 1.0 for Hf) were observed when the velocity was increased from 0.67 to 1.7 cm.s⁻¹. This indicated that the contribution of the lumen to the overall resistance to mass transfer was only significant at very low velocities. It is suspected that the refresh rate of D2EHPA at such low velocities allowed a certain degree of saturation to occur, which could have resulted in agglomerated organometallic complexes which

exhibit much lower diffusion coefficients than the single, smaller complexes, effectively forming a plug in the pore which reduced the mass flux through the membrane. Increasing the lumen velocity above 0.67 cm.s^{-1} seemed to reduce the lumen contribution to the overall resistance to the extent that it became nearly negligible. Based on the data illustrated in Figure 4-11, it was concluded that under the present conditions, the contribution of the lumen boundary layer to the overall resistance to mass transfer could be expected to be negligible as long as the lumen velocity was maintained above 1.5 cm.s^{-1} .

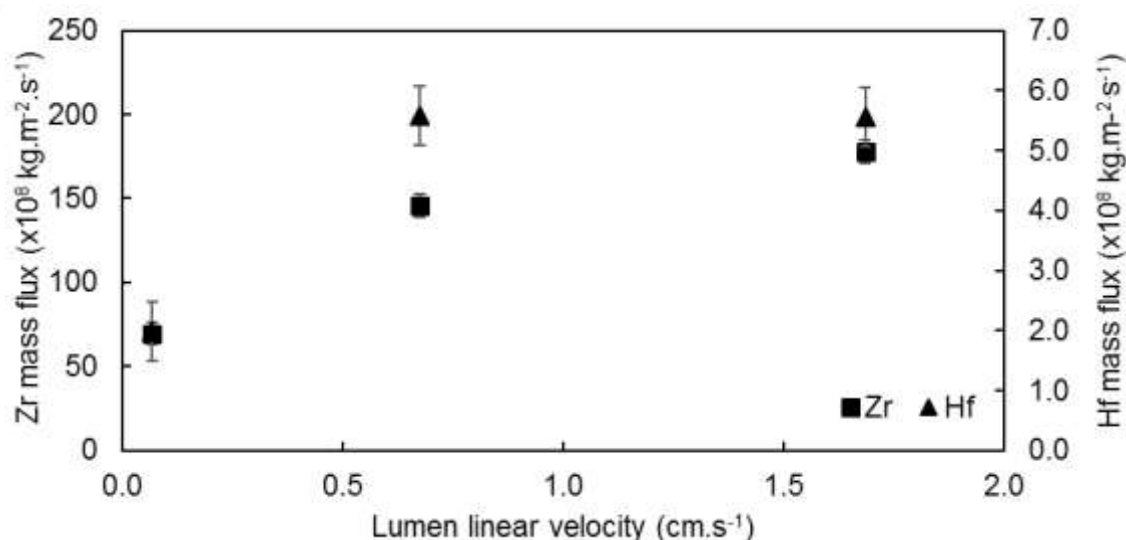


Figure 4-11: The effect of the lumen velocity on the mass flux of Zr and Hf. $[\text{Zr}] = 16 \text{ g.L}^{-1}$, $[\text{Hf}] = 0.36 \text{ g.L}^{-1}$, $[\text{H}_2\text{SO}_4] = 98 \text{ g.L}^{-1}$, $[\text{D2EHPA}] = 235 \text{ g.L}^{-1}$, $[\text{1-octanol}] = 41 \text{ g.L}^{-1}$ in ShellSol 2325.

The highest separation ratio of the study (1.8) was observed at a lumen velocity of 0.67 cm.s^{-1} , while the average separation ratio of both series of experiments was 1.4. The low separation ratio observed throughout all the MBSX experiments indicated that the success of an MBSX process cannot be estimated based on LLE data only, and that mass transfer data must be included to assess the feasibility of MBSX for industrial applications.

4.4 Mass transfer modelling

The project objective (see Section 1.3) regarding the proposal of a process model required two components, i.e. i) a method of describing the mass flux of Zr and Hf through the membrane as a function of the flow velocity, and ii) a way to describe the concentration profile along the surface of a membrane contactor. The mass flux is discussed in the current section (4.4), while the concentration profile is discussed as part of Chapter 5, specifically Section 5.4.

To describe the mass flux, a resistance-in-series approach was used. This approach considers the total resistance to mass transfer to consist of a series of sequential steps which contribute their own resistance to the whole. The resistance of each step in the series was estimated using relations found in literature and compared to the experimental data. Finally, Sherwood relations

were fit to the experimental data, in order to provide more accurate predictions of the shell-side mass transfer coefficients.

As mentioned previously (Sections 1.3 and 1.4.3), it was more important for this study to generate mass transfer data which could be utilised for the development of the MBSX assessment methodology, than finding data representing the best set of operating conditions. The mass transfer data, as well as a discussion on the calculations used, is provided in Appendix B3.

4.4.1 Overall mass transfer coefficient

The average outlet concentration determined for each experiment was used for all the calculations in this section, assuming that the experiments operated at steady state, or as close as possible within the confines of this study. The mass transfer data, and the discussions on the calculations is provided in Appendix B3.

The overall mass transfer coefficient (K_{OV}) lumps the contributions of the shell, membrane, and lumen mass transfer coefficients as well as the partitions coefficients into a single term that was determined using the experimental data as per Eq. 2-14:

$$K_{OV} = \frac{Q_{Shell}\Delta C_{Shell}}{A_{Mem}\Delta C_{LM}} \quad 2-14$$

The overall mass transfer coefficients for the MBSE experiments (Section 4.3.1 and 4.3.2) were determined for Zr and Hf, and are illustrated in Figure 4-12 and Figure 4-13, respectively. From the mass transfer behaviour of Zr (Figure 4-12), two distinct observations were made. Firstly, the mass transfer coefficient seemed to exhibit plateauing behaviour for lumen velocities between 0.67 and 1.7 cm.s⁻¹, indicating that the influence of the lumen phase on the overall rate of mass transfer was small, as was also shown in Section 4.3.2. According to the study published by Baudot *et al.* (2001), the small impact of the lumen velocity would be unexpected, as the relatively low partition coefficient of Zr (20.7) would indicate that the solubility of Zr (as a Zr-D2EHPA complex) in the organic phase would inhibit the rate of mass transfer [18]. The second observation from Figure 4-12 is that it appears that K_{OV} of Zr increased significantly at the higher shell-side velocities tested, and could potentially still increase further at velocities above the experimental range. Based on the observed behaviour, it was also evident that the majority of the resistance to the mass transfer of Zr was located in the shell. Compared to the data reported by Baudot *et al.* (2001), the K_{OV} values for Zr and Hf were quite low, which in this case could likely be explained by the high packing factor and the swelling of the membrane fibres which resulted in non-uniform flow conditions throughout the module where much of the membrane surface had none of the aqueous feed flowing past [18].

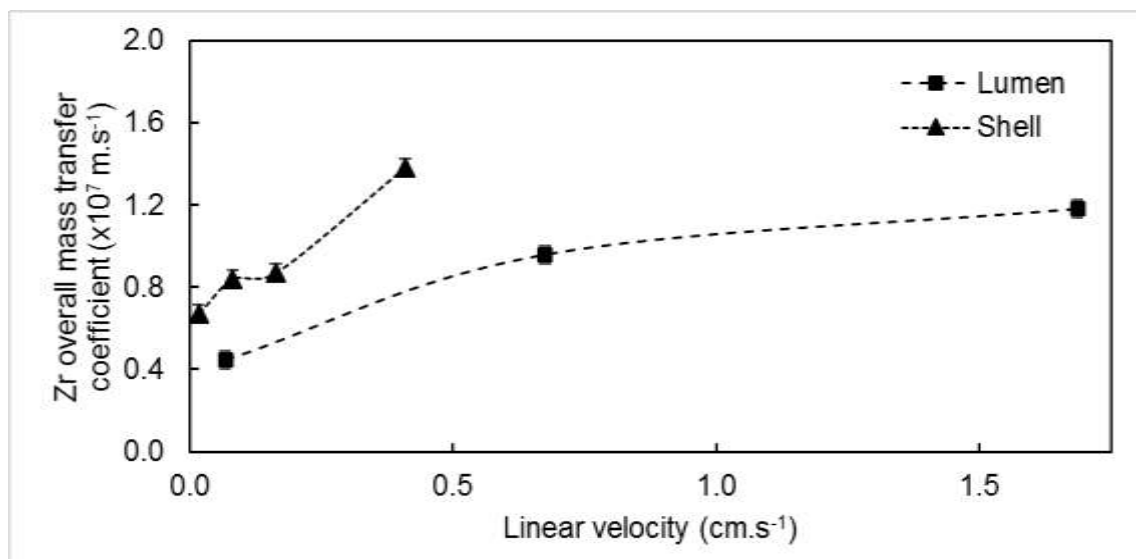


Figure 4-12: The effect of the shell and lumen velocity on the overall mass transfer coefficient of Zr.

The effect of the linear velocity of the shell and lumen on the overall mass transfer coefficient behaviour of Hf, illustrated in Figure 4-13, showed the same plateauing behaviour as the lumen velocity was increased, however at a higher value. As the partition coefficient of Hf was approximately 157, indicating high solubility in the organic phase, therefore, it was expected that the lumen velocity would not have a significant impact on the K_{OV} of Hf. On the other hand, the shell side velocity mass transfer behaviour of Hf, seems to contradict the prediction that has been described by Baudot *et al.* (2001), as species with a high partition coefficient would be expected to be strongly limited by the shell-side velocity under the current experimental conditions [18]. The work published by Mans (2018) also showed that the partition coefficient of a species played an important part in the rate of mass transfer during the extraction of Co and Ni with Cyanex 272 [48]. It is believed that, in the present study, the resistance of the shell was such that it severely limited the rate of mass transfer for both Zr and Hf through the shell boundary layer, and that the E:M ratio at the extraction interface was significantly higher than that of the bulk solutions. From the LLE data illustrated in Figure 4-2 it was observed that the separation factor decreased at high E:M ratios, and it is suspected that this contributed to the low separation ratio observed during the MBSX experiments. The similar diffusion coefficients of the shell-side resulted in non-selective mass transfer of Zr and Hf through the shell-side boundary layer. Therefore, the possibility of a correlation of a high rate of mass transfer associated with a species with a high partition coefficient should be investigated and verified experimentally, as a non-selective resistance to mass transfer may adversely affect the expected K_{OV} and separation ratio if it contributes significantly to the total resistance to mass transfer.

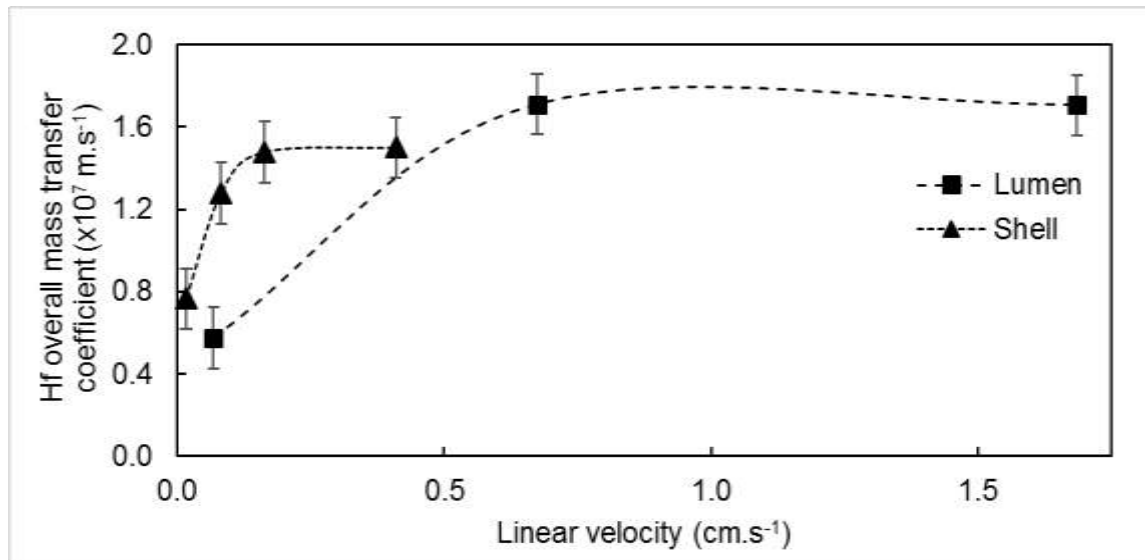


Figure 4-13: The effect of the shell and lumen velocity on the overall mass transfer coefficient of Hf.

4.4.2 Individual mass transfer coefficients

The overall mass transfer coefficient, K_{OV} , as discussed in Section 4.4.1, consists of three mass transfer coefficients acting in series, as given in Eq. 2-11.

$$\frac{1}{K_{OV}} = \frac{1}{k_{Shell}} + \frac{d_{OD}}{Pk_{Mem}d_{LM}} + \frac{d_{OD}}{Pk_{Lumen}d_{ID}} \quad 2-11$$

The membrane and lumen mass transfer coefficients were determined using Eqs. 2-16 and 2-19, respectively:

$$k_{Mem} = \frac{D_{AB}\epsilon}{\tau\delta} \quad 2-16$$

$$Sh_{Lumen} = \frac{k_{Lumen}d_H}{D_{AB}} = 1.5 \left(\frac{d_L^2 U_L}{LD_{AB}} \right)^{0.33} \quad 2-19$$

The shell-side coefficient was determined by rearranging Eq. 2-11, and using K_{OV} determined in Section 4.4.1 (see Figure 4-12 and Figure 4-13), as well as the predictions of the membrane and lumen mass transfer coefficients, determined with Eqs. 2-16 and 2-19. The parameters and their corresponding values that were used to determine the various mass transfer coefficients, are listed in Table 4-1. The method used to estimate the diffusion coefficients of the organic phase complexes was based on that of Soldenhoff *et al.* (2005) [50], assuming that the molecular volume of the extraction complex was 6 times larger than that of the D2EHPA monomer, as 6 D2EHPA molecules were required to extract 1 molecule of Zr or Hf. The estimated diffusion coefficients were in the same order of magnitude as those for Co-Ionquest 801 estimated by Soldenhoff *et al.* (2005) [50]. The shell-side coefficients were determined to be approximately 0.6% larger than the K_{OV} results reported in Figure 4-12 and Figure 4-13. This indicated that the shell-side resistance dominated the mass transfer for both Zr and Hf. The membrane and lumen

mass transfer coefficients were estimated to be approximately 8 and 22 times larger than K_{OV} , respectively, for both Zr and Hf.

The contributions of the shell, membrane, and lumen mass transfer resistances to the total overall resistance at a shell-side velocity of 0.41 cm.s^{-1} are illustrated in Figure 4-14. In Figure 4-14, it can be seen that the contributions of the lumen and membrane resistances to the total resistance were approximately 6 % and 15 % for both Zr and Hf, and that the overwhelming majority of the resistance (approximately 80 % and 78 %, respectively) was located in the shell. Therefore, moving forward, the modelling of the mass transfer behaviour focussed on the shell side. In addition, and based on the behaviour seen in Figure 4-12 and Figure 4-13, it was assumed that if the lumen velocity was maintained above 1.0 cm.s^{-1} , the effect of the lumen mass transfer coefficient on K_{OV} would be negligible. As the membrane resistance was constant, regardless of the velocities of either phase, while also estimated to be approximately an order of magnitude larger than K_{OV} , it was also regarded as negligible.

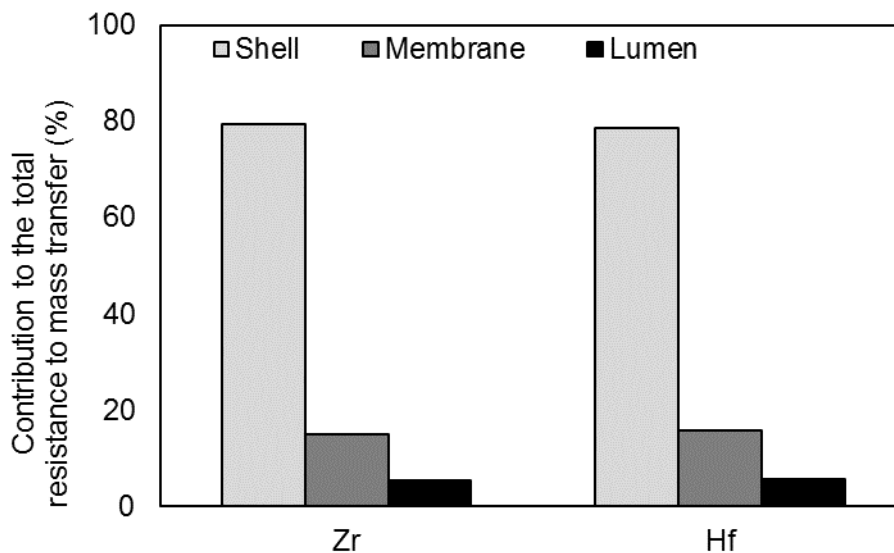


Figure 4-14: The relative contributions of the shell, membrane, and lumen to the total resistance to mass transfer of Zr and Hf. $U_{\text{Shell}} = 4.1 \times 10^{-3} \text{ m.s}^{-1}$

In Figure 4-15 and Figure 4-16, the shell side mass transfer coefficient data were compared to the correlations listed in Table 2-4 for Zr and Hf respectively. The relations proposed by Wakao and Kaguei (1985) and Gawronski & Wrzesinska (2000) overestimated the coefficients (both Zr and Hf) by nearly 100-fold and 10-fold, respectively, and were therefore not illustrated.

Table 4-1: The parameter values used to determine the individual mass transfer coefficients.

Description	Modelling parameters			
	Unit	Shell	Membrane	Lumen
Zr mass transfer coefficient	m.s ⁻¹	-	7.4 x10 ⁻⁷	2.0 x10 ⁻⁶
Hf mass transfer coefficient	m.s ⁻¹	-	7.2 x10 ⁻⁷	2.0 x10 ⁻⁶
Zr diffusion coefficient ¹	m ² .s ⁻¹	1.4 x10 ⁻⁹	1.8 x10 ⁻¹⁰	1.8 x10 ⁻¹⁰
Hf diffusion coefficient ¹	m ² .s ⁻¹	1.5 x10 ⁻⁹	1.7 x10 ⁻¹⁰	1.7 x10 ⁻¹⁰
Solution density ²	kg.m ⁻³	1050	-	851
Solution viscosity ³	Pa.s	2.0 x10 ⁻³	-	2.0 x10 ⁻³
Hydraulic diameter ⁴	m	3.6 x10 ⁻⁴	-	2.2 x10 ⁻⁴
Thickness ⁵	m	-	4.0 x10 ⁻⁵	-
Porosity ⁵	%	-	40	-
Tortuosity ⁵	-	-	2.4	-
Length ⁵	m	-	-	0.4
Zr Schmidt number	-	1 365	13 698	13 698
Hf Schmidt number	-	1 277	14 049	14 049
Zr partition coefficient ²	-	-	20.7	20.7
Hf partition coefficient ²	-	-	158	158

¹ Estimated with Wilke-Chang equation, Eq 2-17, [18,20,32,35,58,64,67].

² Data obtained experimentally.

³ Relation by Koekemoer *et al.* (2005) [69].

⁴ Relation by Baudot *et al.* (2001) [19].

⁵ As per supplier information [72,77,78].

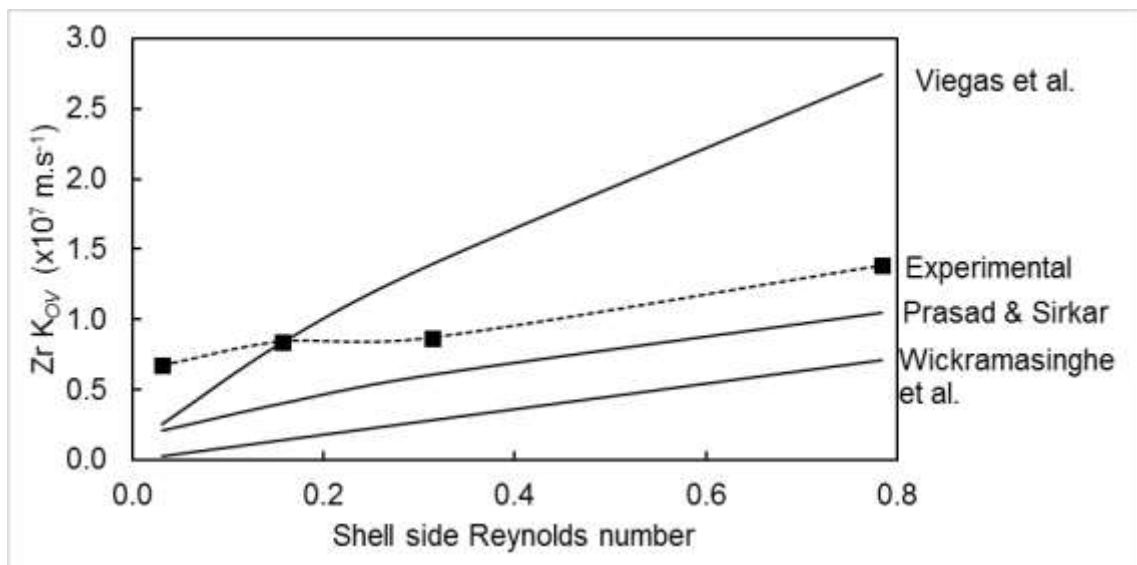


Figure 4-15: Comparison of shell-side Sherwood relations from literature to the experimental Zr data.

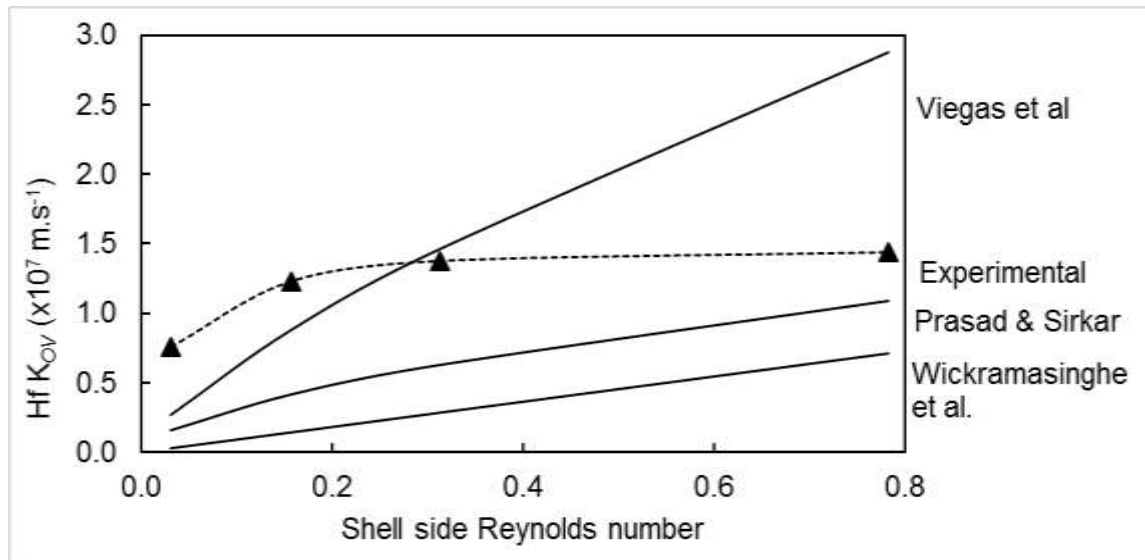


Figure 4-16: Comparison of shell-side Sherwood relations from literature to the experimental Hf data.

While the other relations also exhibited poor matches to the experimental data, they did predict values within the correct order of magnitude. The poor correlation between literature based models and experimental data has also been discussed by Gawronski & Wrzesinska (2000), who reported that Sherwood relations available in literature generally provide poor matches when applied to modules with high fibre packing factors [31]. It is also likely that the geometry of the membrane modules used by the various authors differed both from one another and from what was used in this study, resulting in the poor predictions when published relations are applied to other geometries, such as in this study where a module with a higher fibre packing factor was used. The deformation of the membrane fibres and the poor shell-side fluid distribution, as discussed under the general observations in Section 4.3, likely also had a significant impact on the surface area that was utilised for mass transfer, which in turn affected the accuracy of the literature relations. Because of the poor comparisons, an empirical Sherwood relation of the form given in Eq. 4-3 was fit to the experimental data.

$$Sh = \alpha Re^\beta Sc^{0.33} \quad 4-3$$

It is common for the Schmidt number to be raised to the power of 0.33, as can be seen in Table 2-4, and this was kept unchanged in the present study for both the Zr and Hf relations. The parameters α and β in Eq. 4-3 were used to fit the experimental data.

The parameters were solved by equating the experimental and modelled mass fluxes according to Eqs. 4-4 and 4-5 respectively:

$$j_{experimental} = \frac{\dot{Q}_{Shell}}{A_{mem}} (C_{in} - C_{out})_{Shell} \quad 4-4$$

$$j_{calculated} = \alpha Re^\beta Sc^{0.33} \left(\frac{D_{AB}}{d_H} \right) \Delta C_{LM} \quad 4-5$$

Initial values for α and β were estimated as 0.01 and 0.3, respectively. The experimental and calculated mass fluxes for each of the four shell-side experiments were determined and an objective function, Eq. 4-6, was used to determine the sum of errors between each of the four shell-side data points.

$$Error = \sum (j_{experimental} - j_{calculated})^2 \quad 4-6$$

Eq. 4-6 was minimised using the solver functionality of Microsoft® Excel and the final Sherwood relations, with the solved-for values of α and β , for Zr and Hf, are given in Eqs. 4-7 and 4-8 respectively.

$$Sh_{Zr} = 0.0034Re^{0.28}Sc^{0.33} \quad 4-7$$

$$Sh_{Hf} = 0.0036Re^{0.16}Sc^{0.33} \quad 4-8$$

Parity plots of the experimental and calculated mass fluxes for Zr and Hf are illustrated in Figure 4-17 and Figure 4-18, respectively, with the dotted lines indicating the ideal $y = x$ match. It can be seen that the fitted relations were able to predict the experimental data well, with the maximum deviations between the experimental and calculated values for the Zr relation approximately 20%, while that of the Hf relation was 16%. The average difference for both relations was approximately 10%. Bocquet *et al.* (2005) modelled the MBSX mass transfer of sulphur compounds from an aqueous solution into hexane and reported that the deviations between the simulated and experimental data were between 0.8 and 15% at low concentrations (5 ppm) of the sulphur compounds and between 30 and 60% when the concentrations were increased to 20 ppm [53]. Therefore, the observed deviations of Eqs. 4-7 and 4-8 were regarded as small enough that the relations would provide reliable predictions of K_{OV} for both Zr and Hf, and that they could be used for the purposes of upscaling to an industrial estimation.

The relations given by Eqs. 4-7 and 4-8 provide a vital part of the process model to predict the technical feasibility of MBSX to the industrial separation of Zr and Hf using the D2EHPA- H_2SO_4 chemistry. The LLE data and the Sherwood relations obtained in this chapter complete the first two objectives of this study as specified in Section 1.3, namely, knowledge of the partition coefficients and the effect of velocity on the mass transfer, respectively. The partition coefficient data that were gathered in this chapter, as well as the Sherwood relations, were used in the following chapter to create the industrial-scale estimations.

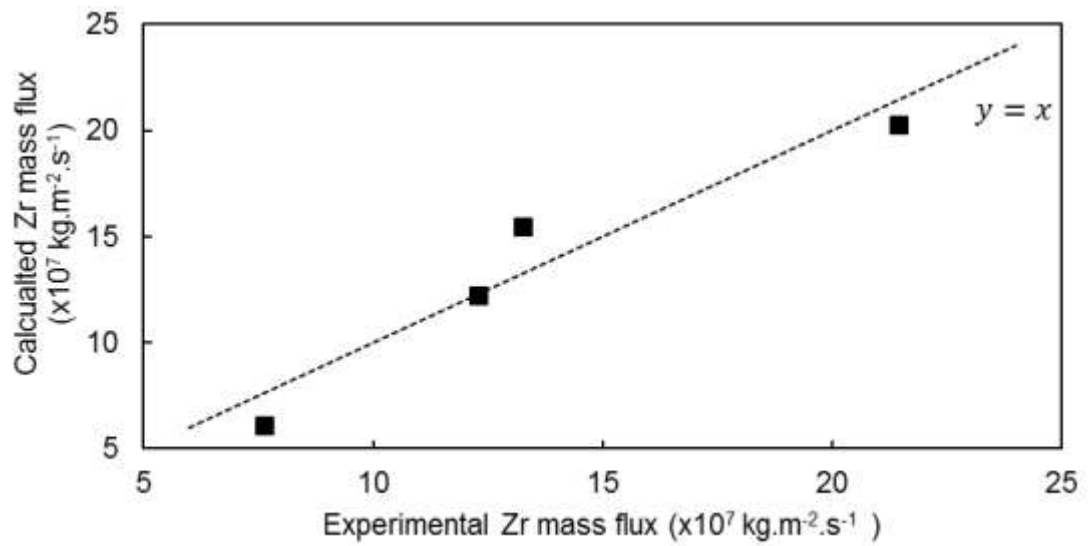


Figure 4-17: Experimental vs. calculated Zr mass flux values for fitting of the Sherwood relation.

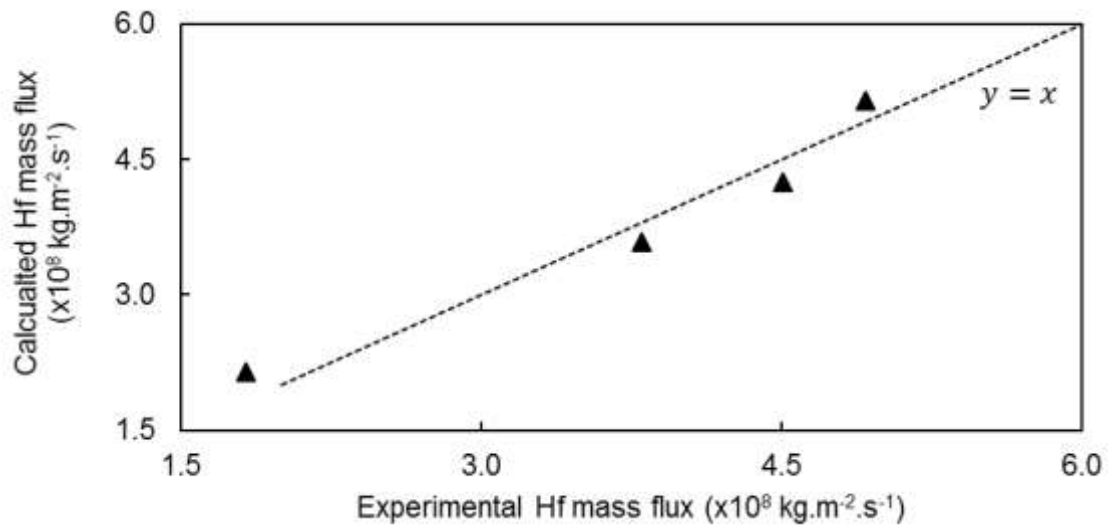


Figure 4-18: Experimental vs. calculated Hf mass flux values for fitting of the Sherwood relation.

5 Design of an industrial MBSX unit

5.1 Introduction

In this chapter, a design methodology is presented for estimating the membrane configuration of an industrial-scale Zr-Hf separation unit using MBSX. The design is based on a combination of the data generated and discussed in the Chapter 4, as well as information gathered from published literature. The final three objectives, as discussed in Section 1.3, are addressed in this chapter. These are: i) to propose a process model predicting the separation efficiency of an MBSX unit, ii) to estimate the required surface area for an industrial scale unit, and iii) to determine the series and parallel configuration of the membrane modules.

The design specifications for the process and the membrane module are discussed in Section 5.2 and 5.3 respectively. This is followed by the development of the process model in Section 5.4, and the methodology that was used to solve the model in Section 5.5. Finally, the estimations that were made are discussed in Section 5.6.

Three parameters needed to be determined for an industrial estimation to be made, namely: i) the minimum Hf content that could be attained in the outlet of the shell-side, ii) the Zr recovery at the point of minimum Hf content, and iii) the module configuration (number of modules in series and parallel) of the MBSX unit.

5.2 Design specifications

The shell-side production rate and product purity were set as the design specifications. The production rate (shell-side outlet) was set to $100 \text{ kg}\cdot\text{hr}^{-1}$ Zr, while the purity target of the same stream was limited to a maximum Hf content of 100 parts Hf per 1 million parts Zr (0.01% Hf). The production rate was based on converting approximately 1% of the Zr metal contained in the total ZrSiO_4 production of South Africa in 2016 to nuclear grade purity. The nuclear-grade purity specification of 0.01% Hf was based on values commonly described in literature [6,24,28,44].

The aqueous and organic phase compositions were maintained as that of the MBSX experiments, as reported in Sections 3.3.1.1 and 3.3.1.2 respectively. The shell-side phase consisted of $16 \text{ kg}\cdot\text{m}^{-3}$ Zr, $0.36 \text{ kg}\cdot\text{m}^{-3}$ Hf, and $98 \text{ kg}\cdot\text{m}^{-3}$ H_2SO_4 , while the lumen-side consisted of $235 \text{ kg}\cdot\text{m}^{-3}$ D2EHPA, and $41 \text{ kg}\cdot\text{m}^{-3}$ 1-octanol in Shelsol 2325.

5.3 Membrane module specifications

The Liqui-Cel™ 1.7x8.75 Minimodules used for the experimental portion of this study were suitable for the low volumetric flow rates that were investigated experimentally, but for an industrial-scale unit it would not be sensible to use many Minimodules rather than fewer, larger

modules that were designed for such operations. Therefore, the Liqui-Cel™ EXF-8x20 industrial series membrane contactor was selected as a suitable candidate for the MBSX unit. The Minimodules have a membrane surface area to volume ratio of approximately 1070 m².m⁻³ while that of the EXF modules is approximately 2100 m².m⁻³, indicating that the larger membrane modules are more space efficient, and possibly also more cost effective. The module and membrane specifications are provided in Table 5-1. The majority of the specifications were taken from the data sheet, while the number of fibres and the total surface area of the module were obtained from correspondence with a third party representative of 3M™ [79]. The module construction follows the centre-baffled pattern as discussed in Section 2.4.2, which improves the flow distribution of liquid in the shell by having the shell side feed flow through a central tube, i.e. across the membranes rather than along them. No specifications of the XIND fibre used in the module could be found, and as such, the fibre ID was estimated based on the total surface area and number of fibres while the membrane porosity, tortuosity, and thickness were assumed to be the same as that of the Minimodules, as listed in Table 4-1.

Table 5-1: Liqui-Cel™ EXF 8x20 hollow fibre membrane module specifications [79].

Module specifications			Membrane specifications		
Parameter	Value	Unit	Parameter	Value	Units
Shell OD	219	mm	Surface Area ²	53	m ²
Shell ID ¹	209	mm	Fibre ID ¹	180	µm
Overall length	610	mm	Fibre OD ¹	260	µm
Shell priming volume	6.7	L	Thickness ¹	40	µm
Lumen priming volume	5.2	L	Fibre length ¹	580	mm
Liquid flow guideline	1 - 11	m ³ .h ⁻¹	Approx. fibre count ²	161 000	-

¹ Assumed value.

² Obtained from correspondence [79].

5.4 Model development

This section provides a brief discussion on the development of the mass balances that were used to estimate the concentration profiles of Zr and Hf along the surface of a hypothetical membrane column. The full discussion regarding the modelling of mass transfer in an MBSX process can be found in Section 2.6.

In the discussions of the MBSX experiments in Section 4.3 and 4.4 it was assumed that the concentration difference between the shell and lumen was constant throughout the length of the membrane column. This assumption does not hold for an industrial estimation, which requires a model capable of predicting the concentration profiles along the membrane. Therefore, a mass balance was created using a control volume over the membrane contactor (Figure 2-4).

The mass balance was simplified by the following assumptions:

- Steady state operation with no solute accumulation in the membrane [17,19,33,53,54].
- Constant fluid properties and isothermal conditions [19,33,54].
- The reaction kinetics are fast and at equilibrium on the aqueous-organic interface [17,19,33,50,53].
- Both Zr and Hf exhibit constant partition coefficients throughout the column.
- The mass transfer coefficients remain constant along the length of the membrane [19].
- Both fluids are completely immiscible with no convective transport through the membrane [17,53].
- Mass transfer through the membrane is by diffusion only, and described by Fick's law.
- The membrane surface area is the same as the data provided by the manufacturer.
- The hydrodynamic relations of the Minimodules apply to EXF 8x20 module and the same fibres are used in both modules.
- The membrane properties of the Minimodules and EXF 8x20 module are the same.
- There are no effects from a pressure drop.

The control volume, originally illustrated in Figure 2-4, was adapted to describe the shell and lumen mass balances on either side of the membrane, and is here illustrated in Figure 5-1:

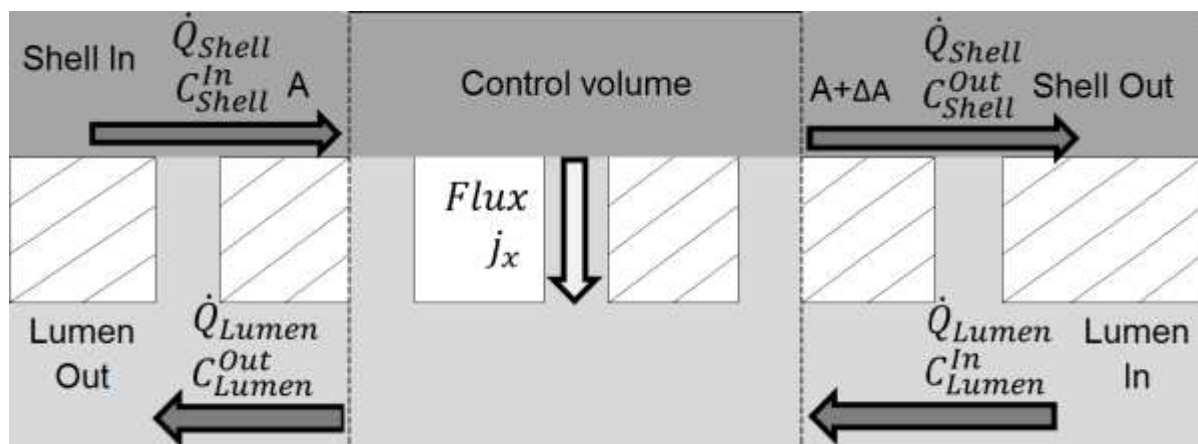


Figure 5-1: The control volume created over a portion of the membrane contactor for the mass balance.

Under conditions of constant fluid properties and steady state operation, the change in the concentration of solute on either side of the membrane was equal to the mass flux through the membrane, as described by Eq. 2-6. The lumen-side equation was similar, when the left-side terms were replaced by the corresponding lumen terms.

$$\dot{Q}_S C_S|_A - \dot{Q}_S C_S|_{A+\Delta A} = j_x A_{mem} \quad 2-6$$

Letting $\Delta A \rightarrow 0$, Eq. 2-6 was written in differential form:

$$\frac{dC_S}{dA_{mem}} = \frac{j_x}{\dot{Q}_S} \quad 2-7$$

Eq. 2-7 represents the shell-side design equation that was used to determine the concentration profiles of Zr and Hf. The lumen-side equation followed similarly. The mass flux, assuming that the reaction kinetics were fast relative to diffusion and did not affect the rate of mass transfer, was estimated using Fick's law and written in terms of K_{OV} as:

$$j_x = K_{OV} \left(C_S - \frac{C_L}{P} \right) \quad 2-9$$

With K_{OV} :

$$\frac{1}{K_{OV}} = \frac{1}{k_{shell}} + \frac{d_{OD}}{Pk_{Mem}d_{LM}} + \frac{d_{OD}}{Pk_{Lumen}d_{ID}} \quad 2-11$$

Based on the results discussed in Section 4.4.2, where it was shown that the resistance of the shell-side dominated the mass transfer, the K_{OV} values used in this chapter were approximated well by the Sherwood relations given by Eqs. 4-7 and 4-8.

$$Sh_{Zr} = 0.0034Re^{0.28}Sc^{0.33} \quad 4-7$$

$$Sh_{Hf} = 0.0036Re^{0.16}Sc^{0.33} \quad 4-8$$

5.5 Model application

The design equation (Eq. 2-7) was solved according to the algorithm depicted in Figure 5-2. The design equation predicts the behaviour of a single membrane column which was replicated to create parallel operating membrane columns as many times as required to reach the production target specified in Section 5.2.

Note that this section uses the subscripts '*single*' and '*total*'. The '*single*' subscript refers to a parameter of one single membrane column, while the '*total*' subscript refers to the parameter for all the parallel membrane columns combined.

5.5.1 Initial values

The initial values, as illustrated in Figure 5-2, that were required as model inputs included the total surface area of the membrane column (*i.e.* the end point of the integral), the shell-side inlet concentrations (as specified in Section 5.2), the shell and lumen velocities, the lumen-side outlet concentrations, and the mass transfer coefficients.

- The end point of the integral (A_{mem}) was chosen as a random value larger than 1.
- The shell-side inlet concentrations were used as specified in Section 5.2.

- The shell velocities were selected to correspond to Reynolds numbers near the lower and upper end of the experimental ranges as well as the velocity corresponding to the maximum design flow rates.
- The lumen velocity was determined according to two constraints: i) a minimum lumen Reynolds number of 0.7, and ii) an organic to aqueous (O:A) ratio of at least 2:1 had to be maintained at all times. As discussed in Section 4.4.2, a lumen Reynolds number of 0.61 (velocity of 0.81 cm.s⁻¹ in the Liqui-Cel™ EXF-8x20 membrane module) or higher indicated that the contribution of the lumen resistance to the overall resistance to mass transfer would be negligible. Further, the maximum metal concentration in the lumen that could be achieved with the given D2EHPA concentration was approximately 10 kg.m⁻³, thus an O:A ratio of at least 2:1 was specified to prevent saturation of the organic phase and ensure that a driving force for extraction could be maintained. For the minimum O:A ratio of 2:1, the lumen velocity was determined using Eq. 5-1:

$$U_{Lumen} = \frac{2U_{Shell-single}Ac_{Shell-single}}{Ac_{Lumen-single}} \quad 5-1$$

If U_{Lumen} was less than 0.92 cm.s⁻¹, the lumen velocity was set to 0.92 cm.s⁻¹ to reach the minimum Reynolds number of 0.7 (with an O:A ratio larger than 2:1 in such cases).

- The counter-current flow of the lumen meant that the lumen-side concentrations were calculated in reverse from the lumen outlet back to the inlet. Therefore, the initial value of the lumen concentrations (at $A_{mem} = 0$) represented the outlet concentrations, and for the first iteration, were estimated as half that of the inlet shell-side concentration.
- The mass transfer coefficients were estimated using Eqs. 4-7 and 4-8 based on the shell-side velocity. The shell velocities were selected such that the shell-side Reynolds numbers in the industrial estimation were similar to that of the MBSX experiments (Section 4.3) in order to maintain the accuracy of the Sherwood relations as much as possible.

5.5.2 Application of the algorithm

The following discussion follows the algorithm depicted in Figure 5-2 from the top downwards. Polymath™ 6.0 ODE solver software was used to solve the design equation (Eq. 2-7).

For the initial values input to the algorithm it was common for the lumen concentrations at the end of the column (at $A_{mem} = final$) to be reported as negative. These values represented the lumen-side concentrations entering the column and under normal operating conditions would be expected to be zero. The negative values were corrected by increasing the initial value of the lumen concentration (measured at $A_{Mem} = 0$) until the values (measured at $A_{Mem} = final$) were positive and less than 1% of the outlet concentration. An inlet concentration of 1% of the outlet concentration was considered sufficient for the purpose of this study.

Once the inlet lumen concentrations met the stipulated criteria, the $Hf:Zr_{final}$ ratio of the shell-side was evaluated and the surface area (A_{mem}^{final}) adjusted according to the criteria as per Figure 5-2. The value of A_{mem}^{final} was increased until $Hf:Zr_{final} > Hf:Zr_{minimum}$, after which A_{mem}^{final} was decreased until $Hf:Zr_{final} = Hf:Zr_{minimum}$. At this point the loop was terminated and the values for A_{mem}^{final} , the Zr recovery (Zr remaining in the shell-side product stream), and $Hf:Zr_{final}$ were extracted and used to determine the design flow rates of the shell and lumen, and the configuration of the membrane modules.

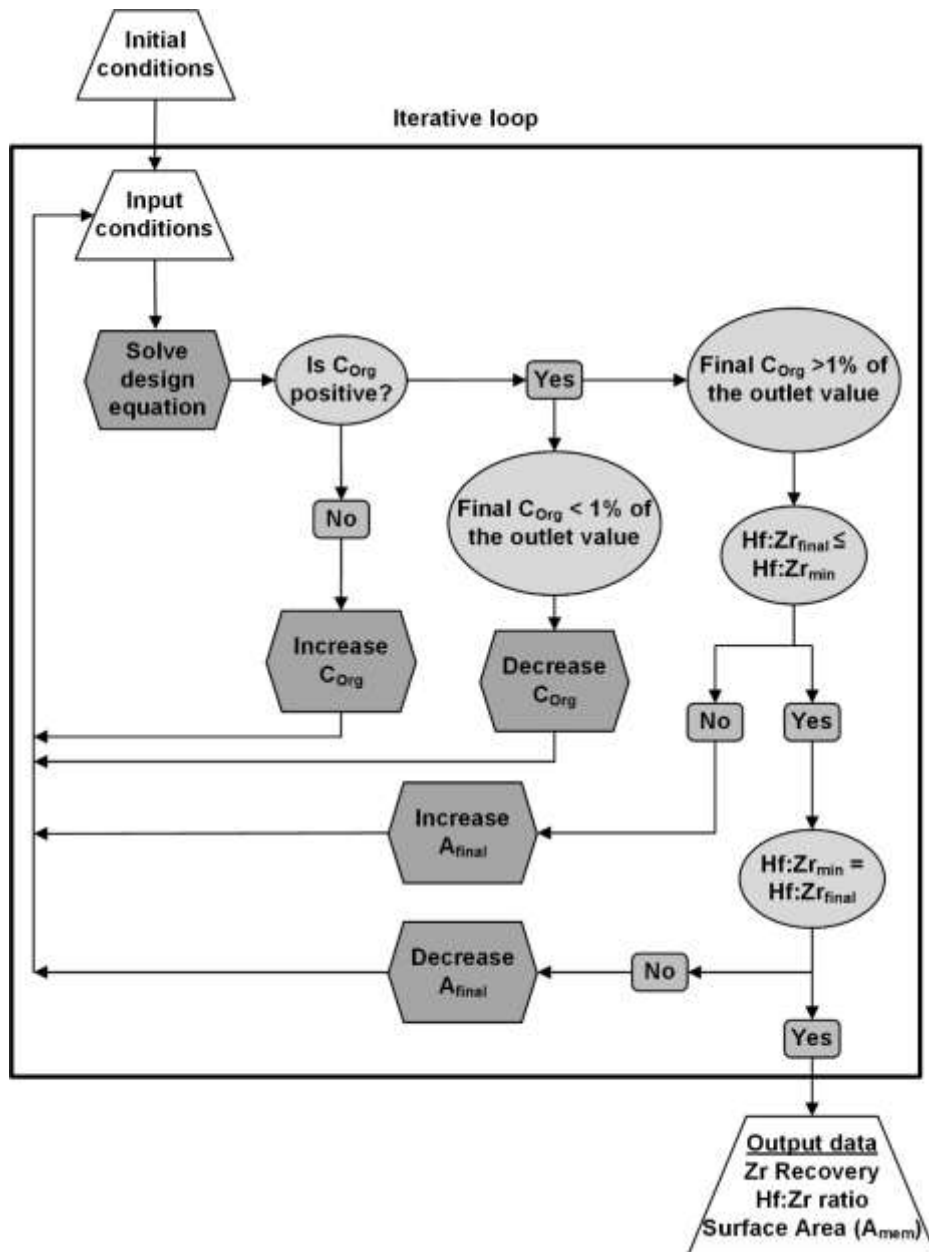


Figure 5-2: Design equation algorithm. In the figure, the trapezoids indicate variables, the ovals indicate criteria for certain variables, the rounded rectangles indicate the outcome of the criteria, and the hexagons indicate the relevant action that needs to be taken based on the outcome of the criteria.

5.5.3 MBSX unit configuration

The data gathered for a single membrane column from the design algorithm in the previous Section (5.5.2) was used to determine following: i) the total input flow rate of the shell (Eq. 5-2), ii) the number of parallel membrane columns (Eq. 5-4), iii) the number of modules in series (Eq. 5-5), and iv) the total lumen input flow rate.

The total volumetric flow rate required to reach the production target of 100 kg.hr⁻¹ Zr was determined using the recovery of Zr as in Eq. 5-2:

$$\dot{Q}_{Shell-total} = \frac{Production\ target}{(Inlet\ Zr\ concentration)(Recovery\ of\ Zr)} \quad 5-2$$

With the total volumetric flow rate and the specified shell velocity known, the total shell-side cross-sectional area (Eq. 5-3) was determined. The shell-side velocity was assumed to be constant in every parallel membrane column.

$$Ac_{Shell-total} = \frac{\dot{Q}_{Shell-total}}{U_{Shell}} \quad 5-3$$

The number of parallel membrane columns ($N_{Parallel}$) was calculated using Eq. 5-4, by dividing the total shell-side cross-section by the shell-side cross-section of a single membrane contactor:

$$N_{Parallel} = \frac{Ac_{Shell-total}}{Ac_{Shell-single}} \quad 5-4$$

The number of modules connected in series were determined by dividing the final surface area as determined in Section 5.5.2 by the surface area of a single module:

$$N_{Series} = \frac{A_{Mem}^{final}}{A_{Module-single}} \quad 5-5$$

The last parameter, the total lumen flow rate, was determined using Eq. 5-6:

$$\dot{Q}_{Lumen-total} = U_{Lumen-single} A_{Lumen-single} N_{Parallel} \quad 5-6$$

The input flow rates ($\dot{Q}_{Shell-total}$ and $\dot{Q}_{Lumen-total}$) and the configuration of the membrane modules ($N_{Parallel}$ and N_{Series}) represent the design parameters used for the industrial estimations.

5.6 Modelling results

The assessment methodology was demonstrated by evaluating four industrial-scale separation cases. The first and second cases represented shell-side Reynolds numbers corresponding to the lower and upper experimental ranges, respectively. The third estimation corresponded to the flow rate, where $\frac{K_{Hf}}{K_{Zr}} \approx 1$, thus the maximum shell-side velocity at which Hf is still preferentially extracted. The final estimation represented a purely hypothetical scenario where the LLE separation factor was achieved at the same velocity as the third estimation. The data for these cases are listed in Table 5-2.

From the data listed in Table 5-2 it can be seen that the first three cases (lower Re, upper Re, and max flow) were not able to achieve the $Hf:Zr_{final}$ purity specification of 100 ppm, due to the low separation ratio between Zr and Hf, which resulted in significant co-extraction of Zr into the lumen. Simply achieving the minimum Hf content in the feed stream would require combining membrane surface areas in the order of trillions of square meters. The high extraction of both Zr and Hf can be seen in the lumen-side outlet concentrations, and subsequently, the lumen flow rates. Such flow rates are excessively high and would be impractical for the proposed cases. In the lower Re, upper Re, and max flow cases the mass flow rate of Zr in the lumen outlet stream exceeded that of the shell-side outlet stream. The low recovery of Zr in the shell-side outlet stream also meant that, in order for the production target of $100 \text{ kg}\cdot\text{hr}^{-1}$ Zr to be reached, the annual production of zircon by South Africa would need to at least double in the case of the lowest Re estimation, or more for the other two cases.

Table 5-2: Summary of the industrial-scale cases. Bold values represent the values that were used as inputs to the algorithm.

Parameter Group	Parameter	Estimation identifier			
		Lower Re	Upper Re	Max flow	Ideal
U (m.s ⁻¹)	Shell	1.0 x10⁻⁴	1.0 x10⁻³	5.0 x10⁻³	4.8 x10⁻²
	Lumen	1.0 x10⁻²	1.8 x10⁻²	9.2 x10⁻²	8.8 x10⁻²
\dot{Q} (m ³ .hr ⁻¹)	Shell (Aq)	45 290	698 090	317 549	14
	Lumen (Org)	494 832	1 396 180	635 098	30
	O:A ratio	10.9	2.0	2.0	2.1
C_{out} (kg.m ⁻³)	Shell Zr	2.2 x10 ⁻³	1.4 x10 ⁻⁴	3.1 x10 ⁻⁴	6.9
	Shell Hf	3.7 x10 ⁻⁷	2.4 x10 ⁻⁷	9.1 x10 ⁻⁷	6.4 x10 ⁻⁴
	Lumen Zr	1.47	8.0	8.0	4.6
	Lumen Hf	0.033	0.18	0.18	0.18
Outlet mass flow rates (kg.hr ⁻¹)	Shell Zr	100	100	100	100
	Shell Hf	0.02	0.17	0.29	0.01
	Lumen Zr	7.3 x10 ⁵	1.1 x10 ⁷	5.1 x10 ⁵	137.7
	Lumen Hf	1.63 x10 ⁴	2.5 x10 ⁵	1.1 x10 ⁴	5.39
K_{OV} (x10 ⁸ m.s ⁻¹)	Zr	1.6	3.1	4.8	4.8
	Hf	2.6	3.7	4.8	36
Separation ratio		1.6	1.2	1.0	7.5
Algorithm outputs	Shell Hf:Zr (ppm)	168	1682	2905	92
	Zr recovery (%)	0.01	0.001	0.01	42.14
Configuration	$A_{C_{shell-total}}$ (m ²)	1.3 x10 ⁻⁵	193 914	18 377	0.8
	A_{mem}^{final} (m ²)	2 100	14 800	79 000	3 200
	$N_{Parallel}$	3 339 799	5 147 909	487 853	23
	N_{Series}	40	280	1 491	61
	Total Surface Area (m ²)	7.1 x10 ⁹	7.64 x10 ¹⁰	3.9 x10 ⁹	7.4 x10 ⁴

The reason for the increased surface area (A_{mem}^{final}) required for a single column to reach the minimum Hf: Zr_{final} ratio with increasing velocity, was that while the mass flux increased slightly at higher velocities as a result of increased mass transfer coefficients, the mass flow rate increased significantly. Therefore, the membrane flux represented a smaller portion of the total mass transfer thus requiring longer columns to achieve the minimum Hf: Zr_{final} ratio. The apparent reduction in the extraction efficiency meant that higher shell-side velocities would require longer columns despite increased rates of transmembrane mass flux. Longer columns present a design concern, especially when combined with higher fluid velocity, as the increased

pressure drop would add not only additional components (such as the possible inclusion of a network of pumps between membrane modules) but also make it more difficult to maintain the required transmembrane pressure to prevent breakthrough of the wetting phase into the non-wetting phase. On the other hand, an increase in the shell-side velocity exhibited a decrease in the number of membrane columns that were required to be used in parallel to reach the desired production target. It is therefore imperative that during the design of an MBSX unit the configuration of the number of membrane modules connected in series and the number of parallel operating membrane columns needs to be carefully considered for optimal performance.

The final estimation listed in Table 5-2 was created as an ideal case in which the LLE separation factor of ??? was achieved. The Zr K_{OV} value was estimated using Eq. 4-7 for the same shell-side velocity as the Max Flow estimation and then multiplied by 7.5 to determine the on the K_{OV} of Hf. The final surface area that would be required to achieve the specified 100 parts Hf per 1 million parts Zr was estimated at approximately 74 000 m², while approximately 42% of the Zr in the feed stream was recovered as nuclear grade purity. Reaching the production target of 100 kg.hr⁻¹ Zr would require 23 membrane columns operating in parallel, with 61 modules connected end to end, therefore a total of 1403 Liqui-Cel™ EXF-8x20 modules with a combined membrane surface area of approximately 74 360 m².

From the difference between the max flow and ideal cases, it was concluded that, the main problem which resulted in the industrial cases requiring approximately a trillion square meters of membrane surface area was the low separation ratio caused by the dominant, and non-selective shell-side resistance to mass transfer. The non-selective mass transport resulted in not only low overall mass fluxes for both metals, but also the low separation ratio. Subsequently, the significant co-extraction of Zr decreased the recovery of Zr, while preventing the purity specification from being achieved. The low mass flux required long columns to effectively extract Zr and Hf. On the other hand, in the ideal case, the high predicted separation ratio, alongside the increased K_{OV} values, ensured that an industrial-scale MBSX would meet both the production and purity specifications as described in Section 5.2.

From the results of the cases that were predicted in this section, it became evident that the values for K_{OV} as well as the separation ratio were vital parameters that determined the feasibility of an industrial-scale MBSX unit. It is critical to the success of an MBSX process that these parameters must be carefully investigated and accurately predicted, as it was shown that the LLE data could not be used on its own as a possible predictor of the success of an MBSX process.

6 Conclusions and recommendations

6.1 Conclusions

In this study, the separation of Hf from Zr using the D2EHPA-H₂SO₄ system in a membrane contactor was investigated as a case study for the purpose of developing an approach that could be used to predict the suitability of MBSX for industrial applications. For the development of this approach, knowledge of i) the partition coefficients for Zr and Hf, ii) the influence of the shell and lumen velocities on K_{OV} of Zr and Hf, iii) a process model capable of estimating the separation efficiency of an industrial-scale MBSX unit, and iv) a design methodology to determine the parallel and series configuration of the membrane modules, was required.

6.1.1 LLE

The high feed concentration utilised required that a suitable D2EHPA concentration in the organic phase and the partition coefficients be determined by LLE. The highest separation factor that was observed to be 7.5 at an E:M ratio of 4.1:1, or 235 g.L⁻¹ D2EHPA. The the separation factor decreased at higher D2EHPA concentrations, and therefore, 235 g.L⁻¹ D2EHPA was used for the MBSX experiments. The corresponding partition coefficients of Zr and Hf, at this D2EHPA concentration, were 21 and 156, respectively.

6.1.2 MBSX

The effect of both the shell-side and lumen-side velocities on the overall mass transfer coefficients of Zr and Hf were investigated. From the results obtained, it became apparent that the lumen velocity only had a small influence on the shell-side outlet concentrations. Furthermore, the mass transfer coefficients of Hf ($1.7 \times 10^{-7} \text{ m.s}^{-1}$) seemed to reach a plateau at lumen velocities exceeding 0.67 cm.s^{-1} ($Re_{Lumen} = 0.61$), while that of Zr appeared to increase throughout the whole range from 4.4×10^{-8} to $1.2 \times 10^{-7} \text{ m.s}^{-1}$, although also showing a possible plateauing trend. At velocities above 0.67 cm.s^{-1} , the contribution of the lumen resistance to the total resistance to mass transfer could be considered minimal for both Zr and Hf. The shell-side velocity had a strongly negative influence on the apparent extraction efficiency. The increased mass flow rate resulting from the increased volumetric flow rate overshadowed the increased rate of mass flux resulting in concentration gradients over the column of less than 5% at the highest shell-side velocity tested. The highest separation ratio (1.7) between Hf and Zr was recorded at an O:A volumetric flow ratio of 1:1. The generally low separation was attributed to the non-selective, diffusion-based nature of the dominant shell-side resistance. It is suspected that even with a higher LLE separation factor the results from the MBSX experiments would exhibit a similar separation ratio under the conditions of this study. The separation ratio of MBSX (1.6) was found

similar to that of the CESUZ process (1.7). Between the two methods, the need for corrosion resistant alloys and special molten salt handling technology might make MBSX preferable.

It was evident that under the conditions used in this study that the LLE experimental data alone could not be used to estimate the feasibility of a chemical system for MBSX application and that mass transfer experiments are vital in predicting the feasibility of an MBSX separation process.

The once-through methodology used in the present study allowed a simple and easy approximation of steady state, with constant, known feed compositions, but required large volumes of chemical reagents, which in addition to the low extraction efficiency at higher shell-side velocities, and the measurement detection limits, limited the number of useful experiments that could be done.

The modules used in this study were originally developed for a gas phase in the shell, and hence they were found to not be ideally suited for MBSX. The observable spacing between the membranes were small and the swelling and deformation of the membrane fibres that was observed during the contact between the membrane fibres and the organic phase further restricted the shell-side flow. The deformation caused the fibre bundle to buckle, creating large channels around the outside of the bundle through which the shell-side fluid bypassed significant portions of the aqueous-organic interfacial area. The discrepancy between the nominal surface area and the utilized surface area likely resulted in underestimated mass transfer coefficients.

6.1.3 Mass transfer modelling

It was found that the shell-side resistance dominated the mass transfer for all the MBSX experiments contributing approximately 80 % for Zr and 78 % for Hf of the total mass transfer resistance. The literature relations to predict the shell-side mass transfer coefficients provided poor matches to experimental data, which was attributed to varying geometries between the membrane modules that were likely used by different authors. However, the fitted Sherwood relations predicted the experimental mass transfer with sufficient accuracy that, despite the likely underestimation, an industrial-scale estimation could be made.

6.1.4 Industrial estimation

A mass balance based differential design equation was used to predict the concentrations of Zr and Hf along the surface of a membrane column. A methodology to estimate an MBSX process unit capable of meeting specifications such as a production rate and product purity using the process model and Sherwood relations was also developed.

Under the tested experimental conditions, it became apparent that it would not be possible to achieve the product purity specification of 100 parts Hf per 1 million parts Zr. This was ascribed to the low separation ratio attained using the specific module and experimental conditions. In all

of these scenarios the recovery of Zr was consistently below 0.1%, making such a process unfeasible for industrial application.

To obtain further clarification, a hypothetical case, where the LLE separation factor of 7.5 was specified by artificially increasing K_{OV} of Hf, was subsequently evaluated. According to the results of this case, the specified shell-side production rate of 100 kg.hr⁻¹ Zr (at an estimated Zr recovery of 42%) and shell-side product purity of 92 ppm Hf could be achieved with 23 parallel operating membrane columns each consisting of 61 Liqui-Cel™ EXF-8x20 membrane modules connected in series, for an approximate total membrane surface area of 74 000 m².

It was thus demonstrated in this study that the data gathered and the approach that was developed could be used to predict the suitability of MBSX for an industrial-scale process. Given the cases based on the experimental data, the application of MBSX with the D2EHPA-H₂SO₄ system is not recommended for industrial application. However, if the separation ratio can be increased to approach that of the LLE data, even without significant increases to the K_{OV} values of this study, MBSX could be significantly more feasible for the industrial-scale separation of Hf from Zr.

The developed methodology did not only provide a prediction of the industrial suitability of MBSX, but also highlighted the critical parameters (overall mass transfer coefficients, and especially, the separation ratio) that need to be improved to attain a feasible industrial-scale process.

6.2 Recommendations

While the Hf-selective system used in this study is attractive as a minor component selective process, it is recommended that Zr-selective systems should also be investigated as the fitted Sherwood relations discussed in Section 4.4.2 clearly demonstrated that Zr benefitted greatly from an increased shell-side velocity. Despite the increased costs related to larger downstream (scrubbing and stripping) equipment of a Zr-selective chemical system, such a system might exhibit better separation characteristics than the D2EHPA-H₂SO₄ system used in this study if the non-selective mass transfer limitations of this study can be overcome.

In the present study, the generation of data for the purpose of developing an approach to estimate the suitability of MBSX was favoured above determining the optimal process conditions. Accordingly, the modelling of the process behaviour did not include the effects of: i) the reagent concentrations, ii) the pH, iii) the reaction kinetics, iv) the inlet flow conditions, v) the membrane fibre spacing or corrections for the bypassing experienced by the shell-side flow, vi) saturation of the organic phase, or, vii) the combination of scrubbing and stripping processes. While the data generated here served the purpose for the development of a methodology to assess the feasibility of MBSX for the industrial-scale separation of Hf from Zr well enough, the model that was developed is far from perfect and many improvements can be incorporated to improve its

accuracy. The suggested improvements can generally be divided into two groups, namely the chemistry, and the module. The chemistry group of variables include the reagent concentrations, pH, reaction kinetics, effects of saturation of the organic phase, and the scrubbing and stripping processes. During this study it was observed that the concentration values measured by the ICP-OES varied, despite the solutions being carefully prepared. It is strongly recommended that any investigations to optimise the chemistry incorporate better controls to reduce such variations and make comparing data sets simpler. The module group of variables include the inlet flow conditions, membrane fibre spacing, and correction factors for channelling and bypassing. It is recommended that each of the mentioned limitations of this study be investigated as all of these variables would certainly provide a refinement of this model.

The available funding of this study limited the number of experiments and variables that were investigated. While the single-variable method used in this study was sufficient for achieving the envisaged aim, a factorial design of experiments could be used to provide more information from a similar number of experiments.

The inclusion of membrane-based scrubbing and stripping processes of the organic phase would be expected to improve the overall separation and recovery of both Zr and Hf. While it is highly recommended that these processes should also be investigated, it is vital that these efforts must avoid a dominant non-selective resistance to mass transfer, as was found in the present study. If this can be achieved, the inclusion of the scrubbing and stripping of the loaded solvent in the approach that was proposed here would allow for a much more comprehensive evaluation of PX for the separation of Zr and Hf.

The swelling of the membrane fibres inside the modules were of particular concern as large channels formed in the shell due to buckling of the fibre bundle, enabling much of the membrane surface to be completely bypassed by the shell-side phase. Additionally, the swelling reduced the spacing between the fibres, further restricting the shell-side access to the aqueous-organic interface. Hence the low overall rates of mass transfer attained, were undoubtedly influenced by the significant bypassing of the shell-side. Therefore, it is imperative that modules must be designed to either accommodate swelling of the fibres or membrane materials which exhibit low swelling should be used. While the Liqui-Cell™ EXF modules with their cross-flow design provide a significant improvement over the simple parallel flow modules used in this study, modules designed for handling (less swelling and deformation) two liquid phases would greatly benefit the attractiveness of MBSX and PX processes for industrial applications.

During the study, all the membrane modules eventually failed with large fractures forming in the polycarbonate shell. Despite cleaning any remaining reagents after experiments, the damage highlighted the chemical incompatibility of the materials used and the evident importance of compatibility between the materials that are used in MBSX. The construction materials of the

modules (housing, flow dividers and membranes) therefore have to be carefully considered to ensure chemical compatibility. Ideally, the materials should be selected based on the specific applications, which in many PX systems would require a compatibility with both polar (aqueous) and non-polar (organic) phases with a high acid stability.

The large volumes of chemicals used and the low extraction values of the once-through methodology can be addressed using a circulating method, such as the circulating method used by Baudot et al. (2001). This is however, more useful at high flow rates as the differential extraction of a single pass through the membrane column can be accumulated until a concentration difference can be measured accurately. Additionally, the cost of reagents per experiment could likely be reduced.

In this study, the organic phase was not analysed due to the unavailability of suitable analytical techniques. To mitigate this limitation, the once-through method was used for the MBSX experiments. This did however limit the amount of experiments that could be conducted as well as performing a mass balance closure over the MBSX equipment. Therefore, it is recommended for future work to include an analysis of the organic phase to aid in the validation of the model assumptions and the extraction mass balance. Additionally, longer experiments utilising a recycle setup could be used to determine the membrane stability, the effects of repeated partial loading and unloading of the carrier as well as ion migration.

While membrane fouling was unlikely in the present study due to the lack of any undissolved particulates in the solutions, possible contaminants and filtration should be considered when upscaling for industrial applications. Based on the current absence of literature on the effects of fouling on MBSX, future studies on the possible mechanisms of membrane fouling and the long-term effects of fouling in MBSX systems should be considered.

7 References

1. Bradley DC, Thornton P. Zirconium and Hafnium. In: J.C. B, H.J. E, R. N, A.F. T-D, editors. *Comprehensive Inorganic Chemistry*. First. Pergamon Press; 1975. p. 253–4.
2. Royal society of chemistry. Zirconium [Internet]. *Encyclopædia Britannica*, inc. 2019 [cited 2019 Aug 29]. Available from: <https://www.britannica.com/science/zirconium>
3. Royal society of chemistry. Hafnium [Internet]. *Encyclopædia Britannica*, inc. 2019 [cited 2019 Aug 29]. Available from: <http://www.rsc.org/periodic-table/element/72/hafnium>
4. Yang XJ, Fane AG, Pin C. Separation of zirconium and hafnium using hollow fibres Part II. Membrane chromatography. *Chem Eng J*. 2002;88(1–3):45–51.
5. Cox RP, Peterson HC, Beyer GH. Separating Hafnium from Zirconium. *Ind Eng Chem Res* [Internet]. 1958;50(2):141–3. Available from: <http://libezp.nmsu.edu:2533/doi/pdf/10.1021/ie50578a022>
6. Banda R, Lee MS. Solvent Extraction for the Separation of Zr and Hf from Aqueous Solutions. *Sep Purif Rev* [Internet]. 2017;44(3):199–215. Available from: <http://dx.doi.org/10.1080/15422119.2014.920876>
7. Chen S, Zhang Z, Kuang S, Li Y, Huang X, Liao W. Separation of zirconium from hafnium in sulfate medium using solvent extraction with a new reagent BEAP. *Hydrometallurgy*. 2017;169(December 2016):607–11.
8. Xu L, Xiao Y, Van Sandwijk A, Xu Q, Yang Y. Production of nuclear grade zirconium: A review. *J Nucl Mater*. 2015;466:21–8.
9. Reddy BR, Kumar JR, Reddy A V. Solvent extraction of tetravalent hafnium from acidic chloride solutions using 2-ethyl hexyl phosphonic acid mono-2-ethyl hexyl ester (PC-88A). *Miner Eng*. 2004;17(4):553–6.
10. Brumbaugh RJ. Corrosion Resistance of Zirconium. Effect of Oxygen, Nitrogen, Carbon, and Hafnium. *Ind Eng Chem* [Internet]. 1951;43(12):2878–80. Available from: <http://pubs.acs.org/doi/abs/10.1021/ie50504a061>
11. Wang LY, Lee HY, Lee MS. Solvent Extraction of Zirconium and Hafnium from Hydrochloric Acid Solutions Using Acidic Organophosphorus Extractants and Their Mixtures with TOPO. *Mater Trans*. 2013;54(8):1460–6.
12. Xu Z, Wang L, Wu M, Xu Y, Chi R, Li P, et al. Hydrometallurgy Separation of zirconium and hafnium by solvent extraction using mixture of DIBK and P204. *Hydrometallurgy* [Internet]. 2016;165:275–81. Available from:

- <http://dx.doi.org/10.1016/j.hydromet.2016.01.032>
13. Banda R, Min SH, Lee MS. Selective extraction of Hf(IV) over Zr(IV) from aqueous H₂SO₄ solutions by solvent extraction with acidic organophosphorous based extractants. *J Chem Technol Biotechnol*. 2013;89(11):1712–9.
 14. Yang XJ, Fane AG, Pin C. Separation of zirconium and hafnium using hollow fibers: Part I. Supported liquid membranes. *Chem Eng J*. 2002;88(1–3):37–44.
 15. Amaral JCBS, Morais CA de. Study of Zirconium and Hafnium Separation by Solvent Extraction Technique from Nitric and Hydrochloric Solutions with Acid , Basic and Neutral Extractants. *World J Eng Technol*. 2016;4:138–50.
 16. Lee MS, Banda R, Min SH. Separation of Hf(IV)-Zr(IV) in H₂SO₄ solutions using solvent extraction with D2EHPA or Cyanex 272 at different reagent and metal ion concentrations. *Hydrometallurgy*. 2015;152:84–90.
 17. Gabelman A, Hwang S-T. Hollow fiber membrane contactors. *J Memb Sci* [Internet]. 1999;159(1–2):61–106. Available from:
<http://linkinghub.elsevier.com/retrieve/pii/S037673889900040X>
 18. Baudot A, Flourey J, Smorenburg HE. Liquid-liquid extraction of aroma compounds with hollow fiber contactor. *AIChE J*. 2001;47(8):1780–93.
 19. Dindore VY, Versteeg GF. Gas-liquid mass transfer in a cross-flow hollow fiber module: Analytical model and experimental validation. *Int J Heat Mass Transf*. 2005;48(16):3352–62.
 20. Schlosser Š, Sabolova E, Kertész R, Kubisova L. Factors influencing transport through liquid membranes and membrane based solvent extraction. *J Sep Sci*. 2001;(24):509–18.
 21. Schlosser S, Martak J. Separation of mixtures by pretraction or membrane-based solvent extraction and new extractants. *Membr Teor I Prakt*. 2009;123–52.
 22. Eykamp W, Mulder MHV, Strathmann H, Boyadzhiev L, Lazarova Z, Reed BW, et al. Membrane separations technology: Principles and applications [Internet]. First. Noble RD, Stern SA, editors. *Membrane Separations Technology - Principles and Applications*. Elsevier B.V.; 1995. 283–352 p. Available from:
<http://linkinghub.elsevier.com/retrieve/pii/S0009250996900391>
 23. Wang LY, Lee MS. Development of a separation process for the selective extraction of hafnium(IV) over zirconium(IV) from sulfuric acid solutions by using D2EHPA. *Hydrometallurgy* [Internet]. 2016;160:12–7. Available from:
<http://dx.doi.org/10.1016/j.hydromet.2015.11.013>

24. Reichl C, Schatz M, Masopust A, Resel W. WORLD MINING DATA 2018 [Internet]. Mineral Commodity Summaries. 2018. Available from: <http://pubs.er.usgs.gov/publication/70180197>
25. Blumenthal WB. Toward a System of Zirconium Chemistry. *Ind Eng Chem.* 1954;46(3):528–39.
26. Xu ZG, Wang LJ, Wu YK, Chi RA, Zhang L, Wu M. Solvent extraction of hafnium from thiocyanic acid medium in DIBK-TBP mixed system. *Trans Nonferrous Met Soc China (English Ed [Internet].* 2012;22(7):1760–5. Available from: [http://dx.doi.org/10.1016/S1003-6326\(11\)61384-8](http://dx.doi.org/10.1016/S1003-6326(11)61384-8)
27. Wang LY, Lee MS. A review on the aqueous chemistry of Zr(IV) and Hf(IV) and their separation by solvent extraction. *J Ind Eng Chem [Internet].* 2016;39:1–9. Available from: <http://dx.doi.org/10.1016/j.jiec.2016.06.004>
28. Pandey G, Mukhopadhyay S, Renjith AU, Joshi JM, Shenoy KT. Recovery of Hf and Zr from slurry waste of zirconium purification plant using solvent extraction. *Hydrometallurgy [Internet].* 2016;163:61–8. Available from: <http://dx.doi.org/10.1016/j.hydromet.2016.03.005>
29. Conradie EW. Selective membrane based solvent extraction of Hf from a $(\text{NH}_4)_3\text{Zr}(\text{Hf})\text{F}_7$ solution. North-West University; 2016.
30. Rydberg J, Cox M. *Solvent Extraction Principles and Practice.* Rydberg J, Cox M, Musikas C, Choppin GR, editors. New York: Taylor & Francis Group, LLC.; 2004.
31. Gawroński R, Wrzesińska B. Kinetics of solvent extraction in hollow-fiber contactors. *J Memb Sci.* 2000;168(1–2):213–22.
32. Kertész R, Schlosser Š. Design and simulation of two phase hollow fiber contactors for simultaneous membrane based solvent extraction and stripping of organic acids and bases. *Sep Purif Technol.* 2005;41(3):275–87.
33. Fadaei F, Shirazian S, Ashrafizadeh SN. Mass transfer simulation of solvent extraction in hollow-fiber membrane contactors. *Desalination.* 2011;275(1–3):126–32.
34. Van der Westhuizen DJ. *Separation of Zirconium and Hafnium via Solvent Extraction.* North-West University; 2010.
35. Kertész R, Šimo M, Schlosser Š, Šimo M. Membrane-based solvent extraction and stripping of phenylalanine in HF contactors. *J Memb Sci.* 2005;257(1–2):37–47.
36. Wang LY, Lee MS. Separation of zirconium and hafnium from nitric acid solutions with LIX 63, PC 88A and their mixture by solvent extraction. *Hydrometallurgy [Internet].*

- 2014;150:153–60. Available from: <http://dx.doi.org/10.1016/j.hydromet.2014.10.009>
37. Mukherji AK. ANALYTICAL CHEMISTRY OF ZIRCONIUM AND HAFNIUM. First. Pergamon Press; 1970.
 38. Taghizadeh M, Ghasemzadeh R, Ashrafizadeh SN, Saberyan K, Maragheh MG. Determination of optimum process conditions for the extraction and separation of zirconium and hafnium by solvent extraction. *Hydrometallurgy*. 2008;90(2–4):115–20.
 39. Wang LY, Lee MS. Solvent Extraction of Zr(IV) and Hf(IV) from Sulfuric Acid Solutions by Acidic Extractants and Their Mixtures with TBP. *J Korean Inst Resour Recycl*. 2016;25(2):3–9.
 40. Wang LY, Lee MS. Separation of Zr and Hf from sulfuric acid solutions with amine-based extractants by solvent extraction. *Sep Purif Technol [Internet]*. 2015;142:83–9. Available from: <http://dx.doi.org/10.1016/j.seppur.2015.01.001>
 41. Biswas RK, Hayat MA. Solvent extraction of zirconium(IV) from chloride media by D2EHPA in kerosene. *Hydrometallurgy*. 2002;63(2):149–58.
 42. Reddy BR, Kumar JR, Raja KP, Reddy AV. Solvent extraction of Hf(IV) from acidic chloride solutions using Cyanex 302. *Miner Eng*. 2004;17(7–8):939–42.
 43. Reddy BR, Kumar JR, Reddy AV. Solvent extraction of zirconium(IV) from acid chloride solutions using LIX 84-IC. *Hydrometallurgy*. 2004;74(1–2):173–7.
 44. Taghizadeh M, Ghasemzadeh R, Ashrafizadeh SN, Ghannadi M. Stoichiometric relation for extraction of zirconium and hafnium from acidic nitrate solutions with Cyanex272. *Hydrometallurgy*. 2009;96(1–2):77–80.
 45. Nayl AA, El-Nadi YA, Daoud JA. Extraction and separation of Zr(IV) and Hf(IV) from nitrate medium by some CYANEX extractants. *Sep Sci Technol*. 2009;44(12):2956–70.
 46. Wang LY, Lee MS. Solvent extraction reaction of hafnium(IV) from strong sulfuric acid solutions with D2EHPA and PC 88A. *Sep Sci Technol [Internet]*. 2016;51(5):759–66. Available from: <http://dx.doi.org/10.1080/01496395.2015.1119841>
 47. Marták J, Schlosser Š, Vlčková S. Pertraction of lactic acid through supported liquid membranes containing phosphonium ionic liquid. *J Memb Sci*. 2008;318(1–2):298–310.
 48. Mans N. The cobalt-nickel pertraction refinery to process recycled spent catalysts leach solutions. North-West University; 2018.
 49. Wongsawa T, Sunsandee N, Pancharoen U, Lothongkum AW. High-efficiency HFSLM for silver-ion pertraction from pharmaceutical wastewater and mass-transport models. *Chem Eng Res Des [Internet]*. 2014;92(11):2681–93. Available from:

- <http://dx.doi.org/10.1016/j.cherd.2014.01.005>
50. Soldenhoff K, Shamieh M, Manis A. Liquid-liquid extraction of cobalt with hollow fiber contactor. *J Memb Sci.* 2005;252(1–2):183–94.
 51. R.W. B. *Membrane Technology and Applications* [Internet]. 2nd ed. John Wiley & Sons Ltd. New York; 2004. Available from: https://www.academia.edu/31551491/Modul_F_Reverse_Osmosis
 52. Schlosser Š, Kertész R, Marták J. Recovery and separation of organic acids by membrane-based solvent extraction and pertraction: An overview with a case study on recovery of MPCA. *Sep Purif Technol.* 2005;41(3):237–66.
 53. Bocquet S, Torres A, Sanchez J, Rios GM, Romero J. Modeling the mass transfer in solvent-extraction processes with hollow-fiber membranes. *AIChE J.* 2005;51(4):1067–79.
 54. Chaturabul S, Srirachat W, Wannachod T, Ramakul P, Pancharoen U, Kheawhom S. Separation of mercury(II) from petroleum produced water via hollow fiber supported liquid membrane and mass transfer modeling. *Chem Eng J* [Internet]. 2015;265:34–46. Available from: <http://dx.doi.org/10.1016/j.cej.2014.12.034>
 55. Valenzuela F, Basualto C, Tapia C, Sapag J. Application of hollow-fiber supported liquid membranes technique to the selective recovery of a low content of copper from a Chilean mine water. *J Memb Sci.* 1999;155(1):163–8.
 56. Trivunac K, Stevanovic S, Mitrovic M. Pertraction of phenol in hollow-fiber membrane contactors. *Desalination.* 2004;162(1–3):93–101.
 57. Hasanoğlu A. Removal of phenol from wastewaters using membrane contactors: Comparative experimental analysis of emulsion pertraction. *Desalination.* 2013;309:171–80.
 58. Červeňanský I, Mihaľ M, Markoš J. Potential application of perfusion and pertraction for in situ product removal in biocatalytic 2-phenylethanol production. *Sep Purif Technol.* 2017;183:11–20.
 59. Carrera JA, Muñoz E, Bringas E, San Román MF, Ortiz I. Influence of operation variables on the recovery of zinc from spent pickling effluents using the emulsion pertraction technology. *Desalination* [Internet]. 2009;245(1–3):675–9. Available from: <http://dx.doi.org/10.1016/j.desal.2009.02.036>
 60. Incropera FP, Dewitt DP, Bergman TL, Lavine AS. *Fundamentals of heat and mass transfer.* Sixth. John Wiley & Sons, Inc.; 2013.

61. Wu J, Chen V. Shell-side mass transfer performance of randomly packed hollow fiber modules. *J Memb Sci.* 2000;172(1–2):59–74.
62. Welty JRJ, Wicks CEC, Wilson RRE, Rorrer GLG. *Fundamentals of Momentum, Heat, and Mass Transfer.* 5th ed. Vol. 1, John Wiley and Sons. Joh; 2008. 2–6 p.
63. Wang CY, Mercer E, Kamranvand F, Williams L, Kolios A, Parker A, et al. Tube-side mass transfer for hollow fibre membrane contactors operated in the low Graetz range. *J Memb Sci [Internet].* 2017;523(June 2016):235–46. Available from: <http://dx.doi.org/10.1016/j.memsci.2016.09.049>
64. Asimakopoulou AG, Karabelas AJ. Mass transfer in liquid-liquid membrane-based extraction at small fiber packing fractions. *J Memb Sci.* 2006;271(1–2):151–62.
65. Mohammadi S, Kaghazchi T, Kargari A. A model for metal ion pertraction through supported liquid membranes. *Desalination.* 2008;219(1–3):324–34.
66. Mavroudi M, Kaldis SP, Sakellaropoulos GP. A study of mass transfer resistance in membrane gas-liquid contacting processes. *J Memb Sci.* 2006;272(1–2):103–15.
67. Sitaraman R, Ibrahim SH, Kuloor NR. A Generalized Equation for Diffusion in Liquids. *J Chem Eng Data.* 1963;8(2):198–201.
68. Zhang LZ. Heat and mass transfer in a randomly packed hollow fiber membrane module: A fractal model approach. *Int J Heat Mass Transf [Internet].* 2011;54(13–14):2921–31. Available from: <http://dx.doi.org/10.1016/j.ijheatmasstransfer.2011.03.005>
69. Koekemoer LR, Badenhorst MJG, Everson RC. Determination of viscosity and density of Di-(2-ethylhexyl) phosphoric acid + aliphatic kerosene. *J Chem Eng Data.* 2005;50(2):587–90.
70. Koekemoer LR. The evaluation of the mechanisms involved in the extraction of nickel from low concentration effluents by means of supported liquid membranes. 2005.
71. Vernekar P V., Jagdale YD, Patwardhan AW, Patwardhan A V., Ansari SA, Mohapatra PK, et al. Transport of cobalt(II) through a hollow fiber supported liquid membrane containing di-(2-ethylhexyl) phosphoric acid (D2EHPA) as the carrier. *Chem Eng Res Des [Internet].* 2013;91(1):141–57. Available from: <http://dx.doi.org/10.1016/j.cherd.2012.06.019>
72. 3M. *Liqui-Cell 1.7x8.75 Minimodule Specification Sheet.* 2011.
73. De Beer L. *The selective extraction of Hf from Zr(Hf)Cl4(aq) using organophosphorous derivatives.* North West University; 2015.
74. SciLabware. *Plastic Chemical compatibility [Internet].* Staffordshire; Available from:

https://www.dwk ltd.com/pub/mediawysiyg/pdf/Plastic_Chemical_Compatibility_Chart_poster.pdf

75. Mat NC, Lou Y, Lipscomb GG. Hollow fiber membrane modules. *Curr Opin Chem Eng* [Internet]. 2014;4:18–24. Available from: <http://dx.doi.org/10.1016/j.coche.2014.01.002>
76. Zahakifar F, Charkhi A, Torab-mostaedi M, Davarkhah R. Performance evaluation of hollow fiber renewal liquid membrane for extraction of uranium (VI) from acidic sulfate solution. 2017;(January).
77. 3M. 1.7x8.75 MiniModule with NPT Liquid ports. 2016.
78. Liqui-Cel 3M. Design & Operating Procedures.
79. Liqui-Cel 3M. 3M™ Liqui-Cel™ EXF-8x20 Industrial Series Membrane Contactor [Internet]. 2017. Available from: <https://multimedia.3m.com/mws/media/1412462O/3m-liqui-cel-exf-8x20-ind-series-membrane-contactorlc-1034-pdf.pdf>
80. LP SC. ShellSol 2325 Handling sheet. Houston; 2017.

Appendix A

This appendix contains additional information related to the ShellSol 2325 solvent (A1), the Liqui-Cel™ 1.7x8.75 Minimodule datasheets (A2), the raw data of the Zr salt purity analysis (A3), the data related to the uncertainty analyses (A4), and a copy of the Polymath™ algorithm (A5). The data sheets for ShellSol 2325, and the Liqui-Cel™ 1.7x8.75 Minimodules are only partial sections containing the relevant parameters used in the study.

A1: ShellSol 2325 specifications

Product Details

Product Name:	ShellSol 2325
Shipping Name:	Kerosene
Chemical Family:	Naphtha
Product Code:	Q3351

SDS: <http://www.shell.com/business-customers/chemicals/safe-product-handling-and-transportation/safety-data-sheets.html>

Physical Properties

Density:	814 g/cm ³ (20 °C / 68 °F)
Dynamic Viscosity:	Data not available
Vapor Pressure:	Typical 0.01 Pa (20 °C / 68 °F)
Boiling Point:	Typical 215 - 250 °C / 419 - 482 °F
Pour Point:	< -30 °C / -22 °F
Flash Point:	Typical 89 °C / 192 °F
Appearance:	Colourless

Note 1: Physical Properties are for reference only and valid as of date of this revision; see loading terminal for specific properties.

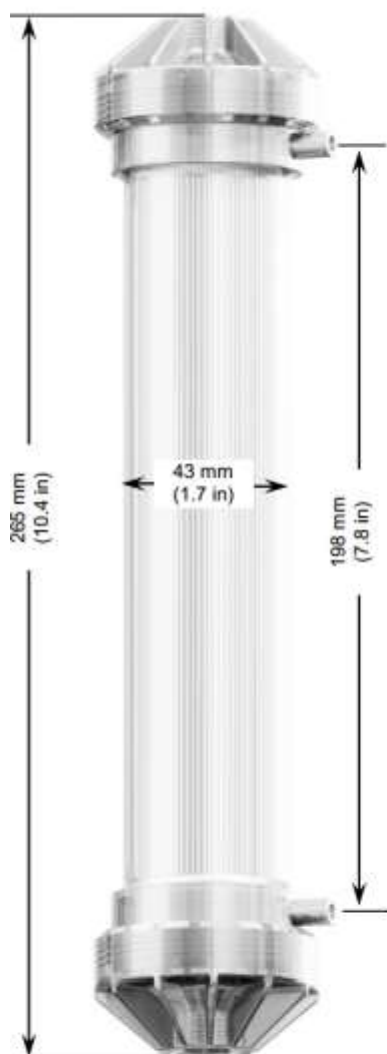
Note 2: This product is a Static Accumulator.

Figure A-1: A section of the ShellSol 2325 data sheet. Adapted from [80].

A2: Minimodule datasheet and dimensional drawing



1.7 x 8.75 MiniModule™ PRODUCT DATA SHEET



Note: All dimensions are nominal values. Refer to liqui-cel.com for detailed housing drawings.



Membrane Characteristics	
Cartridge Configuration	Parallel Flow, Lumenside Liquid Flow.
Liquid Flow Guidelines	<3000 ml/min
Membrane Type	X50 Fiber
Membrane/Potting Material	Polypropylene/Polyurethane
Typical Membrane Surface Area	0.9 m ² <small>Calculated based on inner diameter of hollow fiber</small>
Priming Volume (approximate)	
Shellside	140 ml
Lumenside	70 ml
Pressure Guidelines*	
Maximum Lumenside <u>LIQUID</u> Working Temperature/ Pressure	5-20° C, 4.1 barg (41-68° F, 60 psig) 40° C, 2.1 barg (104° F, 30 psig)
* Note: Liquid pressure should always exceed gas pressure.	
Housing Options and Characteristics	
Material	Polycarbonate
Flange Connections	
Shellside (gas/vacuum)	Standard Female Luer Lock <i>Supplied with two ¼ inch Hosebarb adaptors which mate to ¼ inch ID tubing</i>
Lumenside (wetted surface)	1/4 inch FNPT
Seal Options	
Material	EPDM
Applications	All Purpose
Weight (approximate)	
Dry	186 grams
Shipping weight (max)	196 grams
Regulatory	
Complies with the limits as set by RoHS Directive 2011/65/EU Annex II; recasting 2002/95/EC. Constructed of FDA CFR title 21 compliant materials for wetted parts only at ambient temperatures.	



Figure A-2: A partial section of the data sheet for the Minimodules™ used in the present study Adapted from [72].

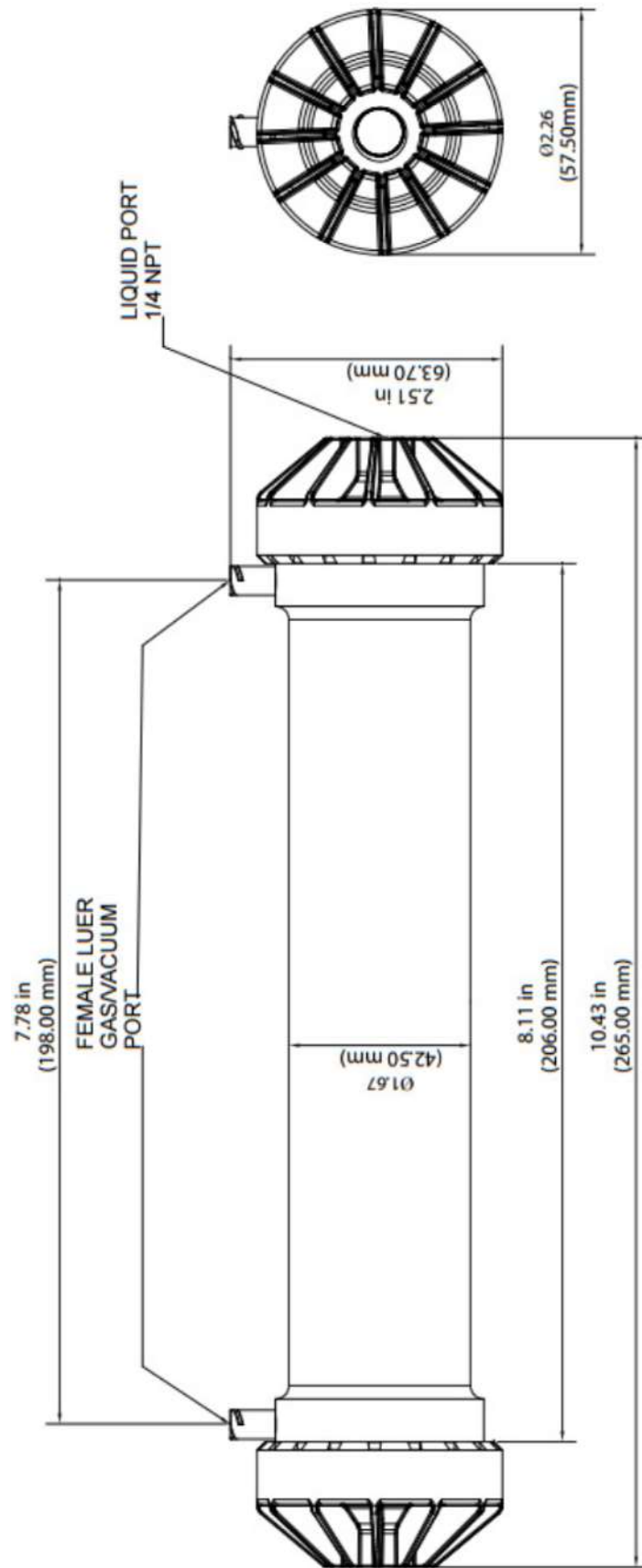


Figure A-3: A dimensional drawing of the Minimodules™ used in the present study. Adapted from [77].

A3: The raw data of the Zr salt purity analysis

The purity of the industrial-grade $\text{Zr(Hf)(SO}_4)_2(\text{H}_2\text{O})_4$ salt was determined by dissolving 1.00 g of the salt in 100 mL water and analysing the solution by ICP-OES. The concentrations of Zr and Hf were used to determine what the hypothetical mass of hydrated sulphate salt would be in the sample. The hypothetical mass was compared to the actual mass and the purity taken as the ratio of the hypothetical mass to the actual mass. The Hf content was determined as the mass ratio of Hf: (Zr + Hf) in the sample. The relevant data is listed in Table A-1.

Table A-1: The raw data used to determine the purity of the $\text{Zr(Hf)(SO}_4)_2(\text{H}_2\text{O})_4$ salt.

Parameter	Unit	Value				Average
		1	2	3	4	
Salt mass weighed	g	1.001	1.001	1.004	1.004	
Zr concentration	ppm	2 530	2 529	2 453	2 510	
Hf concentration	ppm	54.74	58.24	57.18	58.55	
$\text{Zr(SO}_4)_2(\text{H}_2\text{O})_4$ mass	g	0.986	0.985	0.956	0.978	
$\text{Hf(SO}_4)_2(\text{H}_2\text{O})_4$ mass	g	0.014	0.014	0.014	0.015	
Salt purity	%	99.8	99.9	96.6	98.8	98.8
Hf content	%	2.12	2.25	2.28	2.28	2.23

A4: Statistical uncertainty analysis data

The experimental uncertainties were determined by repeating selected experiments. Outliers in the data sets were determined using Tukey’s method and eliminated before the uncertainties were determined.

The LLE data, listed in Table A-2, consisted of three repeated experimental points, with the maximum deviation away from the overall average being 3.5% for Zr and 3.0% for Hf. The maximum deviations are in bold print. The LLE uncertainty was rounded up to 5% for both Zr and Hf.

The MBSE data consisted of two repeated experiments with 7 data points for each experiment. The data for Zr and Hf are listed in Table A-3 and Table A-4, respectively. The eliminated outliers have been identified in the tables but were excluded from any calculations. The shell and lumen terms used in Table A-3 and Table A-4 serve as identifiers and refer to the series of experiments in which the specific experiment was conducted, see Section 4.3.1 and 4.3.2, respectively. The maximum deviation from the overall average for the Zr data was approximately 3.9%, while that of Hf was approximately 5.6%, again shown in bold print in the tables. The MBSE uncertainty for Zr was rounded to 5% while that of Hf was rounded to 10%.

Table A-2: The data used to determine the LLE experimental uncertainty.

Parameter	Zr				Hf					
	Experiment	Repeat	1	2	3	Average	1	2	3	Average
Normalized outlet conc.			0.69	0.70	0.66	0.68	0.46	0.44	0.47	0.46
Extraction %			31.1	30.4	34.4	32.0	54.1	55.6	53.1	54.2
Deviation from average			1.3	2.2	3.5	2.3	0.4	3.0	2.6	2.0

Table A-3: The MBSX data used to determine the Zr experimental uncertainty.

Zr Experimental Uncertainty	Unit	Time (min)							
		2	3	4	5	6	7	8	
Normalized Shell Outlet	-	0.93	0.89	0.90	Outlier	0.93	0.93	0.89	
Normalized Lumen Outlet	-	0.92	0.89	0.87	0.89	0.92	0.91	0.91	
Shell deviation from average	%	2.5	1.5	0.3		2.2	2.3	1.5	
Lumen deviation from average	%	1.7	1.3	3.9	2.1	1.3	0.4	0.3	

Table A-4: The MBSX data used to determine the Hf experimental uncertainty.

Hf Experimental Uncertainty	Unit	Time (min)						
		2	3	4	5	6	7	8
Normalized Shell Outlet	-	0.89	Outlier	0.85	0.87	0.86	0.85	0.83
Normalized Lumen Outlet	-	0.91	0.89	0.85	0.86	0.86	0.87	0.87
Shell deviation from average	%	2.7		2.3	0.1	1.2	2.0	4.6
Lumen deviation from average	%	5.6	3.4	1.4	1.0	0.3	0.1	1.0

A5: The Polymath™ algorithm used in this study

Included is a copy of the algorithm code that was created to solve the design equation given in Eq. 2-7. The design equation was applied to the shell and lumen concentrations of both Zr and Hf. The shell-side concentration profiles were calculated from the shell inlet to the outlet, while due to the counter-current flow the lumen concentrations were determined from the lumen outlet backwards to the inlet conditions. The values for the individual mass transfer coefficients were calculated in MS™ Excel and inserted into polymath due to a restriction on the number of equations that could be used with a free licence.

$d(\text{CaqZr})/d(A) = -\text{kovZr} * (\text{CaqZr} - \text{CorgZr} / \text{PZr}) / \text{Qaq}$ # Shell-side Zr profile
 $\text{CaqZr}(0) = 16$ # Zr concentration entering the column (kg.m^{-3})

$d(\text{CorgZr})/d(A) = -\text{kovZr} * (\text{CaqZr} - \text{CorgZr} / \text{PZr}) / \text{Qorg}$ # Lumen-side Zr profile
 $\text{CorgZr}(0) = 1.47$ # Loaded organic phase Zr concentration leaving the column (kg.m^{-3})

$d(\text{CaqHf})/d(A) = -\text{kovHf} * (\text{CaqHf} - \text{CorgHf} / \text{PHf}) / \text{Qaq}$ # Shell-side Hf profile
 $\text{CaqHf}(0) = 0.36$ # Hf concentration entering the column (kg.m^{-3})

$d(\text{CorgHf})/d(A) = -\text{kovHf} * (\text{CaqHf} - \text{CorgHf} / \text{PHf}) / \text{Qorg}$ # Lumen-side Hf profile
 $\text{CorgHf}(0) = 0.033$ # Loaded organic phase Hf concentration leaving the column (kg.m^{-3})

$A(0) = 0$ # Starting surface area for aqueous phase (m^2)
 $A(f) = 2100$ # Final surface area of membrane column, end of the integral window (m^2)

$U_{\text{aq}} = 1\text{e-}4$ # Shell-side velocity (m.s^{-1})
 $U_{\text{org}} = 0.01$ # Lumen-side velocity (m.s^{-1})

$\text{Impurity} = \text{CaqHf} / (\text{CaqZr}) * 1\text{e}6$ # Hf:Zr ratio in ppm
 $\text{Recovery} = (\text{CaqZr}/16) * 100$ # Percentage of Zr remaining in Feed
 $\text{Loading} = \text{CorgZr} + \text{CorgHf}$ # Lumen loading (total concentration of metal in organic phase)

$\text{kovZr} = 0.0032 * (0.077 \wedge 0.28) * (1365 \wedge 0.33) * (1.40\text{e-}9 / 1.46\text{e-}3)$ # Zr Sherwood
 $\text{kovHf} = 0.0036 * (0.077 \wedge 0.16) * (1277 \wedge 0.33) * (1.49\text{e-}9 / 1.46\text{e-}3)$ # Hf Sherwood

$\text{PZr} = 20.7$ # Partition coefficient of Zr
 $\text{PHf} = 157$ # Partition coefficient of Hf

$\text{Qaq} = 3.77\text{e-}2 * U_{\text{aq}}$ # Conversion of velocity to volumetric flow rate ($\text{m}^3.\text{s}^{-1}$)
 $\text{Qorg} = 4.116\text{e-}3 * U_{\text{org}}$ # Conversion of velocity to volumetric flow rate ($\text{m}^3.\text{s}^{-1}$)
 $\text{OA} = \text{Qorg} / \text{Qaq}$ # Polymath calculated volumetric Shell: Lumen ratio, safety check
 $\text{Sep} = \text{kovHf} / \text{kovZr}$ # Polymath calculated separation ratio, safety check

Appendix B

This appendix contains the raw and processed data that is provided in the main body of the dissertation as well as the calculations that were performed on the raw data. The appendix is divided into three sections; B1, which discusses the LLE data, B2, which discusses the MBSX data, and B3, which elaborates on the mass transfer modelling and fitting the Sherwood relations. The calculations with the data sets are discussed in the relevant sections with data tables and figures provided.

B1: LLE data

This section discusses the LLE portion of the experimental data. The raw data is provided first, followed by an example of the data processing to obtain the desired parameters. A fully populated LLE data table is provided near the end of this section along with figures illustrating the comparison between data sets.

The raw data that are listed Table B-1 and Table B-2 have been converted from the parts per million output format from the ICP data to g.L⁻¹. Both data sets (1 and 2) were done twice (A and B) to determine repeatability. Note that the H₂SO₄ and 1-octanol concentrations were omitted from the tables as they were fixed at 98, and 4.1 g.L⁻¹, respectively throughout the all the LLE and MBSX experiments. The purpose of the LLE experiments was to determine the partition coefficients for Zr and Hf at D2EHPA concentrations that better matched the stoichiometric ratio of the increased metal concentration in the feed phase.

Table B-1: LLE raw data for low D2EHPA concentration range.

Organic phase		Initial aqueous phase		Equilibrium aqueous phase	
D2EHPA g.L ⁻¹	E:M mol.mol ⁻¹	Hf g.L ⁻¹	Zr g.L ⁻¹	Hf g.L ⁻¹	Zr g.L ⁻¹
Data set 1 A					
6.60	0.12	0.37	16.05	0.35	15.12
16.1	0.28	0.37	16.05	0.31	14.94
32.1	0.56	0.37	16.05	0.24	14.17
48.3	0.84	0.37	16.05	0.21	12.12
62.6	1.09	0.37	16.05	0.17	11.06
Data set 1 B					
6.60	0.12	0.37	16.05	0.35	15.61
16.1	0.28	0.37	16.05	0.33	14.82
32.1	0.56	0.37	16.05	0.26	14.07
48.3	0.84	0.37	16.05	0.19	12.20
62.6	1.09	0.37	16.05	0.16	11.17

Table B-2: LLE raw data for high D2EHPA concentration range.

Organic phase		Initial aqueous phase		Equilibrium aqueous phase	
D2EHPA	E:M	Hf	Zr	Hf	Zr
g.L ⁻¹	mol.mol ⁻¹	g.L ⁻¹	g.L ⁻¹	g.L ⁻¹	g.L ⁻¹
Data set 2 A					
62.6	1.2	0.34	14.54	0.10	9.50
91.4	1.8	0.34	14.54	0.07	6.92
122	2.3	0.34	14.54	0.04	4.77
152	2.9	0.34	14.54	0.01	2.80
183	3.5	0.34	14.54	0.01	1.44
213	4.1	0.34	14.54	2.2 x10 ⁻³	0.67
305	5.9	0.34	14.54	3.2 x10 ⁻⁴	0.06
Data set 2 B					
62.6	1.2	0.34	14.54	0.16	9.55
91.4	1.8	0.34	14.54	0.06	6.89
122	2.3	0.34	14.54	0.03	4.64
152	2.9	0.34	14.54	0.02	2.80
183	3.5	0.34	14.54	0.01	1.46
213	4.1	0.34	14.54	2.1 x10 ⁻³	0.66
305	5.9	0.34	14.54	4.5 x10 ⁻⁴	0.06

This processing example utilises point 2 ([D2EHPA] = 91 g.L⁻¹) from data set 2 A. The feed solution was prepared as a large volume of stock solution and sampled for analysis prior to the experiments. It was assumed that the initial concentrations of each individual feed solution were identical. The Zr concentration of the feed solution was measured as 14.54 g.L⁻¹ while the equilibrium Zr concentration was measured as 6.92 g.L⁻¹.

Under the assumption that any change in concentration was the result of only the extraction reaction by D2EHPA, the organic phase concentration was determined using Eq. B 1. In the present study, the volume ratio of the LLE experiments was always maintained at 1:1, therefore:

$$C_{org} = (C_{aq}^{initial} - C_{aq}^{equilibrium}) \left(\frac{V_{org}}{V_{aq}} \right) \quad \text{B 1}$$

$$C_{org} = (14.54 - 6.92) \left(\frac{1}{1} \right) = 7.60 \text{ g.L}^{-1}$$

The partition coefficient (P) was defined as the ratio of the organic phase concentration to the aqueous phase concentration:

$$P_{Zr} = \frac{C_{org}^{Zr}}{C_{aq}^{Zr}} \quad \text{B 2}$$

$$P_{Zr} = \frac{7.60}{6.92} = 1.10$$

Repeating the above steps with the Hf concentration data from the same experiment yields an organic phase concentration of 0.27 g.L⁻¹, and a partition coefficient of 3.85.

The separation factor (SF) between Hf and Zr was defined as the ratio of the partition coefficients of the two compounds:

$$SF = \frac{P_{Hf}}{P_{Zr}} \quad \text{B 3}$$

$$SF = \frac{3.85}{1.10} = 3.50$$

The data listed in Table B-3 and Table B-4 were compiled by repeating the above process for every experimental point.

Table B-3: Populated LLE data table for low D2EHPA concentration range.

Organic phase		Initial aq. phase		Equilibrium aq. phase		Partition coefficient		Separation factor
[D2EHPA] g.L ⁻¹	E:M mol.mol ⁻¹	Hf g.L ⁻¹	Zr g.L ⁻¹	Zr g.L ⁻¹	Hf g.L ⁻¹	Hf -	Zr -	Hf: Zr -
Data set 1 A								
6.60	0.11	0.37	16.05	0.35	15.12	0.35	15.61	0.89
16.1	0.28	0.37	16.05	0.31	14.94	0.33	14.82	2.36
32.1	0.56	0.37	16.05	0.24	14.17	0.26	14.07	3.93
48.3	0.84	0.37	16.05	0.21	12.12	0.19	12.20	2.42
62.6	1.1	0.37	16.05	0.17	11.06	0.16	11.17	2.61
Data set 1 B								
6.60	0.11	0.37	16.05	0.35	15.61	0.04	0.03	1.49
16.1	0.28	0.37	16.05	0.33	14.82	0.12	0.08	1.39
32.1	0.56	0.37	16.05	0.26	14.07	0.42	0.14	2.97
48.3	0.84	0.37	16.05	0.19	12.20	0.93	0.32	2.96
62.6	1.1	0.37	16.05	0.16	11.17	1.25	0.44	2.86

Table B-4: Populated LLE data table for high D2EHPA concentration range.

Organic phase		Initial aq. phase		Equilibrium aq. phase		Partition coefficient		Separation factor
[D2EHPA]	E:M	Hf	Zr	Zr	Hf	Hf	Zr	Hf: Zr
g.L ⁻¹	mol.mol ⁻¹	g.L ⁻¹	g.L ⁻¹	g.L ⁻¹	g.L ⁻¹	-	-	-
Data set 2 A								
61	1.2	0.34	14.54	0.10	9.50	2.29	0.53	4.31
91	1.8	0.34	14.54	0.07	6.92	3.79	1.10	3.45
122	2.3	0.34	14.54	0.04	4.77	6.92	2.05	3.38
152	2.9	0.34	14.54	0.01	2.80	22.3	4.20	5.32
183	3.5	0.34	14.54	0.01	1.44	63.7	9.07	7.02
213	4.1	0.34	14.54	2.2 x10 ⁻³	0.67	153	20.8	7.39
305	5.9	0.34	14.54	3.2 x10 ⁻⁴	0.06	1048	232	4.52
Data set 2 B								
61	1.2	0.34	14.54	0.16	9.55	1.13	0.52	2.16
91	1.8	0.34	14.54	0.06	6.89	4.36	1.11	3.93
122	2.3	0.34	14.54	0.03	4.64	10.9	2.13	5.12
152	2.9	0.34	14.54	0.02	2.80	20.7	4.20	4.94
183	3.5	0.34	14.54	0.01	1.46	61.2	8.95	6.84
213	4.1	0.34	14.54	2.1 x10 ⁻³	0.66	159	20.9	7.61
305	5.8	0.34	14.54	4.5 x10 ⁻⁴	0.06	745	228	3.27

The partition coefficient and separation factor data listed in Table B-3 and Table B-4 have been illustrated in Figure B-1 and Figure B-2, respectively. Note that data sets A and B have been combined for aesthetic purposes.

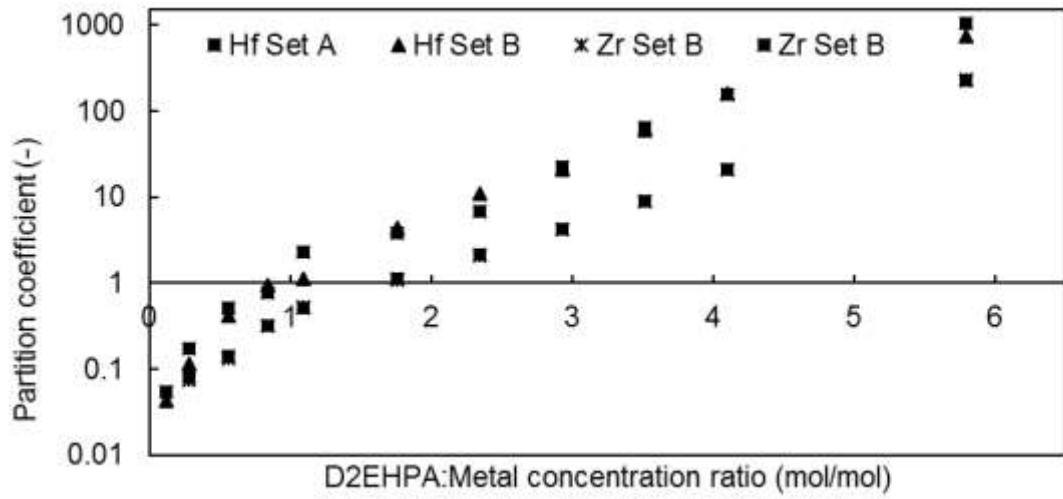


Figure B-1: The effect of the D2EHPA to metal molar ratio on the partition coefficients of Zr and Hf.

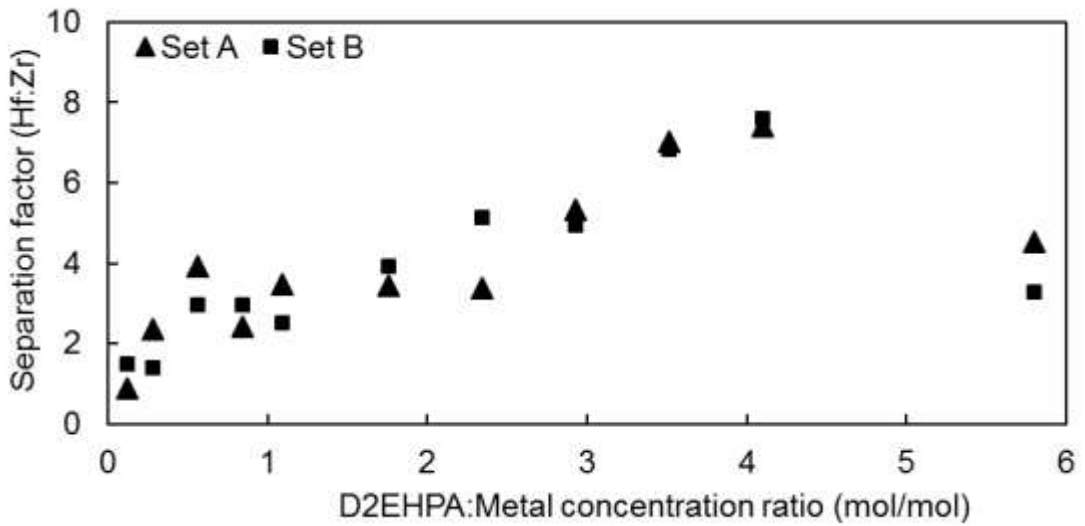


Figure B-2: The effect of the D2EHPA to metal molar ratio on the separation between Hf and Zr.

B2: MBSX data

Appendix B2 provides the raw MBSX data and how it was processed. It is divided into two subsections namely; i) the concentration data and, ii) the normalising of the data. In the first section, the unprocessed concentration data for Zr and Hf that was collected during the shell-side velocity variation experiments are listed, which is followed by the data collected during the lumen-side velocity variation experiments. Visual representations of the data are also provided. Following this, the normalising of the data is discussed alongside an example calculation and finally, the visual representations.

Measured concentration data

The measured concentration data for Zr and Hf gathered during the MBSX experiments are listed in Table B-5 and Table B-6 respectively. Each table contains concentration data from both the shell-side and lumen-side velocity variation series of experiments. Note that all the data represent the concentrations of the metals in the shell-side aqueous phase regardless of whether the velocity of the shell or lumen was varied. In these tables, the first data point, indicated as “Feed”, represents the bulk inlet concentration that was sampled for measurement prior to the start of each experiment. Data points 0 through 6 were taken from the shell-side outlet stream of the membrane column after contacting the organic phase. The samples were not taken from the outlet reservoir (see Figure 3-2).

After the organic phase had begun flowing out of the module (which indicated that both sides of the membrane had liquid flowing past it), the experiments were operated for two minutes (without samples being taken) to ensure stabilisation of the system. After two minutes, the experimental timer was started, and the first sample taken. Accordingly, the first data point was recorded at a time value of zero ($t=0$).

Values in the table that have been bolded represent either statistical outliers determined by the Tukey method, discussed in Section 3.4, or impossible values (e.g. a measured concentration value higher than the feed concentration). These values are reported in the data tables but were excluded from further consideration or calculations.

Zr Data

The Zr concentration data are listed Table B-5. The table contains data from both the shell-side velocity as well as the lumen-side velocity variation series of experiments. The variation between the feed concentrations were significant but due to a lack of resources and the structural failure of the modules these experiments could not be repeated. The shell-side velocity data is illustrated in Figure B-3 while the lumen-side velocity data is illustrated in Figure B-4 .

Table B-5: The measured Zr concentration (in g.L⁻¹) data for the shell-side and lumen-side velocity variation series of experiments. Bold face values indicate statistical outliers.

Time (min.)	Shell-side velocity (cm.s ⁻¹)			
	0.02	0.08	0.16	0.41
Feed	18.41	14.39	14.85	16.47
0	9.77	11.05	13.25	16.02
1	8.96	11.54	13.42	15.81
2	8.95	11.92	14.41	15.86
3	12.55	12.30	13.75	15.22
4	9.30	12.39	13.77	14.86
5	8.09	12.57	13.26	16.50
6	8.55	12.26	12.79	15.33
Outlet average	8.94	14.39	13.52	15.51

Time (min.)	Lumen-side velocity (cm.s ⁻¹)			
	0.07	0.34	0.67	1.7
Feed	16.10	17.93	15.69	15.08
0	15.15	15.49	14.46	13.27
1	15.17	15.48	14.04	13.33
2	15.87	15.08	13.66	13.38
3	15.09	15.11	13.92	13.69
4	14.80	14.73	14.40	13.08
5	17.33	13.42	14.27	13.36
6	15.98	14.09	14.26	13.18
Outlet average	15.34	14.77	14.14	13.27

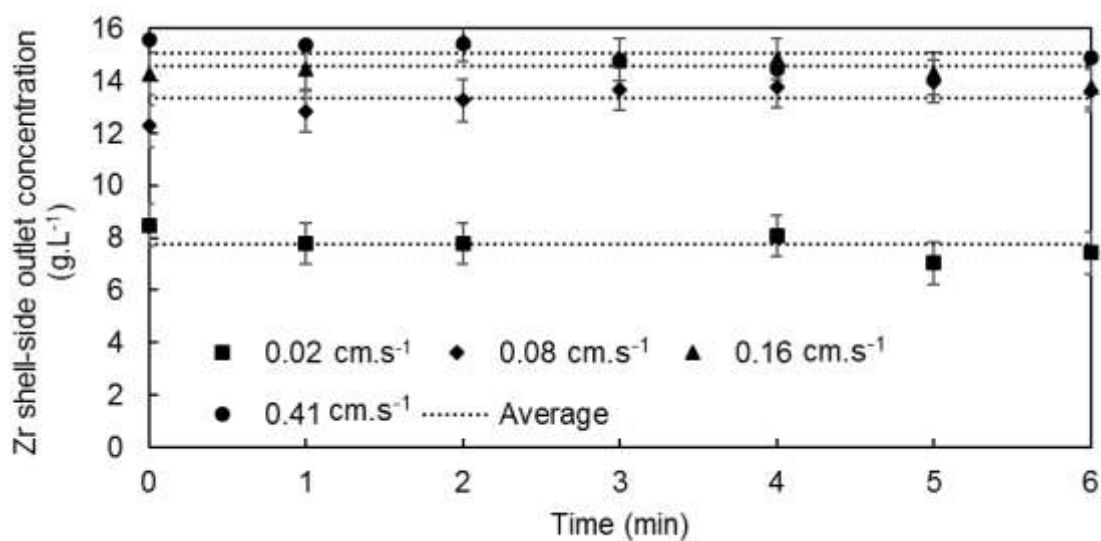


Figure B-3: The shell-side Zr outlet concentration as a function of time and shell-side velocity.

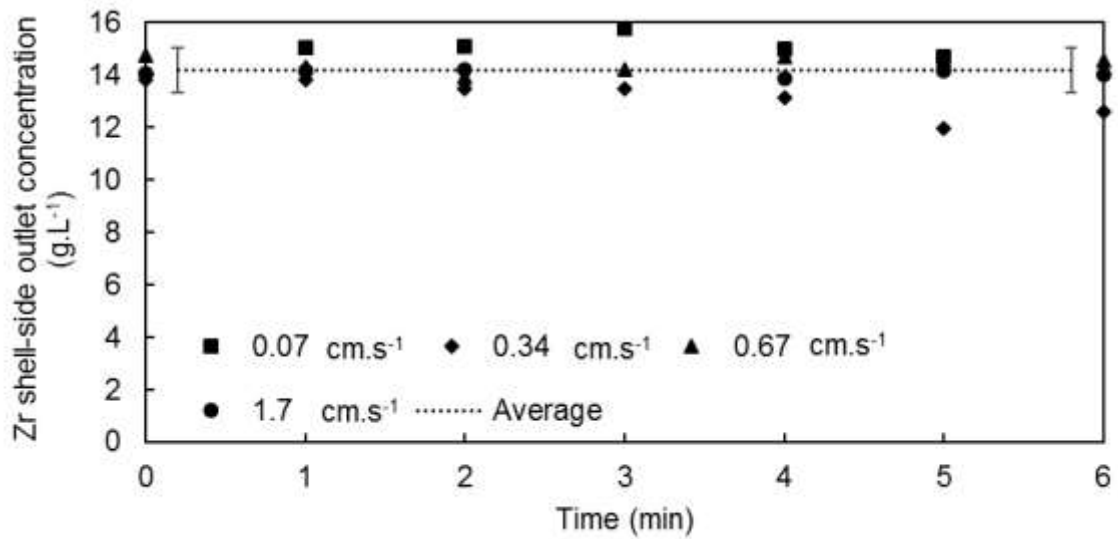


Figure B-4: The shell-side Zr outlet concentration as a function of time and lumen-side velocity.

Hf Data

The Hf concentration data are listed Table B-6. As with the Zr data, the table contains data from both the shell-side velocity as well as the lumen-side velocity variation series of experiments. The shell-side velocity data is illustrated in Figure B-5, while the lumen-side velocity data is illustrated in Figure B-6.

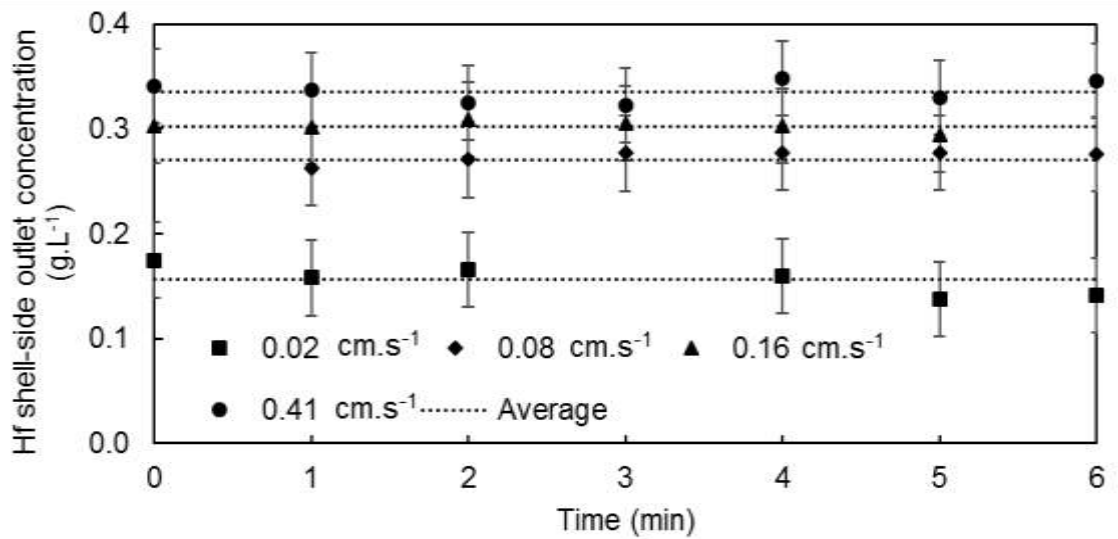


Figure B-5: The shell-side Hf outlet concentration as a function of time and shell-side velocity.

Table B-6: The measured Hf concentration (in g.L⁻¹) data for the shell-side and lumen-side velocity variation series of experiments. Bold face values indicate statistical outliers.

Time (min.)	Shell-side velocity (cm.s ⁻¹)			
	0.02	0.08	0.16	0.41
Feed	0.40	0.33	0.34	0.36
0	0.20	0.24	0.29	0.35
1	0.18	0.24	0.29	0.34
2	0.19	0.25	0.30	0.33
3	0.23	0.26	0.29	0.33
4	0.18	0.26	0.29	0.36
5	0.15	0.26	0.28	0.34
6	0.16	0.26	0.27	0.35
Outlet average	0.18	0.25	0.29	0.34

Time (min.)	Lumen-side velocity (cm.s ⁻¹)			
	0.07	0.34	0.67	1.7
Feed	0.37	0.40	0.36	0.34
0	0.34	0.34	0.31	0.28
1	0.34	0.34	0.31	0.29
2	0.36	0.32	0.29	0.29
3	0.34	0.32	0.29	0.29
4	0.34	0.32	0.29	0.28
5	0.39	0.30	0.30	0.28
6	0.36	0.31	0.30	0.27
Outlet average	0.34	0.32	0.30	0.28

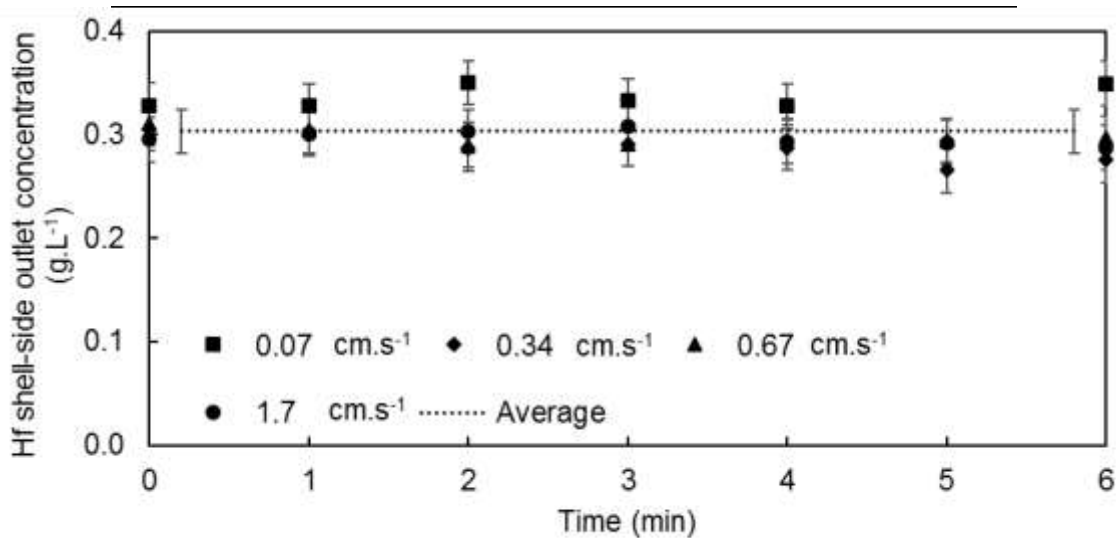


Figure B-6: The shell-side Hf outlet concentration as a function of time and lumen-side velocity.

Normalised concentration data

As large variations in the feed concentrations were measured by the ICP-OES, the data was normalised to concentrations for Zr and Hf of 16.0 and 0.361 g.L⁻¹, respectively. The Hf concentration factor was determined as 2.25% of 16.0 g.L⁻¹ (see Section 3.3.2 for a discussion of the Hf content of the metal salt used in this study). The procedure to prepare the solutions was conducted carefully and consistently for all the experimental work, therefore, it was assumed that the actual concentrations were near to the specified concentrations and the variations in the measured concentrations were attributed to the operation of the analysis equipment. This was addressed by normalising the concentration data by taking the ratio between the outlet and inlet concentrations of a specific experiment, multiplied by the specified concentration:

The illustrated example utilised the data from the shell-side velocity section of Table B-6. The shell-side Hf feed concentration at 0.41 cm.s⁻¹ was measured as 0.36 g.L⁻¹, while the outlet concentration at 5 minutes was measured as 0.34 g.L⁻¹. Therefore, the ratio of the outlet to inlet concentration was calculated as:

$$Ratio = \left(\frac{C^{Out}}{C^{In}} \right) \quad B\ 4$$

The normalised Zr concentration was therefore defined as:

$$C_{normalised}^{Hf} = 0.357(Ratio) = 0.357 \left(\frac{0.34}{0.36} \right) g.L^{-1} \quad B\ 5$$
$$C_{normalised}^{Hf} = 0.357 \left(\frac{0.34}{0.36} \right) = 0.34 g.L^{-1}$$

The normalised Zr content was determined in a similar manner, only using 16.0 as the reference concentration. Repeating the above process for all the data listed in Table B-5 and Table B-6, the data listed in Table B-7 and Table B-8 were obtained. The normalised concentration vs. time profiles are illustrated in Figure B-7 through Figure B-10.

Table B-7: The normalised Zr concentration (in g.L⁻¹) data for the shell-side and lumen-side velocity variation series of experiments. The statistical outliers have been removed.

Time (min.)	Shell-side velocity (cm.s ⁻¹)			
	0.02	0.08	0.16	0.41
Feed	16.0	16.0	16.0	16.0
0	8.5	12.3	14.3	15.6
1	7.8	12.8	14.5	15.4
2	7.8	13.3	15.5	15.4
3		13.7	14.8	14.8
4	8.1	13.8	14.8	14.4
5	7.0	14.0	14.3	
6	7.4	13.6	13.8	14.9
Outlet average	7.8	13.3	14.6	15.1

Time (min.)	Lumen-side velocity (cm.s ⁻¹)			
	0.07	0.34	0.67	1.7
Feed	16.0	16.0	16.0	16.0
0	15.1	13.9	14.8	14.1
1	15.1	13.8	14.3	14.2
2	15.8	13.5	13.9	14.2
3	15.0	13.5	14.2	
4	14.7	13.1	14.7	13.9
5		12.0	14.6	14.2
6	15.9	12.6	14.5	14.0
Outlet average	15.2	13.2	14.4	14.1

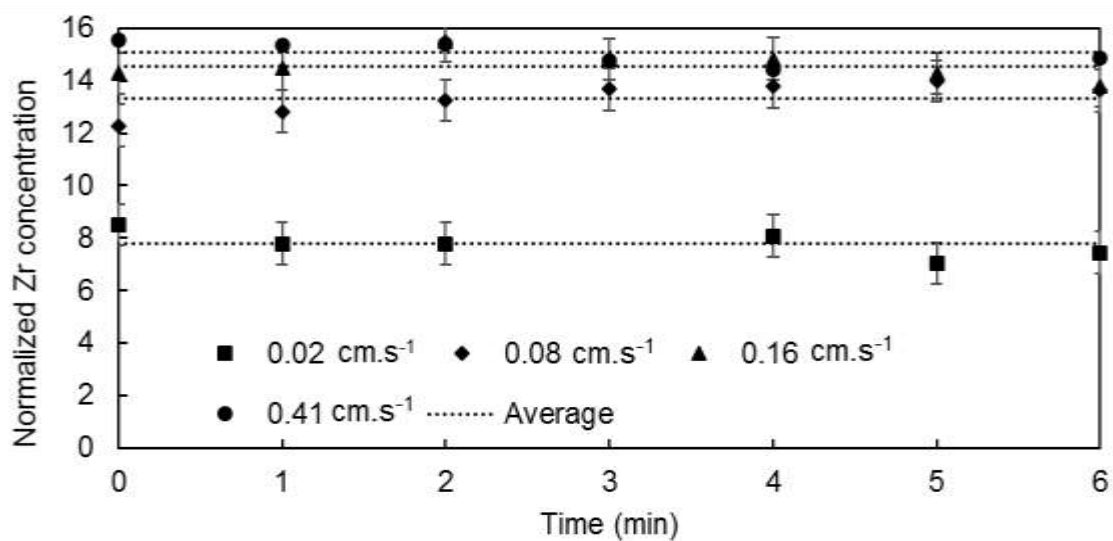


Figure B-7: The normalised shell-side Zr outlet concentration as a function of time and shell-side velocity.

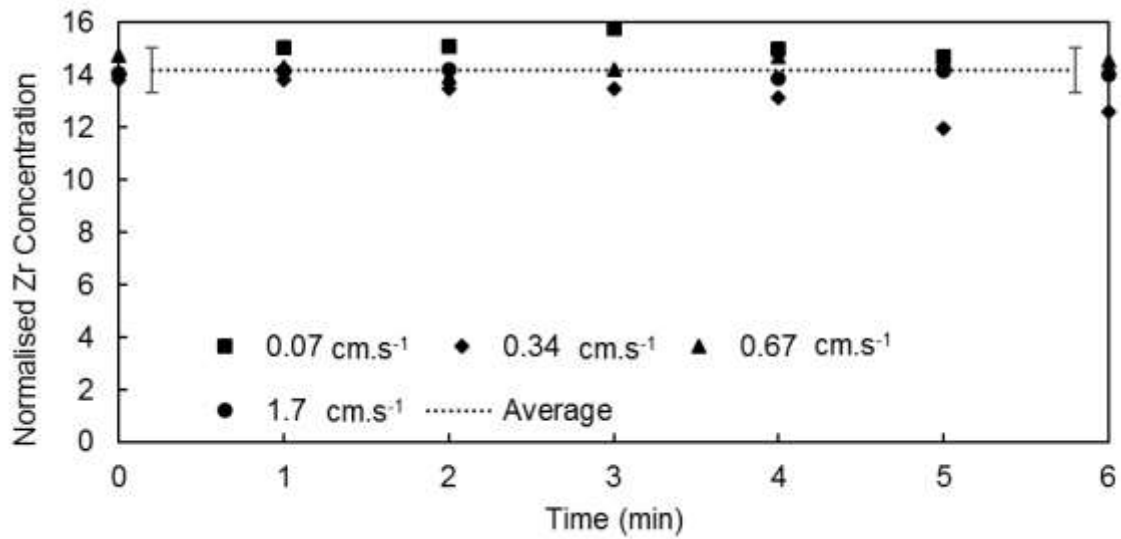


Figure B-8: The normalised shell-side Zr outlet concentration as a function of time and lumen-side velocity.

Table B-8: The normalised Hf concentration (in g.L⁻¹) data for the shell-side and lumen-side velocity variation series of experiments. The statistical outliers have been removed.

Time (min.)	Shell-side velocity (cm.s ⁻¹)			
	0.02	0.08	0.16	0.41
Feed	0.36	0.36	0.36	0.36
0	0.18	0.26	0.31	0.35
1	0.16	0.27	0.31	0.34
2	0.17	0.27	0.31	0.33
3		0.28	0.31	0.33
4	0.16	0.28	0.31	0.35
5	0.14	0.28	0.30	0.33
6	0.14	0.28		0.35
Outlet average	0.16	0.27	0.31	0.34
Time (min.)	Lumen-side velocity (cm.s ⁻¹)			
	0.07	0.34	0.67	1.7
Feed	0.36	0.36	0.36	0.36
0	0.33	0.31	0.31	0.30
1	0.33	0.31	0.31	0.30
2	0.35	0.29	0.29	0.31
3	0.34	0.29	0.29	0.31
4	0.33	0.29	0.30	0.30
5		0.27	0.30	0.30
6	0.35	0.28	0.30	0.29
Outlet average	0.34	0.29	0.30	0.30

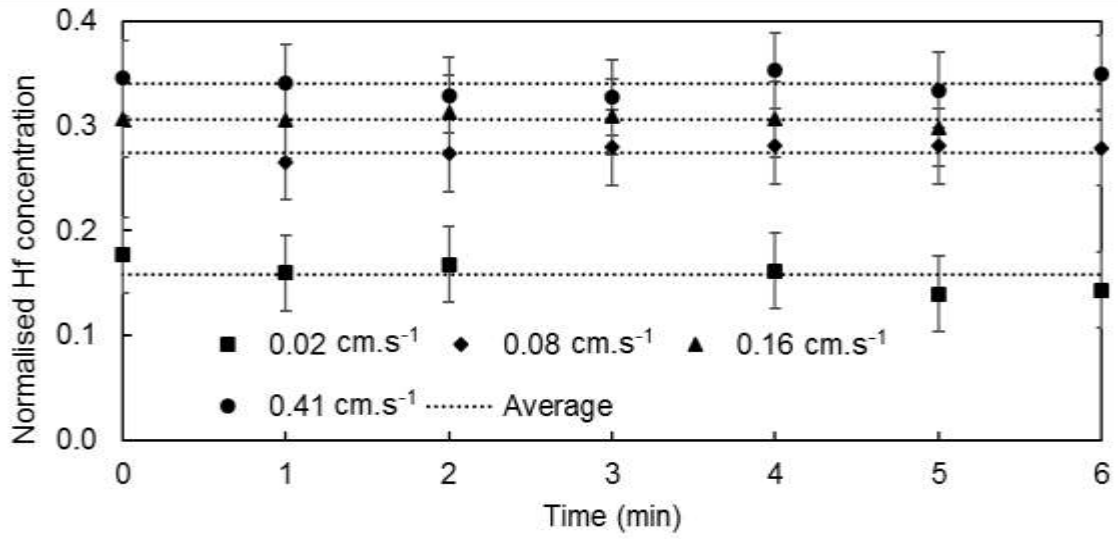


Figure B-9: The normalised shell-side Hf outlet concentration as a function of time and shell-side velocity.

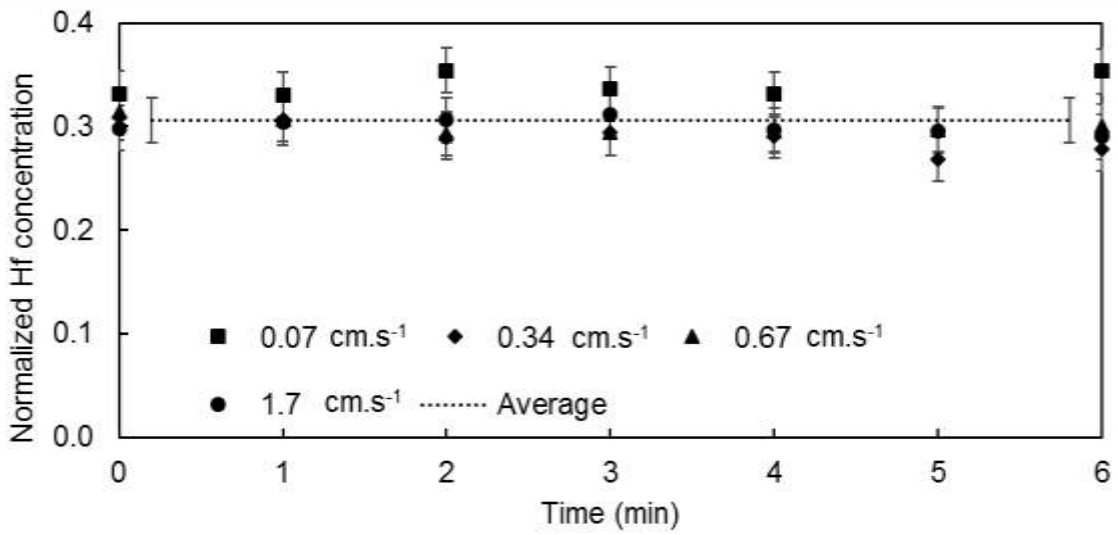


Figure B-10: The normalised shell-side Hf outlet concentration as a function of time and lumen-side velocity.

B3: Mass transfer data and modelling

Experimental overall mass transfer coefficients

The following section is discussed in detail in Section 2.6, therefore the present section will not elaborate on derivations or assumptions more than is necessary. The example calculation is illustrated using the concentration data for Hf taken from the shell-side velocity 0.41 cm.s^{-1} experimental data listed in Table B-8. An average outlet concentration was determined for each velocity and used for all the calculations. In this example the shell-side inlet Hf concentration was 0.36 g.L^{-1} , while the average outlet concentration was 0.34 g.L^{-1} . As the organic phase did not contain any metal at the inlet, it was assumed to not approach bulk saturation, and since it could also not be analysed after the experiments, the logarithmic mean concentration difference between the aqueous and organic phases was estimated as:

$$C_{LM} = \frac{C_{in} - C_{out}}{\ln\left(\frac{C_{in}}{C_{out}}\right)} = \frac{0.36 - 0.34}{\ln\left(\frac{0.36}{0.34}\right)} = 0.35 \text{ g.L}^{-1} \quad \text{B 6}$$

The mass flux was determined by rearranging Eq. 2-7:

$$j_{Zr} = \frac{Q_{shell}}{A_{membrane}} (C_{in} - C_{out}) = \frac{(4.2 \times 10^{-6})}{1.8} (0.36 - 0.34) = 5.0 \times 10^{-8} \text{ kg.m}^{-2}\text{s}^{-1} \quad \text{B 7}$$

From the mass flux, the overall mass transfer coefficients were determined by substituting the mass flux into Eq. 2-14:

$$K_{OV} = \frac{Q_S \Delta C_S}{A_{Mem} \Delta C_{LM}} = \frac{j_{Zr}}{\Delta C_{LM}} = \frac{5.0 \times 10^{-8}}{0.35} = 1.4 \times 10^{-7} \text{ m.s}^{-1} \quad \text{B 8}$$

The above calculations were performed on the data from each of the MBSX experiments and compiled into Table B-9 (Zr data), and Table B-10 (Hf data). It is evident that both the Zr and Hf data from the $U_{Lumen} = 1.6 \times 10^{-3} \text{ m.s}^{-1}$ was significantly different from the other data sets and it was assumed that an error had occurred during the experiment, therefore it was not considered further. The mass flux values as a function of the velocity for Zr and Hf are illustrated in Figure B-11 and Figure B-12, respectively.

Table B-9: The Zr shell-side concentration, mass flux, and overall MTC data for the shell and lumen velocity variation series of experiments. Boldface values indicate the experimental variable.

Parameter	Unit	Shell-side velocity variation			
U_{Shell}	m.s⁻¹	1.6 x10⁻⁴	8.2 x10⁻³	1.6 x10⁻³	4.1 x10⁻³
U _{Lumen}	m.s ⁻¹	6.7 x10 ⁻³	6.7 x10 ⁻³	6.7 x10 ⁻³	6.7 x10 ⁻³
C _{in} ^{Zr}	g.L ⁻¹	16.0	16.0	16.0	16.0
C _{out} ^{Zr}	g.L ⁻¹	7.8	13.4	14.6	15.1
C _{LM} ^{Zr}	g.L ⁻¹	11.4	14.6	15.3	15.5
j _{Zr} x10 ⁻⁸	kg.m ⁻² s ⁻¹	76.2	123	133	214
K _{OV} x10 ⁻⁸	m.s ⁻¹	6.69	8.40	8.68	13.8
Lumen-side velocity variation					
U _{Shell}	m.s ⁻¹	1.6 x10 ⁻³	1.6 x10 ⁻³	1.6 x10 ⁻³	1.6 x10 ⁻³
U_{Lumen}	m.s⁻¹	6.7 x10⁻⁴	1.6 x10⁻³	6.7 x10⁻³	1.7 x10⁻²
C _{in} ^{Zr}	g.L ⁻¹	16.0	16.0	16.0	16.0
C _{out} ^{Zr}	g.L ⁻¹	15.3	13.2	14.4	14.1
C _{LM} ^{Zr}	g.L ⁻¹	15.6	14.5	15.2	15.0
j _{Zr} x10 ⁻⁸	kg.m ⁻² s ⁻¹	69.5	261	146	178
K _{OV} x10 ⁻⁸	m.s ⁻¹	4.45	18.0	9.60	11.8

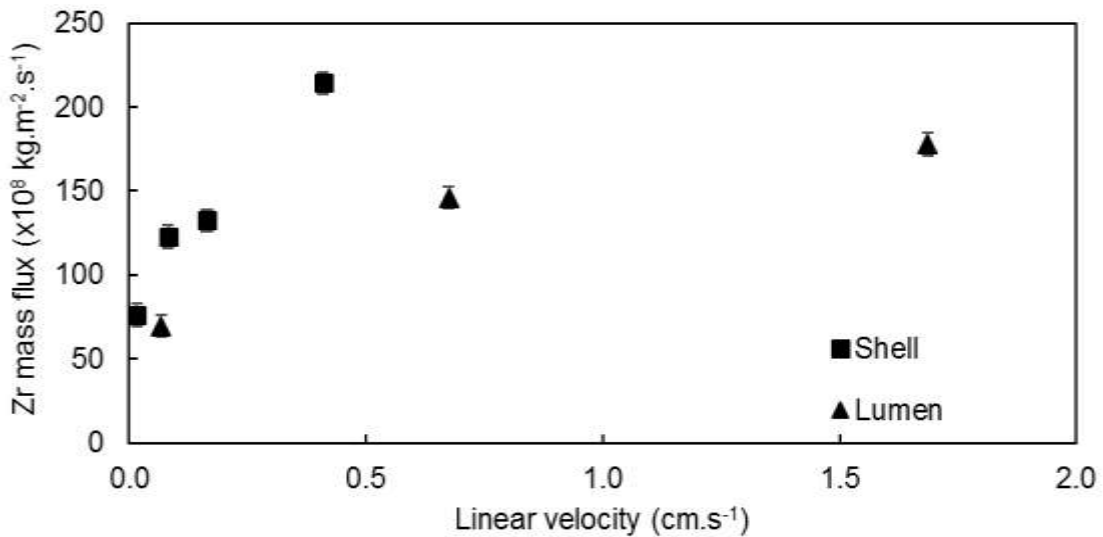


Figure B-11: The effect of the shell and lumen flow velocity on the mass flux of Zr.

Table B-10: The Hf shell-side concentration, mass flux, and overall MTC data for the shell and lumen velocity variation series of experiments. Boldface values indicate the experimental variable.

Parameter	Unit	Shell-side velocity variation			
		U_{Shell}	m.s⁻¹	1.6 x10⁻⁴	8.2 x10⁻³
U _{Lumen}	m.s ⁻¹	6.7 x10 ⁻³	6.7 x10 ⁻³	6.7 x10 ⁻³	6.7 x10 ⁻³
C _{in} ^{Hf}	g.L ⁻¹	0.36	0.36	0.36	0.36
C _{out} ^{Hf}	g.L ⁻¹	0.16	0.27	0.30	0.34
C _{LM} ^{Hf}	g.L ⁻¹	0.24	0.31	0.33	0.35
j _{Hf} x10 ⁻⁸	kg.m ⁻² s ⁻¹	1.86	3.99	4.88	4.97
K _{OV} x10 ⁻⁸	m.s ⁻¹	7.65	12.8	14.8	14.4
Lumen-side velocity variation					
U _{Shell}	m.s ⁻¹	1.6 x10 ⁻³	1.6 x10 ⁻³	1.6 x10 ⁻³	1.6 x10 ⁻³
U_{Lumen}	m.s⁻¹	6.7 x10⁻⁴	1.6 x10⁻³	6.7 x10⁻³	1.7 x10⁻²
C _{in} ^{Hf}	g.L ⁻¹	0.36	0.36	0.36	0.361
C _{out} ^{Hf}	g.L ⁻¹	0.34	0.29	0.30	0.300
C _{LM} ^{Hf}	g.L ⁻¹	0.35	0.32	0.33	0.33
j _{Hf} x10 ⁻⁸	kg.m ⁻² s ⁻¹	1.98	6.42	5.58	5.56
K _{OV} x10 ⁻⁸	m.s ⁻¹	5.73	20.0	17.1	17.1

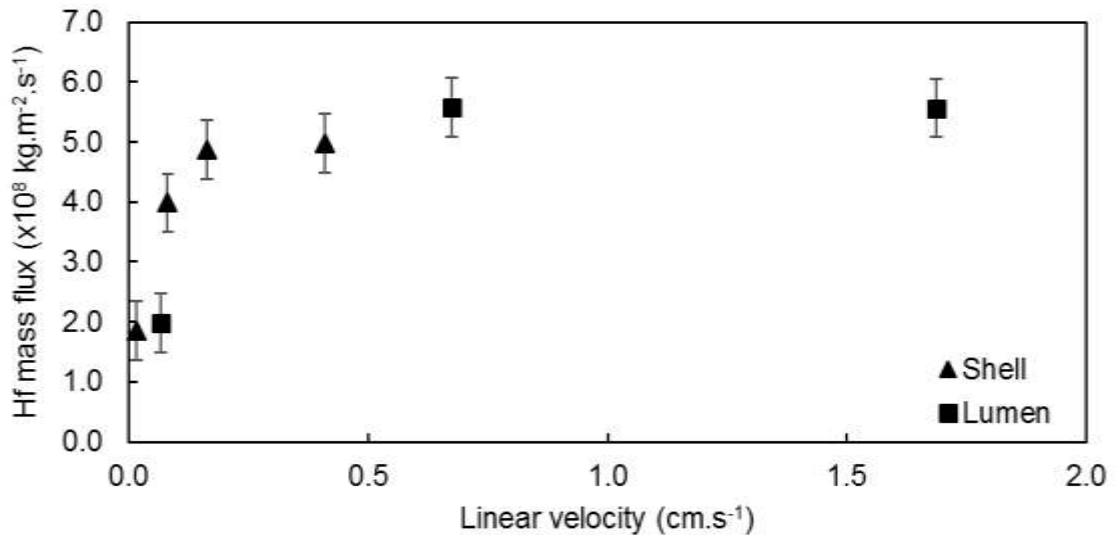


Figure B-12: The effect of the shell and lumen flow velocity on the mass flux of Zr.

Individual mass transfer coefficients

The individual mass transfer coefficients, consisting of the membrane, lumen, and shell components were estimated using the parameters listed in Table B-11. The example below uses the parameters for Hf related to the 0.41 cm.s⁻¹ shell-side velocity experiment.

$$k_{Mem} = \frac{D_{AB}\varepsilon}{\tau\delta} = \frac{(1.73 \times 10^{-10})(0.4)}{(2.4)(40 \times 10^{-6})} = 7.22 \times 10^{-7} m.s^{-1} \quad B\ 9$$

$$\frac{k_{Lumen}d_H}{D_{AB}} = 1.5 \left(\frac{d_L^2 U_L}{LD_{AB}} \right)^{0.33} \quad B\ 10$$

$$\frac{k_{Lumen}(220 \times 10^{-6})}{1.73 \times 10^{-10}} = 1.5 \left(\frac{(220 \times 10^{-6})^2 (6.7 \times 10^{-3})}{(0.4)(1.73 \times 10^{-10})} \right)^{0.33}$$

$$k_{Lumen} = 1.97 \times 10^{-6} m.s^{-1}$$

$$\frac{1}{k_{Shell}} = \frac{1}{K_{OV}} - \frac{d_{OD}}{Pk_{Mem}d_{LM}} - \frac{d_{OD}}{Pk_{Lumen}d_{LD}} \quad B\ 11$$

$$\frac{1}{k_{Shell}} = \frac{1}{1.44 \times 10^{-7}} - \frac{300 \times 10^{-6}}{(158)(7.22 \times 10^{-7})(5.9 \times 10^{-4})} - \frac{300 \times 10^{-6}}{(158)(2.0 \times 10^{-6})(220 \times 10^{-6})}$$

$$k_{Shell} = 1.44 \times 10^{-7} m.s^{-1}$$

The above calculations were repeated for Zr and Hf, and for both the shell-side velocity variation and lumen-side velocity variation data sets to obtain the data listed in Table B-12 and Table B-13. Table B-12 lists the data for Zr, while Table B-13 lists the data for Hf. In both tables the boldfaced values indicate the variables of the experiment. Note that the $U_{Lumen} = 1.6 \times 10^{-3} m.s^{-1}$ experimental data has been included only for the sake of completeness.

The contributions of each resistance to the total resistance is illustrated in Figure B-13. It is evident that the resistance from the shell contributed the vast majority of the resistance and therefore determined the overall rate of mass transfer.

Table B-11: Parameters for estimating the individual mass transfer coefficients.

Parameter	Unit	Value
Membrane		
Porosity	-	0.4
Tortuosity	-	2.4
Thickness	μm	40
Total surface area ¹	m ²	1.8
ID	um	220
OD	um	300
Total length ¹	m	0.4
Module		
ID	m	3.6 x10 ⁻²
Hydraulic diameter	m	3.6 x10 ⁻⁴
Zr species		
Aq. molecular vol.	m ³ .mol ⁻¹	0.017
Aq. diffusion coefficient ²	m ² .s ⁻¹	1.40 x10 ⁻⁹
Org. molecular volume	m ³ .mol ⁻¹	2.1
Org. diffusion coefficient ²	m ² .s ⁻¹	1.78 x10 ⁻¹⁰
Partition coefficient	-	20.7
Hf species		
Aq. molecular volume	m ³ .mol ⁻¹	0.015
Aq. diffusion coefficient ¹	m ² .s ⁻¹	1.49 x10 ⁻⁹
Org. molecular vol.	m ³ .mol ⁻¹	2.2
Org. diffusion coefficient ¹	m ² .s ⁻¹	1.73 x10 ⁻¹⁰
Partition coefficient	-	158
Aqueous phase		
Density	kg.m ⁻³	1050
Viscosity ³	Pa.s	2.1 x10 ⁻³
Organic phase		
Density	kg.m ⁻³	851
Viscosity ³	Pa.s	2.1 x10 ⁻³

¹ Two series-connected modules.
² Determined by Wilke-Chang equation, Eq. 2-17 [18].
³ Relation by Koekemoer *et al.* (2005) [69].

Table B-12: The Zr mass transfer data table for the MBSX series of experiments.

Parameter	Unit	Shell-side velocity variation			
U_{Shell}	m.s⁻¹	6.7 x10⁻⁴	3.4 x10⁻³	6.7 x10⁻³	1.7 x10⁻²
U _{Lumen}	m.s ⁻¹	6.7 x10 ⁻³	6.7 x10 ⁻³	6.7 x10 ⁻³	6.7 x10 ⁻³
K _{OV} x10 ⁻⁸	m.s ⁻¹	6.7	8.4	8.7	14
k _{Mem} x10 ⁻⁸	m.s ⁻¹	74	74	74	74
k _{Lumen} x10 ⁻⁸	m.s ⁻¹	200	200	200	200
k _{Shell} x10 ⁻⁸	m.s ⁻¹	6.7	8.4	8.7	14
Lumen-side velocity variation					
U _{Shell}	m.s ⁻¹	1.6 x10 ⁻³	1.6 x10 ⁻³	1.6 x10 ⁻³	1.6 x10 ⁻³
U_{Lumen}	m.s⁻¹	6.7 x10⁻⁴	1.6 x10⁻³	6.7 x10⁻³	1.7 x10⁻²
K _{OV} x10 ⁻⁸	m.s ⁻¹	4.8	18	9.6	12
k _{Mem} x10 ⁻⁸	m.s ⁻¹	74	74	74	74
k _{Lumen} x10 ⁻⁸	m.s ⁻¹	94	159	200	271
k _{Shell} x10 ⁻⁸	m.s ⁻¹	4.5	18	9.6	12

Table B-13: The Hf mass transfer data table for the MBSX series of experiments.

Parameter	Unit	Shell-side velocity variation			
U_{Shell}	m.s⁻¹	6.7 x10⁻⁴	3.4 x10⁻³	6.7 x10⁻³	1.7 x10⁻²
U _{Lumen}	m.s ⁻¹	6.7 x10 ⁻³	6.7 x10 ⁻³	6.7 x10 ⁻³	6.7 x10 ⁻³
K _{OV} x10 ⁻⁸	m.s ⁻¹	7.7	13	15	14
k _{Mem} x10 ⁻⁸	m.s ⁻¹	72	72	72	72
k _{Lumen} x10 ⁻⁸	m.s ⁻¹	197	197	197	197
k _{Shell} x10 ⁻⁸	m.s ⁻¹	7.7	13	15	14
Lumen-side velocity variation					
U _{Shell}	m.s ⁻¹	1.6 x10 ⁻³	1.6 x10 ⁻³	1.6 x10 ⁻³	1.6 x10 ⁻³
U_{Lumen}	m.s⁻¹	6.7 x10⁻⁴	1.6 x10⁻³	6.7 x10⁻³	1.7 x10⁻²
K _{OV} x10 ⁻⁸	m.s ⁻¹	5.7	20	17	17
k _{Mem} x10 ⁻⁸	m.s ⁻¹	72	72	72	72
k _{Lumen} x10 ⁻⁸	m.s ⁻¹	92	157	197	267
k _{Shell} x10 ⁻⁸	m.s ⁻¹	5.7	20	17	17

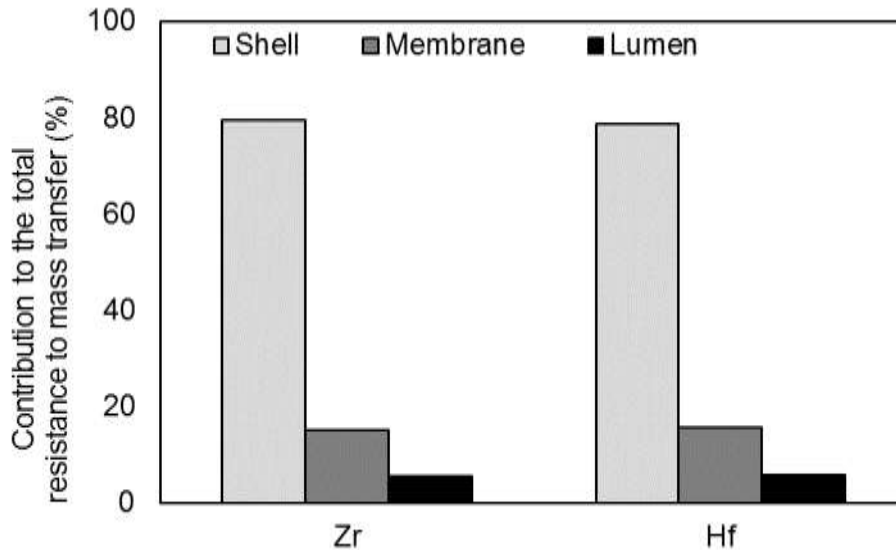


Figure B-13: The contribution of the individual resistances to the total resistance to mass transfer for $U_{Shell} = 1.7 \times 10^{-2} \text{ m.s}^{-1}$.

Model fitting

From Figure B-13, it is evident that the shell-side mass transfer coefficient was the determining component of the overall rate of mass transfer. Therefore, going forward, the membrane and lumen coefficients were discarded from the model development process, with the focus on modelling the shell-side mass transfer coefficient. Several Sherwood relations from literature (see Table 2-4) were used to estimate the shell-side mass transfer coefficients by substituting the parameters that have been listed in Table B-11. As all the models provided poor predictions of the experimental data (see Figure 4-15 and Figure 4-16), the experimental mass flux was modelled using a Sherwood-type relation given in Eq.4-5:

$$j_{experimental} = \frac{\dot{Q}_{Shell}}{A_{mem}} (C_{in} - C_{out})_{Shell} \quad 4-4$$

$$j_{calculated} = \alpha Re^{\beta} Sc^{0.33} \left(\frac{D_{AB}}{d_H} \right) \Delta C_{LM} \quad 4-5$$

Since the modelling process is described in detail in Section 4.4, only a limited discussion is presented here. The fitting parameters, α , and β , of Eq. 4-5 were solved using the MS Excel Solver add-in to minimize the error value of an objective function, Eq. 4-6:

$$Error = \sum (j_{experimental} - j_{calculated})^2 \quad 4-6$$

The experimental and estimated mass flux values, the error values of the objective function, and the values obtained for α , and β are listed in Table B-14 for Zr Table B-15 for Hf.

Table B-14: Objective function error for Zr model.

Parameter	Shell-side velocity (m.s ⁻¹)			
	6.7 x10 ⁻⁴	3.4 x10 ⁻³	6.7 x10 ⁻³	1.7 x10 ⁻²
$j_{\text{experimental}}$ (x10 ⁻⁸ kg.m ⁻² .s ⁻¹)	76.2	123	133	214
$j_{\text{calculated}}$ (x10 ⁻⁸ kg.m ⁻² .s ⁻¹)	61	122	155	203
Error	2.3 x10 ⁻¹⁴	3.9 x10 ⁻¹⁷	4.9 x10 ⁻¹⁴	1.4 x10 ⁻¹⁴
Sum of errors	8.6 x10 ⁻¹⁴			
Fitted parameters				
α	0.00337			
β	0.276			

Therefore, the mass flux for Zr could be estimated using:

$$j_{\text{calculated}} = 0.0034Re^{0.28}Sc^{0.33} \left(\frac{D_{AB}}{d_H} \right) \Delta C_{LM} \quad 4-7$$

Table B-15: Objective function error for Hf model.

Parameter	Shell-side velocity (m.s ⁻¹)			
	6.7 x10 ⁻⁴	3.4 x10 ⁻³	6.7 x10 ⁻³	1.7 x10 ⁻²
$j_{\text{experimental}}$ (x10 ⁻⁸ kg.m ⁻² .s ⁻¹)	1.88	4.03	4.93	5.03
$j_{\text{calculated}}$ (x10 ⁻⁸ kg.m ⁻² .s ⁻¹)	2.19	3.65	4.32	5.26
Error	9.4 x10 ⁻¹⁸	1.5 x10 ⁻¹⁷	3.7 x10 ⁻¹⁷	5.4 x10 ⁻¹⁷
Sum of errors	6.7 x10 ⁻¹⁷			
Fitted parameters				
α	0.00361			
β	0.163			

The mass flux for Hf could be estimated using:

$$j_{\text{calculated}} = 0.0036Re^{0.16}Sc^{0.33} \left(\frac{D_{AB}}{d_H} \right) \Delta C_{LM} \quad 4-8$$

Finally, two parity plots of the calculated vs experimental mass flux values for Zr (Figure B-14) and Hf (Figure B-15) are provided showing that the experimental mass flux was adequately estimated using the fitted parameters.

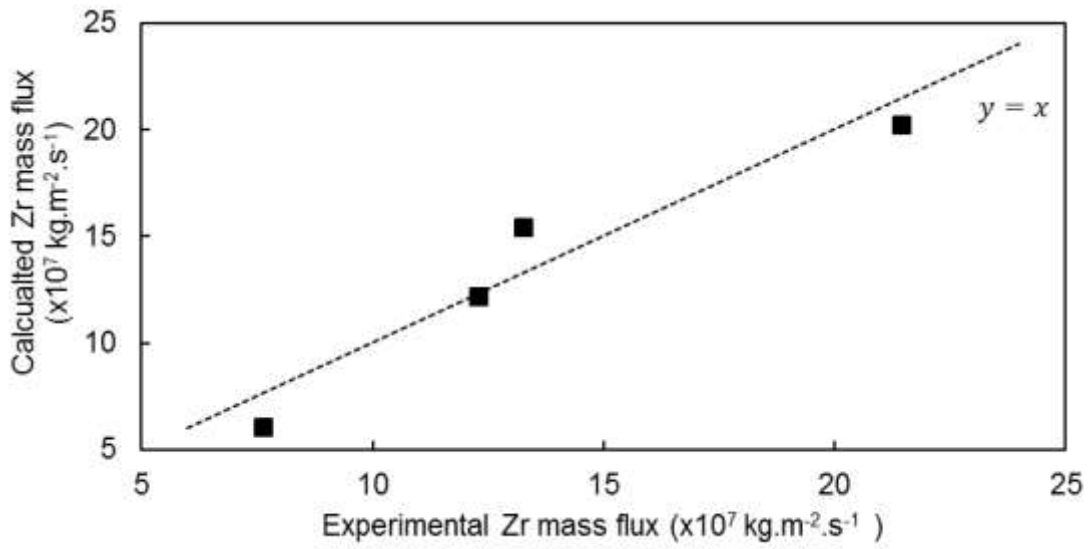


Figure B-14: The experimental vs. calculated Zr mass flux values for fitting of the Sherwood relation.

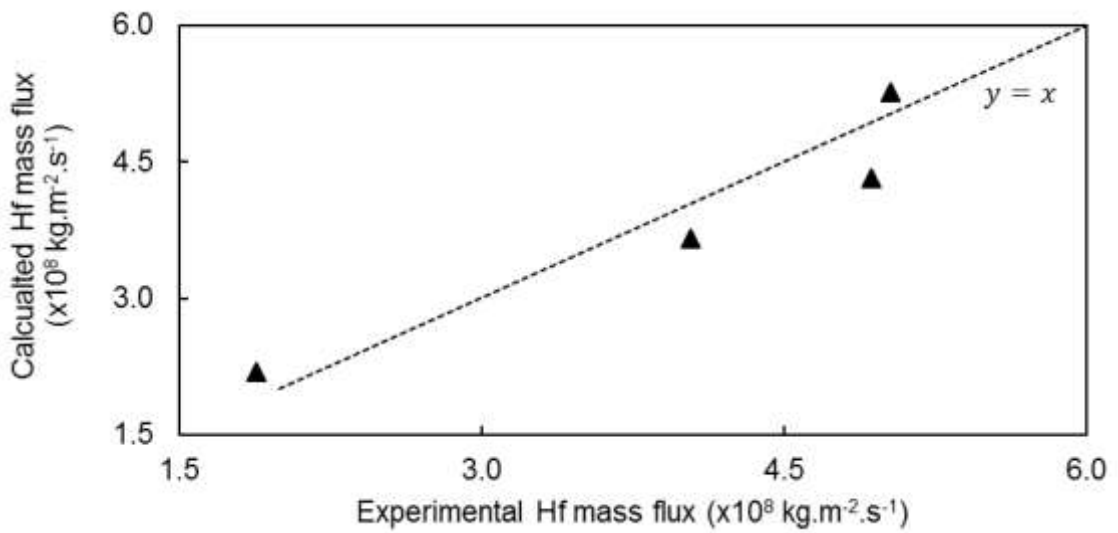


Figure B-15: The experimental vs. calculated Hf mass flux values for fitting of the Sherwood relation.